

TUNNELING IONIZATION OF NOBLE GAS ATOMS USING A HIGH  
INTENSITY LASER AT 1  $\mu\text{m}$  WAVELENGTH

by

Steven Jay Augst

Submitted in Partial Fulfillment  
of the  
Requirements for the Degree

DOCTOR OF PHILOSOPHY

Supervised by David D. Meyerhofer  
and J. H. Eberly

Department of Physics and Astronomy  
and College of Arts and Science

University of Rochester  
Rochester, New York

1991

## CURRICULUM VITAE

Steven Jay Augst was born on January 23, 1963 in Menahga, Minnesota. He attended Gustavus Adolphus College from 1981 to 1985 where he graduated *Magna Cum Laude* with a B.A. degree in Physics. From 1985 to 1991 he attended the University of Rochester as a graduate student in the department of Physics and Astronomy where he was the recipient of a three year Rush Rhees fellowship. His research work was performed at the Laboratory for Laser Energetics under the supervision of David D. Meyerhofer.

### Publication list:

- Y. H. Chuang, D. D. Meyerhofer, S. Augst, H. Chen, J. Peatross, and S. Uchida, "Suppression of the Pedestal in a Chirped-Pulse-Amplification Laser," *J. Opt. Soc. Am. B.* **8**, 1226 (1991).
- S. Augst, D. D. Meyerhofer, J. Peatross, and C. I. Moore, "Spatial distribution of high-order harmonics generated in the tunneling regime", in the Proceedings of *Short-Wavelength Coherent Radiation: Generation and Application (OSA topical meeting)*, Monterey, CA April 1991 (pub. by OSA, Washington D. C., 1991).
- S. Augst, D. D. Meyerhofer, D. Strickland, and S. L. Chin, "Laser Ionization of Noble Gases by Coulomb-Barrier Suppression," *J. Opt. Soc. Am. B.* **8**, 858 (1991).
- S. Augst, D. D. Meyerhofer, C. I. Moore, and J. Peatross, "Tunneling Ionization and Harmonic Generation in Krypton Gas using a High-Intensity, 1- $\mu\text{m}$ , 1-ps Laser", in the Proceedings of SPIE OE/LASE '90, *Femtosecond to Nanosecond High-Intensity Lasers and Applications*, 1229, 152 (pub. by SPIE, Bellingham, WA, 1990).
- S. Augst, D. Strickland, D. D. Meyerhofer, S. L. Chin and J. H. Eberly, "Tunneling Ionization of Noble Gases in a High-Intensity Laser Field," *Phys. Rev. Lett.* **63**, 2212 (1989).

## ACKNOWLEDGMENTS

I would like to thank Dr. David Meyerhofer for providing daily supervision and insightful discussions regarding experiments and the analysis of the data which was obtained. I would also like to thank Dr. Joseph Eberly for being my official advisor and for providing many critical readings of publications and this thesis. I would also like to thank Dr. See-Leang Chin who initiated the ionization experiments at the Laboratory for Laser Energetics when he was a visiting professor at the University of Rochester. He provided many fruitful discussions and much encouragement.

Dr. Robert Kremens provided extensive help and guidance throughout the course of my graduate career. His philosophy regarding scientific research was both helpful and at times entertaining. Without his expertise many of these experiments would not have been completed.

The assistance of several other graduate students was also greatly appreciated. Among these are: Yung-Ho Chuang who taught me much about lasers and who refined the original laser system design so that it did not require constant supervision, Justin Peatross who traded shifts with me when we did 16 hour data runs and let me borrow his computer to write this thesis, Chris Moore who did virtually all the analysis of the harmonic generation experiments (which are not discussed in this thesis), and Shigeaki Uchida and Hong Chen for numerous helpful suggestions and discussions.

The original laser system was designed and built by Dr. Donna Strickland, Patrick Maine, and Dr. Gerard Mourou. I would like to thank them for the use of this laser.

Lastly, I greatly appreciate the support of the staff at the Laboratory for Laser Energetics. This work was supported by the National Science Foundation under contract No. PHY 8822730. Additional support was provided by the U.S. Department of Energy Division of Inertial Fusion under agreement No. DE-FC03-85DP40200 and by the Laser Fusion Feasibility Project at the Laboratory for Laser Energetics which has the following sponsors: Empire State Electric Energy Research Corporation, New York State Energy Research and Development Authority, Ontario Hydro, and the University of Rochester.

## ABSTRACT

Laser induced ionization of noble gases has been studied with a 1-ps, 1- $\mu\text{m}$  laser. An experimental survey of the intensity dependence for ion production is presented for a large number of charge states. The survey spans intensities from  $10^{14}$  W/cm<sup>2</sup> to mid- $10^{16}$  W/cm<sup>2</sup>, which exceeds the intensities of previous surveys at this wavelength by over an order of magnitude.

The ion production is compared to several theoretical models. Tunneling (or field-ionization) models rather than multiphoton models describe the data best, and the two models that have the most satisfactory agreement are: 1) a one-dimensional Coulomb barrier suppression model, and 2) a species dependent quasiclassical tunneling model. The  $I^N$  ionization rate dependence which is predicted by lowest-order perturbation theory is not observed for 1 ps laser pulses. Various forms of Keldysh's model cannot accurately describe the ionization of all the charge states. Two Thomas-Fermi models show varying degrees of agreement with the data.

Experiments comparing linearly and circularly polarized light suggest that the ionization process is non-resonant with this wavelength and in this intensity regime. This is in contrast to some previous experiments at shorter wavelengths which suggests that all ionization is resonant. Two resonance criteria are suggested, both of which place the shorter wavelength experiments in the resonance regime and our longer, 1- $\mu\text{m}$  wavelength experiments in the non-resonant regime. The two suggested criteria for resonance both have a strong frequency dependence which explains the transition to non-resonant ionization with our 1- $\mu\text{m}$  wavelength.

## TABLE OF CONTENTS

CURRICULUM VITAE .....	ii
ACKNOWLEDGMENTS.....	iii
ABSTRACT .....	v
TABLE OF CONTENTS.....	vi
LIST OF TABLES .....	viii
LIST OF FIGURES .....	ix
INTRODUCTION .....	1
A. Perturbation Theory .....	3
B. Tunneling and Suppression Models.....	5
C. Keldysh Approximation .....	7
D. Ponderomotive Potential.....	8
E. Ion Yield Experiments .....	11
F. Resonantly Enhanced Ionization: Ion Spectra .....	16
G. Resonantly Enhanced Ionization: Electron Spectroscopy .....	18
H. Additional Ionization Experiments.....	20
I. Organization of Document.....	23
EXPERIMENTAL APPARATUS .....	25
A. The Laser .....	25
B. Intensity Measurements.....	32
C. Intensity Measurements from Electron Energies.....	36
D. Uncertainties in Intensity .....	38
E. Ion Spectrometer: Data Acquisition.....	41
F. Ion Spectrometer: Data Analysis .....	45

ION EXPERIMENTS .....	49
A. The Data .....	49
B. Comparison to Other Experiments.....	59
COMPARISON BETWEEN EXPERIMENTS AND THEORIES .....	65
A. Procedure for Comparison .....	65
B. Barrier Suppression Ionization (BSI) Theory.....	70
C. ADK Theory .....	80
D. Keldysh Theory.....	90
E. Keldysh-Faisal-Reiss (KFR) Theory .....	94
F. Constant Potential Modification to KFR Theory.....	99
G. Thomas-Fermi models .....	101
ADDITIONAL IONIZATION EXPERIMENTS.....	103
A. Linear versus Circular Polarization and Resonant Ionization.....	103
B. Pulse Duration and Bandwidth Experiments .....	109
C. Second Harmonic Generation Experiments .....	118
CLOSING REMARKS.....	121
A. Summary .....	121
B. Future experiments .....	123
APPENDICES.....	124
A. Pulse Fluctuation Measurement.....	124
B. Time of Flight Calculation.....	126
C. Integration of Coupled Rate Equations.....	129
D. Iso-Intensity Volume Calculation.....	135
E. Second Harmonic Experimental Procedure.....	138
REFERENCES.....	140

## LIST OF TABLES

4.1	BSI Threshold intensities for the next higher charge state than was observed. The intensities exceed those which were used in the experiment so it is reasonable that we did not see these charge states.....	73
5.1	Laser intensity at which $\mathcal{E}^2 = 4\omega_L^3$ for various wavelengths. Resonant enhancement is not expected for $\mathcal{E}^2 \gg 4\omega_L^3$ .....	107

## LIST OF FIGURES

1.1	(a) A bound state in a Coulomb potential and (b) Superposition of a Coulomb and a static electric field potential with the same bound state. The electron can now tunnel out quite easily.....	6
1.2	Electron energy spectra. The numbers at the left show the time advance between the electron pulse and the laser pulse. The electron pulse is generated 180 $\mu\text{m}$ from the laser focus. [from Fig. 2 of reference 27].....	10
1.3	Contour plot of the laser intensity distribution near focus. The 80%, 50%, 20%, and 10% intensity contours are shown. The graph assumes focusing by an $f/1$ lens. The dimensions scale with $f\#$ as $r \propto f\#$ and $z \propto f\#^2$ . .....	12
1.4	The number of xenon ions produced as a function of laser intensity for $\tau = 50$ ps and $\lambda = 1064$ nm. The $I^N$ dependence, saturation of the focal volume, and direct ionization are features of the data which are described in the text. [from Fig. 2 of reference 14].....	14
1.5	Production of xenon ions using a 50 ps laser pulse at 532 nm. Direct and sequential ionization processes are clearly present in the second charge state. [from Fig. 3 of reference 15].....	15
1.6	Electron energy spectrum from reference [46]. The peaks correspond to various levels coming into resonance as the ponderomotive potential changes with laser intensity. The energy of the electron peaks is approximately given by $(N \hbar \omega - E - U_P)$ . .....	19

1.7	Initially non-resonant six-photon ionization becomes enhanced when an upper level is Stark shifted into a five-photon resonance. The energy of the freed electron decreases by an amount which is approximately equal to the value of the ponderomotive potential which is present at the time resonant enhancement occurs.....	20
2.1	The parts of the CPA laser system. ....	28
2.2	Diagram showing how a chirped pulse can be compressed with a grating pair. The blue ray travels a shorter distance so it can catch up to the red ray. A single pass results in an oval beam and a double pass results in a circular beam. If a telescope with magnification of one is placed between the gratings, the separation of the gratings can be effectively negative. This results in a temporal expansion of the pulse.....	29
2.3	Autocorrelator. The wedged beam splitter and slits are used to prevent all étalon reflections from reaching the photomultiplier. The PIN diode detects shot-to-shot laser energy fluctuations. This setup becomes a single-shot autocorrelator when the slits are removed and the photomultiplier is replaced by a linear-array detector. ....	33
2.4	Autocorrelation trace of the compressed laser pulse for the experiments described in chapter five.....	34
2.5	Time-of-flight spectrometer used for measuring electron energies and ion mass-to-charge ratios.....	38
2.6	Vacuum tank, TOF spectrometer, and gas delivery system. ....	43
2.7	Time-of-flight spectrum of xenon. The detector is saturated when the first charge state arrives (at about 7 $\mu$ s).....	44

2.8	Quantum efficiency of an MCP detector versus ion energy. Our ion energies range from 3 keV for singly charged particles to 27 keV for nine times ionized particles. [from reference 74] .....	46
2.9	Log-log plot of the production of Xe <sup>+</sup> ions versus laser intensity using three different gas densities. Saturation of the detector is clearly seen for each of the three different backfill pressures. ....	47
3.1	Helium ion production rate as a function of peak laser intensity. The relative intensity error can be deduced from the scatter of the data points and the error bar represents the absolute intensity error. (P = 5 × 10 <sup>-6</sup> Torr) .....	50
3.2	Neon ion production rate as a function of peak laser intensity. The relative intensity error can be deduced from the scatter of the data points and the error bar represents the absolute intensity error. (P = 2.5 × 10 <sup>-6</sup> Torr).....	51
3.3	Argon ion production rate as a function of peak laser intensity. The relative intensity error can be deduced from the scatter of the data points and the error bar represents the absolute intensity error. (P = 5 × 10 <sup>-6</sup> Torr) .....	52
3.4	Krypton ion production rate as a function of peak laser intensity. The relative intensity error can be deduced from the scatter of the data points and the error bar represents the absolute intensity error. (P = 5 × 10 <sup>-6</sup> Torr) .....	53
3.5	Xenon ion production rate as a function of peak laser intensity. The relative intensity error can be deduced from the scatter of the data points and the error bar represents the absolute intensity error. (P = 5 × 10 <sup>-6</sup> Torr) .....	54
3.6	Helium TOF spectrum at (a) low intensity and (b) high intensity. He <sup>2+</sup> is present in (b) but not in (a). ....	56

3.7	Ion threshold intensity vs. sequential ionization potential for five noble gases. There is a clear species dependence present. The relative error in the laser intensity is approximately the size of the data symbols. ....	58
3.8	Keldysh's $\gamma$ parameter at the threshold intensity for each of the charge states. In each case $\gamma < 1$ which indicates that ionization occurs in the tunneling regime. ....	59
3.9	Helium ion threshold intensities versus sequential ionization potential for various experimental groups. ....	60
3.10	Neon ion threshold intensities versus sequential ionization potential for various experimental groups. ....	61
3.11	Argon ion threshold intensities versus sequential ionization potential for various experimental groups. ....	61
3.12	Krypton ion threshold intensities versus sequential ionization potential for various experimental groups. ....	62
3.13	Xenon ion threshold intensities versus sequential ionization potential for various experimental groups. ....	62
4.1	The change in ionization rate per laser cycle never exceeds $10^{-2}$ of the ionization rate. An $I^6$ rate is assumed since this is suggested by our data. A Gaussian intensity profile and an $I^6$ profile are also shown. ....	66
4.2	Comparison of experimentally determined and theoretically predicted threshold intensities using the BSI model. The solid line corresponds to exact agreement. Some of the higher charge states shown on this graph are not included on the ion curves since the production of these charge states occurred on only a few laser shots. ....	72

4.3	Comparison of helium ion data with theoretical curves calculated using the BSI model. The absolute intensity uncertainty is indicated. ....	74
4.4	Comparison of neon ion data with theoretical curves calculated using the BSI model. The absolute intensity uncertainty is indicated. ....	75
4.5	Comparison of argon ion data with theoretical curves calculated using the BSI model. The absolute intensity uncertainty is indicated. ....	76
4.6	Comparison of krypton ion data with theoretical curves calculated using the BSI model. The absolute intensity uncertainty is indicated. ....	77
4.7	Comparison of xenon ion data with theoretical curves calculated using the BSI model. The absolute intensity uncertainty is indicated. ....	78
4.8	The effective principal quantum number $n^*$ versus the sequential ionization potential for each of the charge states observed. ADK theory is expected to be valid for $n^* \gg 1$ . ....	82
4.9	Comparison of helium ion production and that predicted by ADK theory. The absolute intensity uncertainty is indicated. ....	84
4.10	Comparison of neon ion production and that predicted by ADK theory. The absolute intensity uncertainty is indicated. ....	85
4.11	Comparison of argon ion production and that predicted by ADK theory. The absolute intensity uncertainty is indicated. ....	86
4.12	Comparison of krypton ion production and that predicted by ADK theory. The absolute intensity uncertainty is indicated. ....	87

4.13	Comparison of xenon ion production and that predicted by ADK theory. The absolute intensity uncertainty is indicated.....	88
4.14	Predicted charge density as a function of radial distance using the ADK and BSI models at a laser intensity of $3 \times 10^{16}$ W/cm <sup>2</sup> . The corresponding laser profile is also shown.....	89
4.15	Comparison of the two forms of Keldysh's theory for ionization of xenon at 1 $\mu$ m wavelength and 1 ps pulse length. The corrected form accounts for the Coulomb potential in the wavefunction of the ionized electron.....	92
4.16	Comparison of xenon ion production and that predicted by the Coulomb-corrected Keldysh theory. The absolute intensity uncertainty is indicated.....	93
4.17	Comparison of helium ion production and that predicted by KFR theory. The absolute intensity uncertainty is indicated. ....	97
4.18	Comparison of xenon ion production and that predicted by KFR theory. The absolute intensity uncertainty is indicated. ....	98
4.19	Comparison of xenon ion production and that predicted by the Constant Potential Modification to Keldysh-Faisal-Reiss (KFR) theory. The absolute intensity uncertainty is indicated. ....	100
4.20	Comparison of experimentally determined and theoretically predicted threshold intensities using two Thomas-Fermi models. The solid line corresponds to exact agreement. (a) is from reference [85] and (b) is from Fig. 4 of reference [86] (Xe <sup>+</sup> is missing in their Fig. 4 so it could not be plotted here either).....	102
5.1	Angular momentum channels available for dipole transitions of linearly or circularly polarized light [from Fig. 13 in reference 9]. For large photon number there will be many more resonant channels available for linearly polarized light. ....	104

5.2	Comparison of the production of Xe <sup>+</sup> and Ne <sup>+</sup> ions for linearly and circularly polarized light. The laser pulse length is 1.9 ps.....	105
5.3	Xenon ion production for 55 ps laser pulse with 0.3 Å bandwidth.....	110
5.4	Xenon ion production for 55 ps laser pulse with 7 Å bandwidth.....	111
5.5	Xenon ion production for a 55 ps pulse with 0.3 Å bandwidth. There is some evidence for a transition from the multiphoton regime to the tunneling regime.....	113
5.6	Comparison between the 55 ps data obtained at LLE and the 50 ps data obtained by L'Huillier. L'Huillier's data is aligned with the lower saturation level.....	115
5.7	Comparison between the 55 ps data obtained at LLE and the 50 ps data obtained by L'Huillier. L'Huillier's data is aligned with the upper saturation level.....	116
5.8	Comparison of Xe <sup>+</sup> ion production for 1.9 ps and 55 ps laser pulses at 1.053 μm wavelength.....	117
5.9	Four-wave mixing between the laser and another electric field with frequency $\omega_p$ . If the field is static then $\omega_p = 0$ and second harmonic generation results.....	119
5.10	Second harmonic wavelength shift versus gas pressure (electron density is proportional to pressure in this range). The best fit line is $\Delta\lambda = -0.55 + 0.65 \times P^{0.58}$ .....	119
B.1	Drawing of the ion time-of-flight spectrometer.....	126

## CHAPTER ONE

### INTRODUCTION

This thesis presents the first systematic experimental survey of noble gas photoionization using 1  $\mu\text{m}$  wavelength radiation at intensities of the order of the atomic unit of intensity ( $I_A = e^2 m^4 / \hbar^8 \sim 3 \times 10^{16} \text{ W/cm}^2$ ). Remarkably, recent advances can still be related to physical pictures developed almost a century ago, in the earliest stages of the development of quantum theory. Experimental evidence for the quantized nature of light was first produced by Hertz in 1887. He observed that when metal plates were irradiated with light they emitted electrons only when the light frequency was larger than some critical value. This effect could not be explained using classical electromagnetic theory. In 1905 Einstein used the concepts of Planck to explain this phenomenon as the photoelectric effect.<sup>1</sup> This work by Einstein led very gradually to a general acceptance of the idea that light is quantized, and is the work for which Einstein's Nobel Prize was awarded in 1921.

Another development in the study of light-matter interactions was a proposal by Maria Goeppert-Mayer in 1931. She predicted that very intense light sources would be able to induce two-photon ionization of atoms.<sup>2</sup> After the invention of the laser in 1960 it became possible to produce light beams of sufficient intensity to observe related processes. Experimental evidence of a two photon excitation by light from a ruby laser was obtained in 1961 by Kaiser and Garrett<sup>3</sup> and later by Abella.<sup>4</sup> Observation of multiphoton ionization (MPI) first occurred in 1963 when Meyerand and Haught<sup>5</sup> used a ruby laser to ionize argon and helium atoms. Other early MPI studies were done by Voronov and Delone<sup>6-8</sup> in xenon and krypton gases.

Lasers with field strengths large enough to ionize atoms have been widely available for over twenty years now and the interaction of very intense laser pulses with matter has constantly been a topic of great interest, as available laser intensities have increased from  $10^{11}$  W/cm<sup>2</sup> to  $10^{19}$  W/cm<sup>2</sup>. Interest in the study of both atomic physics (low particle density) and plasma physics (high particle density) has developed. The topic discussed here is the interaction of laser pulses with low density noble gas atoms. Several experimental methods can be used to explore this interaction. These include spectroscopic studies of ions, electrons, or photons. We have performed experiments to study both ion and photon spectra, but this thesis will deal mainly with the ion spectra.

Einstein's photoelectric theory predicts that an atom cannot be ionized when the energy of incident photons is less than the binding potential of the atom. How then does MPI work? The uncertainty principle supplies an answer. If photons strike an atom at a fast enough rate ( $\Delta t < \hbar/\Delta E$ ) the atom is prohibited from "knowing" whether it is absorbing one photon or simultaneously absorbing many photons. The absorption of a single photon places the atom in an excited state which can be either real or virtual.<sup>9</sup> Usually there is no real level available that conserves energy, so we must deal with virtual states. The linewidth of a virtual state is of the order of the detuning from real energy levels. Since the state's "linewidth" is inversely proportional to its "lifetime" this means that a virtual state has a lifetime of the order of  $10^{-16}$  seconds ( $\sim \hbar/10\text{eV}$ ). If another photon is absorbed by the excited atom during this time, the electron can be further excited to a higher state which again is usually virtual. A series of such absorptions can lead to ionization of the atom since the continuum of positive energy (ionized) states is dense with real levels.

The intensity required to ionize a hydrogen atom can be estimated using the uncertainty principle. If 13.6 eV of energy passes through a disk with radius  $a_0$  (the Bohr radius) in a time  $\Delta t$  ( $= \hbar/13.6 \text{ eV} = 3 \times 10^{-16} \text{ sec}$ ) then ionization should occur. The cross section of a hydrogen atom is approximately  $\pi a_0^2 = 8 \times 10^{-17} \text{ cm}^2$ , so the required intensity should be

$$\frac{13.6 \text{ eV} \times 1.6 \times 10^{-19} \text{ J/eV}}{8 \times 10^{-17} \text{ cm}^2 \times 3 \times 10^{-16} \text{ s}} = 9 \times 10^{13} \text{ W/cm}^2.$$

Experimental observations of the ionization of hydrogen with a 248-nm wavelength laser indicate that an intensity of about  $1.5 \times 10^{13} \text{ W/cm}^2$  is required for ionization.<sup>10</sup> This model based on the uncertainty principle provides an order-of-magnitude estimation for the intensity which is required for ionization but many refinements could be made to it. Several theoretical approaches which are more rigorous in their treatment of the ionization process are introduced below.

### I.A. Perturbation Theory

Lowest order perturbation theory (LOPT) can be used to describe multi-photon ionization of atoms. The conventional approach assumes that the laser field is a small perturbation on the atomic field. For this reason the use of LOPT is restricted to relatively low intensities in order to keep the expansion parameter from exceeding unity. For two-photon ionization second-order perturbation theory predicts an ionization rate which is proportional to the laser intensity squared. The result is<sup>9,11-13</sup>

$$W_{FI}^{(2)} = \frac{2\pi}{\hbar} \left| \sum_A \frac{V_{FA} V_{AI}}{(E_A - E_I - \hbar\omega)} \right|^2 \delta(E_F - E_I - 2\hbar\omega). \quad (1.1)$$

A generalization of this to  $N$ -photon ionization leads to a transition rate which is proportional to the laser intensity raised to the  $N$ -th power:

$$W_{FI}^{(N)} = \frac{2\pi}{\hbar} \left| \sum_{A_{N-1} \dots A_1} \frac{V_{FA_{N-1}} \dots V_{A_2 A_1} V_{A_1 I}}{(E_{A_{N-1}} - E_I - (N-1)\hbar\omega) \dots (E_{A_2} - E_I - 2\hbar\omega)(E_{A_1} - E_I - \hbar\omega)} \right|^2 \times \delta(E_F - E_I - N\hbar\omega) \quad (1.2)$$

Here the  $V$ 's represent the dipole radiation matrix element of  $e\mathbf{r} \cdot \mathcal{E}$ ,  $E_A$  is the energy of the intermediate state  $A$  and  $\mathcal{E}$  is the electric field strength of the laser. We see that  $V/(E_A - E_I - n\hbar\omega)$  is the effective perturbation expansion parameter. Using typical values of  $|r| \sim 0.5 \text{ \AA}$  and  $(E_A - E_I - n\hbar\omega) \sim 0.5 \text{ eV}$ , we find that the expansion parameter equals unity when the electric field strength  $|\mathcal{E}| = 9 \times 10^7 \text{ V/cm}$ , which corresponds to an intensity of  $1 \times 10^{13} \text{ W/cm}^2$ . These values for  $|r|$  and  $(E_A - E_I - n\hbar\omega)$  are rather arbitrary so the value  $1 \times 10^{13} \text{ W/cm}^2$  is simply an order of magnitude estimation of the maximum allowable intensity for this formulation to be valid. An important aspect of LOPT is the frequency dependence contained in the denominator. For high laser frequencies the term  $(E_A - E_I - n\hbar\omega)$  will be larger on average than for low frequencies. For example, a factor of four increase in the photon energy can be accompanied by an increase in the electric field  $\mathcal{E}$  by a factor of four without causing Eqns. (1.1) and (1.2) to become invalid. This translates into an intensity increase of a factor of 16 which corresponds to  $2 \times 10^{14} \text{ W/cm}^2$  in the example given above. Eqns. (1.1) and (1.2) also become invalid when one of the energy denominators approaches zero. This special case will be discussed in section (I.F) which deals with resonantly enhanced ionization.

Expression (1.2) can be put into a simpler looking form:  $W^{(N)} = \sigma_N I^N$  where  $\sigma_N$  is the total generalized cross section and  $N$  is the number of photons required to

ionize the atom ( $N=11$  for  $1.06 \mu\text{m}$  light and xenon atoms). This  $I^N$  dependence for the production of ions has been observed<sup>14,15</sup> with intensities below  $\sim 5 \times 10^{13} \text{ W/cm}^2$  which suggests that LOPT is valid for low intensities. Most experiments in our laboratory have been performed with intensities well above  $10^{13} \text{ W/cm}^2$  so the LOPT prediction of an  $I^N$  ionization rate dependence has not been in agreement with our results. At these high intensities LOPT breaks down and other types of models must be used to describe the ionization process.

### I.B. Tunneling and Suppression Models

The disagreement of LOPT with our results led us to investigate the applicability of tunneling ionization models.<sup>16</sup> Consider a static electric field interacting with an atom (see Fig. 1.1). With a sufficiently strong external field applied, the bound electrons can tunnel through the potential barrier with an appreciable probability. Tunneling ionization rates are characterized by an exponential dependence on the ionization potential ( $E$ ) and the strength of the external electric field ( $\mathcal{E}$ ).

$$W \propto \exp\left[-\frac{2(2E)^{3/2}}{3\mathcal{E}}\right] \quad (1.3)$$

Various pre-exponential factors are possible depending on the characteristics of the particular model which is used. Some tunneling models will be discussed in chapter four.

As the external field strength is increased the barrier is further suppressed to the point where a bound electron can freely escape over the barrier. At this point, the ionization rate is equal to the orbital frequency of the electron. This model is referred to as "barrier suppression ionization" (BSI)<sup>17,18</sup> "over the barrier", or "field emission"

ionization. The threshold for ionization depends on the ionization potential and the ionic charge state.

$$I_{th} \propto \frac{E^4}{Z^2} \quad (1.4)$$

The exact expression is derived in chapter four. We find that a tunneling or barrier suppression model works quite well to describe the experiments done in our laboratory where the frequency of the laser is small compared to the electron orbital frequency.

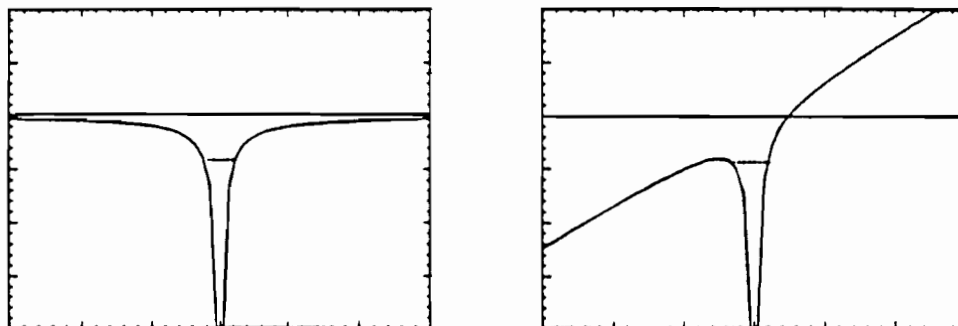


Fig. 1.1 (a) A bound state in a Coulomb potential and (b) Superposition of a Coulomb and a static electric field potential with the same bound state. The electron can now tunnel out quite easily.

### I.C. Keldysh Approximation

A third theoretical approach was introduced by Keldysh<sup>19</sup> in 1964. He used perturbation theory (basically just Fermi's Golden Rule) to calculate the probability of transition from a bound state to a Volkov<sup>20</sup> state. A Volkov state is an exact solution of Schrödinger's equation for a free electron oscillating in a monochromatic electric field. In electric field gauge it is given by<sup>19</sup>

$$\Psi = \exp\left\{\frac{i}{\hbar}\left(\mathbf{p} + \frac{e\mathcal{E}}{\omega}\sin\omega t\right)\mathbf{r} - \frac{i}{\hbar}\int_0^t dt' \frac{1}{2m}\left(\mathbf{p} + \frac{e\mathcal{E}}{\omega}\sin\omega t'\right)^2\right\}, \quad (1.5)$$

where it is assumed that the electron is oscillating in an electric field of the form  $\mathcal{E}(t) = \mathcal{E}\cos(\omega t)$ . This approach has acquired the title "the Keldysh approximation." Various modifications to Keldysh's original model have been proposed.<sup>21-24</sup> "Keldysh like" models continue to be among the most commonly used analytical models for describing high-intensity laser-atom interactions. In the high-field, low-frequency limit these models agree with tunneling models and in the low-field, high-frequency limit some of the modified theories predict an ionization rate with an  $I^N$  dependence which is in agreement with LOPT.

The distinction between the multiphoton regime (where LOPT is valid) and the tunneling (or "field ionization") regime can be quantified with the "Keldysh gamma parameter." This is a dimensionless parameter which appears in Keldysh's derivation for the ionization rate. Its value is  $\gamma \gg 1$  in the multiphoton regime and  $\gamma \ll 1$  in the tunneling regime and it is defined as

$$\gamma = \frac{\omega_L \sqrt{2Em}}{e\mathcal{E}} \quad (1.6)$$

where  $\omega_L$  is the laser frequency,  $E$  is the ionization potential,  $m$  and  $e$  are the electron mass and charge, and  $\mathcal{E}$  is the field strength of the laser. Keldysh explains<sup>19</sup> that a physical understanding of  $\gamma$  can be obtained through the following argument.

A bound electron in an oscillating electric field feels a potential as shown in Fig 1.1b. The barrier width is of the order of  $E/e\mathcal{E}$  and the average electron velocity is of the order of  $(E/m)^{1/2}$ . We are only interested in an order of magnitude estimation so we can say the tunneling frequency  $\omega_t = \text{velocity}/(\text{barrier width}) = e\mathcal{E}/(2mE)^{1/2}$ . If  $\gamma$  is then defined as  $\gamma = \omega_L/\omega_t$  we obtain expression (1.6). With this definition of  $\gamma$  it is easy to see that the regime where  $\gamma \ll 1$  would be dominated by tunneling effects and the regime where  $\gamma \gg 1$  would have only small contributions due to tunneling and the ionization must be dominated by another type of process (MPI). Clearly the "derivation" given above is not rigorous, but it clarifies the physical significance of the  $\gamma$  parameter.

#### I.D. Ponderomotive Potential

It is useful to rewrite the expression for  $\gamma$  as

$$\gamma = \sqrt{\frac{E}{2U_P}}, \quad (1.7)$$

where  $U_P = e^2\mathcal{E}^2/4m\omega_L^2$  is referred to as the ponderomotive potential.<sup>25,26</sup> The ponderomotive potential can be described as follows. When an atom is ionized by an intense laser field the freed electron is not in free space, but is borne into an oscillating electro-magnetic field. This field places a force upon the electron causing it to oscillate at the field frequency. The energy associated with this oscillation can be calculated classically or quantum mechanically (the same result is obtained using either method).

The electric field can be described as  $\mathcal{E}(t) = \mathcal{E}_0 \cos(\omega t)$ . The resulting equation of motion for an electron in this field is that of a simple harmonic oscillator:  $ma = e\mathcal{E}_0 \cos(\omega t)$ . The solution is

$$x(t) = \frac{-e\mathcal{E}_0}{m\omega^2} \cos(\omega t) \quad (1.8)$$

with a velocity of

$$v(t) = \frac{e\mathcal{E}_0}{m\omega} \sin(\omega t). \quad (1.9)$$

The average kinetic energy associated with this quiver motion is  $U = m\langle v^2 \rangle / 2$ . This quiver energy is referred to as the ponderomotive energy and is given by

$$U_P(I) = \frac{e^2 \mathcal{E}_0^2}{4m\omega^2}$$

$$U_P(I) [eV] = 9.33 \times 10^{-14} I [W/cm^2] \lambda^2 [\mu m]. \quad (1.10)$$

This means that a free electron in a laser field will have an average kinetic energy which is greater than zero. For laser induced ionization a bound electron must acquire an energy equal to its ionization potential plus whatever quiver energy it needs to remain in the laser field. This additional energy which is required is equivalent to an ac Stark shift of the upper lying atomic levels by an amount equal to the ponderomotive energy. Thus the ponderomotive energy acts like a potential.

A set of experiments by Bucksbaum *et al.*<sup>27</sup> shows convincing evidence for the existence of the ponderomotive potential. The experiment observed the scattering of free electrons from the focus of a laser beam. The direction of the electron beam and the laser beam were perpendicular to each other and they were both pulsed sources. By

varying the time delay between the two pulses, Bucksbaum was able to measure the energy of electrons which were transmitted through the laser focus as a function of pulse timing (see Fig. 1.2). The electron beam which they used consisted of electrons at four discrete energies separated by about 1.5 eV. This accounts for the presence of four electron peaks for each delay setting. The vertical dotted lines in Fig. 1.2 represent the unshifted energies of the electrons. If the electrons reached the focus when the laser was already present they were decelerated, and if the laser arrived as the electrons were slightly beyond the focus they were accelerated. The amount of acceleration or deceleration was consistent with the value of the laser's ponderomotive potential (8 eV using a wavelength of 1064 nm).

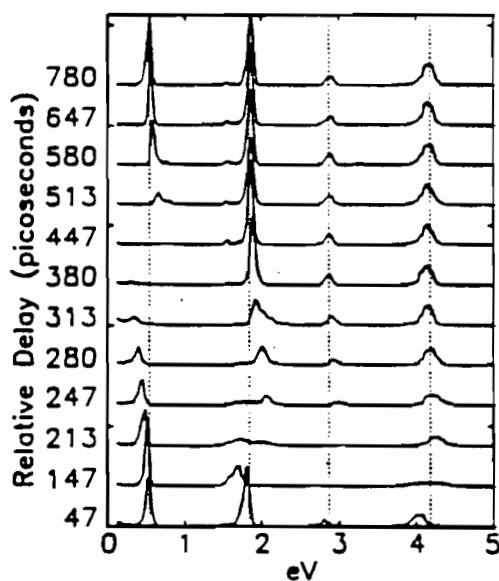


Fig. 1.2 Electron energy spectra. The numbers at the left show the time advance between the electron pulse and the laser pulse. The electron pulse is generated 180  $\mu\text{m}$  from the laser focus. [from Fig. 2 of reference 27]

## I.E. Ion Yield Experiments

The measurement of ionic spectra is a common technique which is used to gain insight into the physical processes which occur at high laser intensities. One particular advantage of this is that it is easy to determine the degree of ionization whereas this information can be very difficult or impossible to extract from electron or photon spectra. The interpretation of any data which is collected in a high intensity laser experiment is complicated by the spatial distribution of the laser intensity.

Focused laser beams are used in all high-intensity laser experiments consequently a large gradient exists in the spatial dependence of the laser intensity. This spatial dependence is a very important factor to consider when interpreting experimental data. Theoretical models for laser ionization typically predict an ionization rate, so to determine the number of ions which are produced we must multiply the rate by the number of atoms illuminated and by the pulse length. This means that the volume of the laser focus and the density of particles at the focus must be known in order to compare experimental results with theoretical predictions.

Figure 1.3 shows a contour plot of the laser intensity as a function of the cylindrical coordinates  $(r,z)$ . Azimuthal symmetry is assumed. For very high laser intensities the ionization probability within a given intensity contour might be 100%. For example if the 80% contour has intensity  $I$  with an ionization rate of  $10^{14} \text{ s}^{-1}$ , total ionization occurs within about 10 fs. This means that all atoms within the 80% contour will be ionized for our laser pulse which is approximately Gaussian with FWHM of 1 ps. If the peak laser intensity is doubled, the intensity  $I$  will then correspond to the 40% contour which has a larger volume than the 80% contour. The number of ions produced will then be equal to the total number of neutral atoms which were originally

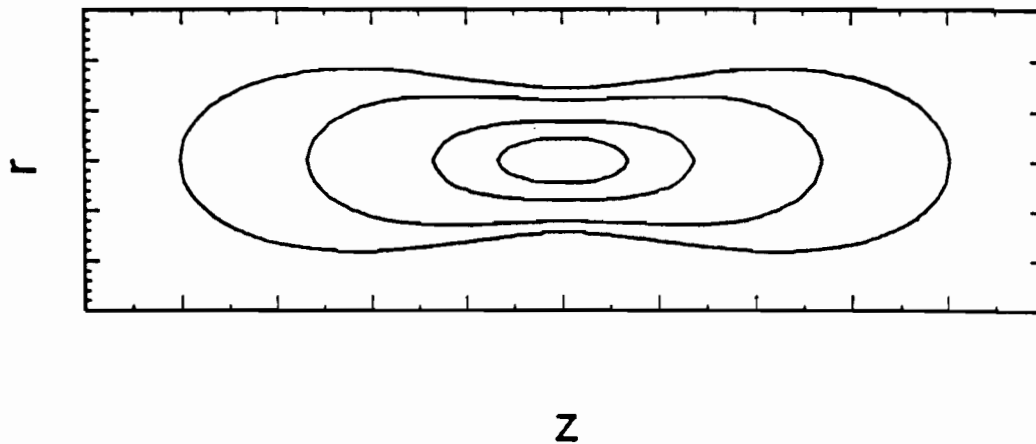


Fig. 1.3 Contour plot of the laser intensity distribution near focus. The 80%, 50%, 20%, and 10% intensity contours are shown. The graph assumes focusing by an  $f/1$  lens. The dimensions scale with  $f\#$  as  $r \propto f\#$  and  $z \propto f\#^2$ .

within the 40% contour. The increase in ion production in this case is not due to the increased ionization rate but is due to a larger focal volume. This idea is commonly referred to as expansion of the focal volume.

The intensity shell where charge state  $n$  is produced will contain few ions of differing charges. Any shell of higher intensity will be comprised of mainly the  $n+1$  charge state and a lower intensity shell will contain mainly the  $n-1$  charge state. As the peak intensity is increased the volume of any intensity shell<sup>28</sup> will expand as  $I^{3/2}$ . Figure [1.4] shows a logarithmic plot of ion number versus laser intensity and this  $I^{3/2}$  dependence can be seen in the first charge state for high intensity. Very little

information regarding the ionization rate can be obtained from data which is collected in this regime since the ionization has been saturated ( $\int_{-\infty}^{+\infty} dt W(t) \sim 1$ ).

For low laser intensities the ionization probability will be small so it is valid to assume the number of neutral atoms at the focus remains constant even after the laser pulse has passed. We can see the validity of this assumption in Fig. 1.4. The various charge states which are created account for the multiple curves. The first charge state follows an  $I^N$  dependence which is the predicted ionization rate dependence in LOPT for an  $N$  photon ionization. This  $I^N$  dependence might be expected to be affected by focal volume expansion effects but numerical simulations show that the intensity dependence of the ion number is insensitive to focal volume expansion effects for low ion number. As the laser intensity is increased the slope of the ion curve lessens. This is due to saturation of the focal volume which means that the neutral atoms are being depleted and it is no longer valid to approximate their number as constant.

The group in Saclay, France [4.15.29-35] has made a large experimental contribution to the field of MPI both in terms of volume and quality of data and the number of new phenomena discovered. They have done experiments to detect ions, electrons, and photons. Experiments which measured ion spectra are most relevant to the work described here. Log-log graphs of the number of ions produced versus laser intensity show curves which have a slope of  $N$  [see Fig. 1.4], thus demonstrating the  $I^N$  dependence for the ionization rate which is predicted by LOPT. These experiments were done mainly in the regime of  $\gamma > 1$ , although the data for neon and helium demonstrated an  $I^N$  dependence even for  $\gamma < 1$ . All the Saclay experiments which were published prior to 1990 used 30-50 ps laser pulses at either 1  $\mu\text{m}$  or 0.5  $\mu\text{m}$

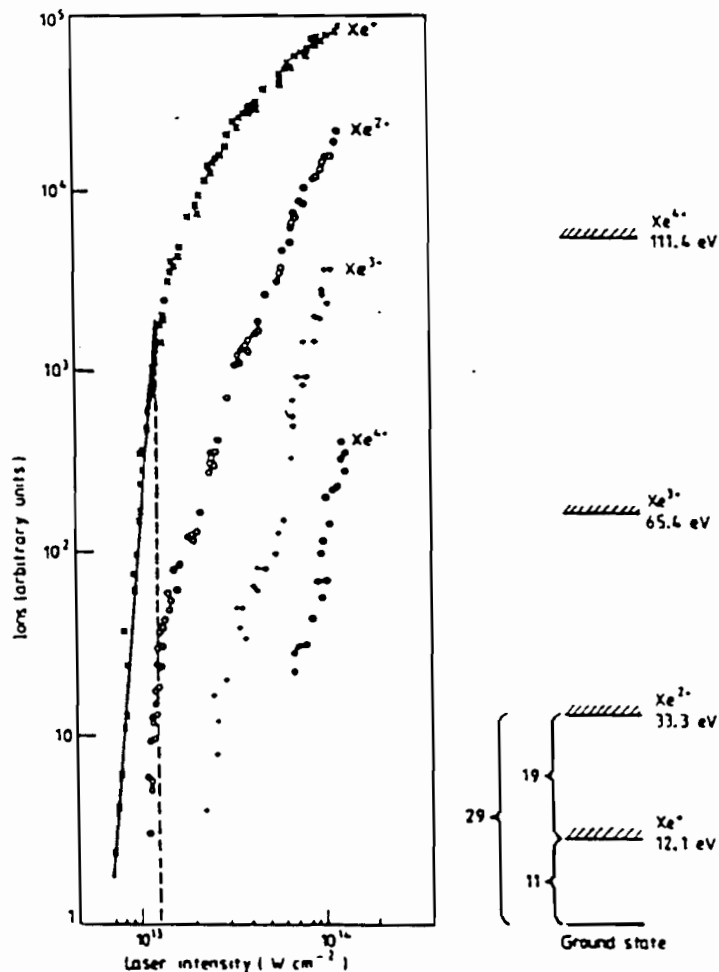


Fig. 1.4 The number of xenon ions produced as a function of laser intensity for  $\tau = 50$  ps and  $\lambda = 1064$  nm. The  $I^N$  dependence, saturation of the focal volume, and direct ionization are features of the data which are described in the text. [from Fig. 2 of reference 14]

wavelength. Recent results<sup>35</sup> have been obtained with a 1 ps laser pulse at the same wavelength and preliminary indications are that the first charge state of xenon still follows this  $I^N$  dependence.

Another feature which can be seen in the data in Fig. 1.4, but is more clearly seen at a shorter wavelength (532 nm) in Fig. 1.5, is the transition from a direct

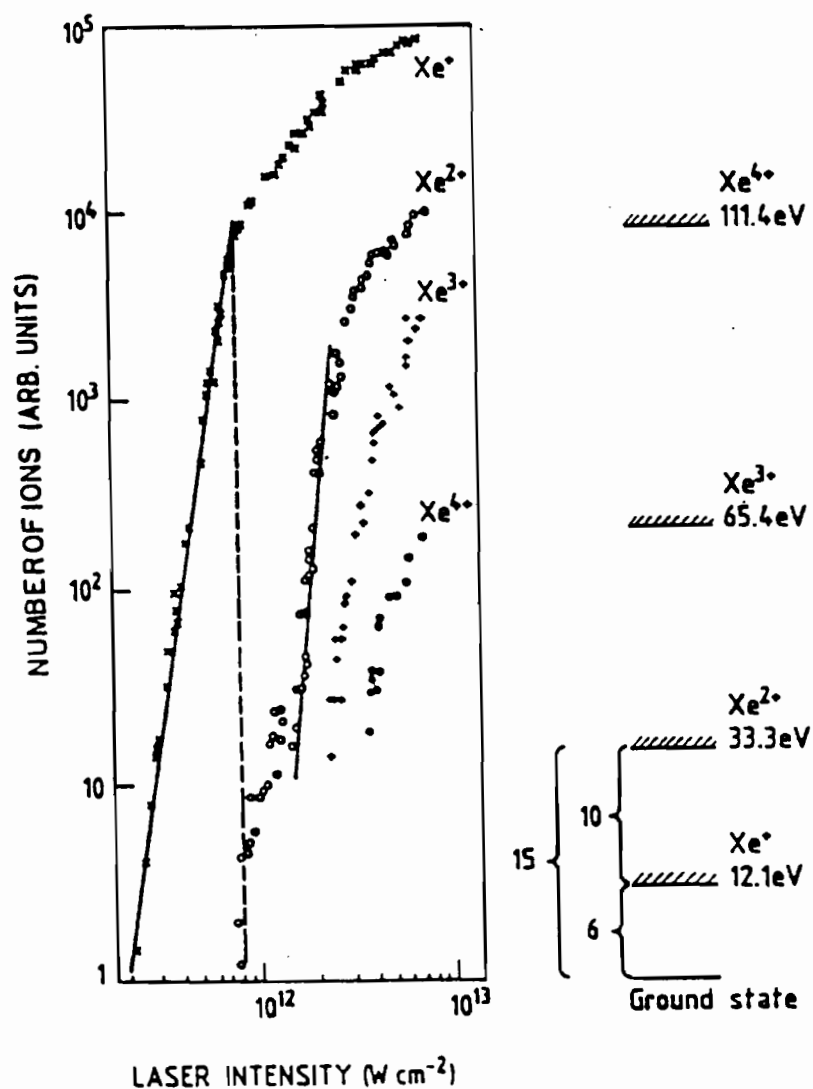


Fig. 1.5 Production of xenon ions using a 50 ps laser pulse at 532 nm. Direct and sequential ionization processes are clearly present in the second charge state. [from Fig. 3 of reference 15].

ionization process to a sequential process for the second charge state. For intensities where the ionization probability is much less than one, the second charge state appears at an intensity only slightly higher than the first charge state. The  $I^N$  dependence of the second charge state suggests a value of  $N$  which is equal to the number of photons

required to remove two directly from the neutral atom ( $N = 15$  in Fig. 1.5). As the laser intensity is increased the focal volume saturates and there are no more neutral atoms at the center of the focal volume. The intensity at which saturation of the focal volume occurs is commonly referred to as the "saturation intensity". When the first charge state reaches saturation, the production of the second charge state levels off until a higher intensity is reached. In Fig. 1.5 the production of doubly charged ions then resumes its  $I^N$  dependence, this time with  $N$  being equal to the number of photons necessary for ionization of a singly charged ion ( $N = 10$  in Fig. 1.5).

#### **I.F. Resonantly Enhanced Ionization: Ion Spectra**

A group at Lawrence Livermore National Laboratories<sup>24,36-39</sup> has done a large amount of experimental work using 1 ps pulse length dye lasers at visible and ultraviolet wavelengths. The results of experiments done at 586 nm show agreement with a modified "Keldysh approximation" theory.<sup>24</sup> This theory will be reviewed in section (IV.F). Other experiments done by this group have investigated resonantly enhanced MPI.<sup>37-39</sup>

Resonant enhancement occurs when the laser frequency is such that the energy of an integral number of photons corresponds to the energy separation of some excited state and the ground state. This enhancement appears in Eqns. (1.1) and (1.2) when one of the energy denominators goes to zero. Clearly these expressions are invalid for resonant ionization unless they are modified to account for the ac Stark shift due to the ponderomotive potential and the linewidth of the resonant state. The ionization rate due to the resonant term will be much larger than all the other terms if the linewidth is

sufficiently small. Equation 1.2 then takes the form of the Breit-Wigner formula.<sup>12,40</sup>

$$W = \frac{\Omega^2}{4} \frac{\gamma_2}{(\omega_R - \omega_I - N\omega + \alpha I)^2 + (\Gamma/2)^2} \quad (1.11)$$

where  $\Omega$  is the Rabi frequency (the transition rate from the initial state to the resonant level),  $\gamma_2$  is the ionization rate from the resonant level to the continuum,  $\Gamma$  is the width of the resonant level, and  $\alpha I$  represents the ac Stark shift of the resonant level. The width ( $\Gamma$ ) of the resonant state is determined by the largest of the following: the radiative lifetime of the level,  $\gamma_2$ , or the bandwidth of the laser. In resonantly-enhanced multiphoton ionization (REMPI)  $\gamma_2$  is typically the largest of these parameters.

The experiments described in references [37-39] used the frequency-doubled output of a dye laser which provided a usable wavelength range from 285 nm to 310 nm. Krypton has a three-photon resonance near 289 nm which enhances four-photon ionization. The intensity of the laser was varied and the Stark shift of the resonant level was observed. An intensity dependent broadening of the level also occurred. Due to the large photon energy it is possible to describe the level shift and broadening satisfactorily with Eqn. (1.11). A more sophisticated model which uses multichannel-quantum-defect theory<sup>41,42</sup> also describes the data quite well.

It is interesting to note that the ion curves shown in reference [38] have a slope of 3 for resonant ionization and a slope of 4 for the non-resonant ionization curves. These slope values are consistent with the predictions of LOPT.

## I.G. Resonantly Enhanced Ionization: Electron Spectroscopy

The study of resonantly enhanced MPI is an issue which has been explored by many research groups. Several years ago experimental results were obtained at Bell Laboratories which showed that transient resonances can dominate MPI processes which were originally thought to be non-resonant.<sup>43</sup> This is possible since bound levels in the atom can be Stark shifted into resonance as the laser pulse passes over the atom. This shifting of bound levels into resonance has been observed by several groups.<sup>43-47</sup> Experiments which demonstrated the effects of intermediate resonances involved measuring the energy of ionized electrons. Very short laser pulses were used so that the electrons would not have time to be accelerated by the ponderomotive gradient (here very short means 1 ps to 100 fs). Consequently, the energy with which they were borne was the energy which was measured by the spectrometer. Numerous peaks can be seen in the electron energy spectrum [see Fig. 1.6].

As the laser intensity sweeps bound states into resonance with an integral number of laser photons, the electron yield is increased. Since the ionization potential is shifted at the same time, each electron peak corresponds to a different level coming into resonance. The energy of each peak is approximately  $(N\hbar\omega - E - U_P)$ . The presence of these resonance peaks verifies that the bound levels in the atom are Stark shifted due to the presence of the ponderomotive potential. This level shift is demonstrated in Fig. 1.7. Only one intermediate level is shown, but in a real atom there are many intermediate levels which might be shifted into resonance.

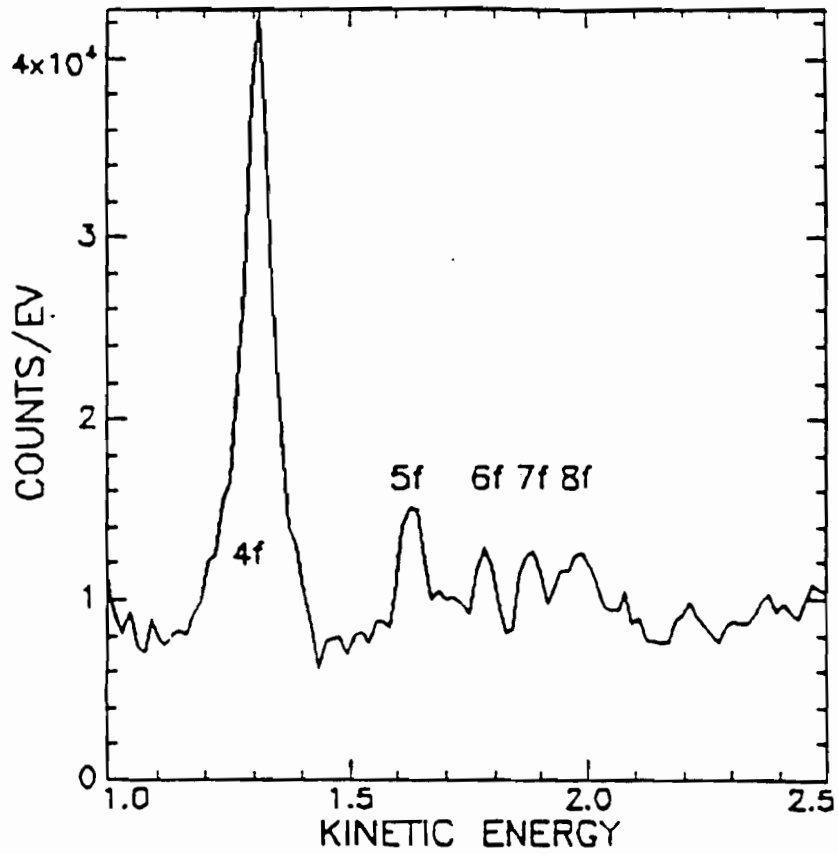


Fig. 1.6 Electron energy spectrum from reference [46]. The peaks correspond to various levels coming into resonance as the ponderomotive potential changes with laser intensity. The energy of the electron peaks is approximately given by  $(N\hbar\omega - E - U_P)$ .

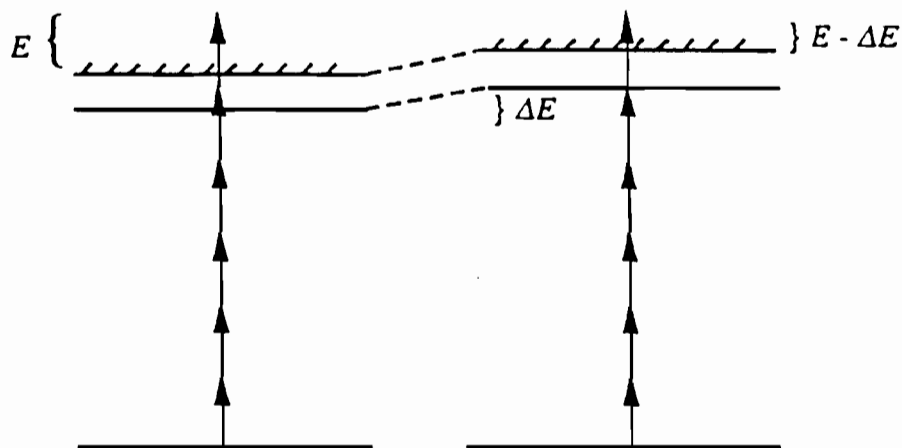


Fig. 1.7 Initially non-resonant six-photon ionization becomes enhanced when an upper level is Stark shifted into a five-photon resonance. The energy of the freed electron decreases by an amount which is approximately equal to the value of the ponderomotive potential which is present at the time resonant enhancement occurs.

#### I.H. Additional Ionization Experiments

Contributions to the study of MPI in noble gases have been made by numerous other groups. Here I will briefly describe the work of some additional groups that have made a significant contribution to the study of MPI processes.

A group at the Australian National University has used a laser ( $1 \mu\text{m}$ , 25 ps) which is similar to that of the Saclay group's. They studied MPI in argon and helium by collecting electron spectra.<sup>48,49</sup> Electrons liberated at the laser focus acquired a directed kinetic energy which was approximately equal to the ponderomotive potential of the laser field. As the laser energy was increased multiply charged ions were created. The higher charge states were created at higher laser intensities which had larger ponderomotive potentials thus giving the electrons a greater kinetic energy. The electron energy spectra showed quantized jumps in the number of electrons detected

versus electron energy. These jumps were determined to be a result of the creation of different charge states in the gas. From these data they were able to obtain the threshold intensities for ionization of various charge states of argon and helium. The threshold intensities for charge states of argon were significantly higher than those reported by the Saclay group (by as much as a factor of 10) but the helium threshold intensities were consistent between the two groups. All ionization was determined to occur in the tunneling regime ( $\gamma < 1$ ).

A CO<sub>2</sub> laser with a 10- $\mu\text{m}$  wavelength is the ideal system to study high ponderomotive potential effects since the ponderomotive potential is proportional to the wavelength squared (see Eqn. 1.10). A group at Laval University<sup>50-54</sup> has obtained both ion and electron spectra resulting from the ionization of xenon gas using a 1-ns CO<sub>2</sub> laser. The electron spectra are similar to those seen by the Australian group<sup>48,49</sup> in that they show jumps in electron number as a function of electron energy. Again, the jumps are the result of different charge states being created in the laser focus with the freed electrons acquiring a kinetic energy which is equal to the ponderomotive potential at the location which they were created. The measured threshold intensities required for ionization were found to agree with those obtained from ion spectra and the measured ionization rates were found to be in agreement with the tunneling theory<sup>54</sup> which is discussed in section (IV.C.).

Variable pulse length ion experiments have been done with a dye laser (0.62  $\mu\text{m}$  wavelength) where pulse lengths of 22, 90, or 900 fs were used.<sup>55</sup> The results showed a decrease in the number of ions produced as the pulse length was decreased. This result is expected since the ionization probability decreases with the pulse length if the ionization rate remains constant. It is found that the ion production

decreases by less than a factor of ten when the pulse length is decreased from 900 to 90 fs. Further, the ion production is decreased by more than a factor of five when the pulse length is decreased from 90 to 22 fs.

The authors suggest that at such short pulse lengths the presence of transient resonances has little effect on the ionization rate. This is due to the rapid change in the ponderomotive potential. The 22 fs pulse contains only 11 optical cycles and for a peak intensity of  $10^{14}$  W/cm<sup>2</sup> the maximum ponderomotive shift is 0.4 eV/cycle which means that any transient resonance will enhance the ionization rate for a few cycles at most. LOPT predicts an  $I^7$  dependence for xenon at this wavelength. This dependence is seen with the 900 fs pulses but the shorter pulses display approximately an  $I^4$  dependence. This suggests a transition from an MPI process to a field ionization process even though  $1 < \gamma < 3$  for all three pulse lengths.

Another group with a large experimental contribution to MPI is a group<sup>56-58</sup> at the University of Illinois. They have done ion, electron, and harmonic experiments using excimer lasers with wavelengths of 193 nm or 248 nm and pulse lengths between 0.5 ps and 5 ps. Ion experiments performed in the  $1 < \gamma < 8$  regime showed agreement with tunneling theories<sup>58</sup> despite the fact that a multi-photon approach is expected to work better in this regime. Threshold intensities for ionization were consistent with the Australian National University's results and with some of the Saclay results (helium and neon). The higher Z gases (argon, krypton, and xenon) showed a discrepancy between the Saclay and Illinois data with the Saclay threshold intensities occurring at values which were as much as a factor of 10 lower than those of the Illinois group.

Excimer lasers with subpicosecond pulse lengths have also been used by a group at Los Alamos National Laboratories.<sup>59</sup> They have used a KrF laser at 248 nm

wavelength and 700 fs pulse length as well as a XeCl laser at 308 nm with 350 fs pulse length to perform experiments at intensities up to  $5 \times 10^{18}$  W/cm<sup>2</sup>. They have reported ion production of xenon up to the 13th charge state.

The experiments done at the University of Rochester Laboratory for Laser Energetics (LLE) were initially started to investigate the ionization of noble gases using a 1-ps pulse length, 1- $\mu$ m wavelength laser. The short laser pulse length was possible because of a new technique which was developed at LLE. This technique will be described briefly in chapter two. The results of these experiments seemed not to agree with results from Saclay which were done at the same wavelength but with a 50 ps pulse length. The 1-ps results agree well with tunneling or barrier suppression models and with the Australian National University's 25 ps electron experiments whereas the 50-ps results from Saclay had agreed with lowest order perturbation theories. This led to a second set of experiments whose purpose was to investigate this apparent discrepancy and to attempt to resolve some of the discrepancies among the threshold intensities reported by various groups.

## **I.I. Organization of Document**

I will first discuss the laser and experimental equipment in chapter two. This includes a review of the uncertainties which occur in the data, in particular the difference between absolute and relative uncertainties in the laser intensity is discussed. Techniques for the measurement of the laser intensity and for the acquisition of ion spectra are presented. A survey of the ionization of five noble gases as a function of laser intensity will be presented in chapter three, followed by a discussion of the experimental data and a comparison to results obtained by other research groups. Chapter four reviews some theoretical models and compares theoretical predictions to

the data. The Coulomb barrier suppression model (BSI) and a quasiclassical tunneling model are found to be in the best agreement with the data. Chapter five presents some additional experiments which have been performed and suggests further work which could be done. Chapter six gives a summary and conclusion.

## CHAPTER TWO

### EXPERIMENTAL APPARATUS

This chapter describes various aspects of the experiments. First, the laser characteristics and method of operation are described followed by a discussion of diagnostic measurements which are performed to characterize the laser pulses. This includes two methods for measuring the intensity with a discussion of the related errors in these measurements. The method for acquisition and analysis of ion spectra is then described.

#### II.A. The Laser

The laser used for these experiments is a high-power (~0.5 TW) Nd:glass laser based on the concept of chirped pulse amplification and compression (CPA).<sup>60-63</sup> The CPA design was developed to increase the power output of solid state lasers without increasing the aperture size of the amplifiers. Prior to the introduction of CPA lasers, the power output of solid state lasers was limited by intensity-dependent non-linear effects in the lasing medium, which is typically some type of glass or crystal that has been doped with an impurity. The impurity element is actually the gain medium and the glass or crystal serves as a host. For high power laser beams, non-linear effects in the glass or crystal contribute significantly to the index of refraction which results in the introduction of a phase error in the wavefront of the laser. To first order, non-linear effects in the medium are proportional to the intensity of the laser beam.

Non-linear effects are undesirable since severe phase error can lead to a lensing effect in the laser rod known as self-focusing. When these lensing effects begin, the

local intensity can increase thereby causing stronger non-linear effects and more lensing. The process builds on itself and can lead to severe damage in the rod. This damage consists of linear sections of the rod which have been ionized. The ionized sections are no longer transparent which destroys the optical quality of the rod. Additionally, the phase error results in a decreased ability to focus the laser beam to a small spot and hence limits the maximum intensity which can be achieved. There are three ways to decrease the beam intensity inside the laser rod: 1) increase the cross-sectional area of the rod, 2) decrease the beam energy, or 3) temporally lengthen the laser pulse. The first method is undesirable for several reasons. Glass laser rods can become expensive for large sizes, and as the cross-sectional area is increased the uniformity of pumping is reduced, which results in somewhat lower quality spatial characteristics in the laser beam. The repetition rate of the laser is also reduced for large aperture rods due to the extra time that is required to allow the rod to return to thermal equilibrium between shots. The use of low energy beams or long-pulse laser beams makes high-power experiments impossible unless the CPA technique is used.

The CPA laser design takes advantage of the large energy storage capabilities of glass amplifiers while avoiding problems due to high-intensity non-linear effects. This is accomplished by making the laser pulse long in time to extract the energy efficiently while keeping the peak power levels relatively low. After the light has been amplified to the desired energy the pulse is compressed to a shorter length. The obtainable compression ratio is typically as high as 100 or 1000. The CPA design allows laser pulses to be expanded and recompressed using the dispersive qualities of optical fibers and diffraction gratings. Many variations on the original CPA design can be used and the two designs which we have employed are described below<sup>60,63</sup> [see Fig. 2.1].

A 100-MHz train of approximately 55-ps pulses is generated by an acousto-optically mode-locked Nd:YLF oscillator at the wavelength  $1.053\ \mu\text{m}$ . The 55 ps pulses from the oscillator are bandwidth limited which means the pulse length cannot be shortened unless additional bandwidth is acquired somehow. These pulses are injected into an 800 meter single-mode optical fiber where they are temporally stretched and frequency chirped by group-velocity dispersion and self-phase modulation (SPM).<sup>64</sup> SPM in the optical fiber increases the bandwidth from about  $0.3\ \text{\AA}$  to about  $40\ \text{\AA}$ , and group velocity dispersion in the fiber causes the output pulses to be frequency chirped in time. The pulses are further stretched by a pair of expansion gratings to a pulse length of approximately 300 ps.<sup>65,66</sup> After amplification, the pulses can be compressed to a length which is much less than the original 55 ps. This is possible because of the linear frequency chirp which is present. A grating pair can compress a chirped pulse as shown in Fig. 2.2.

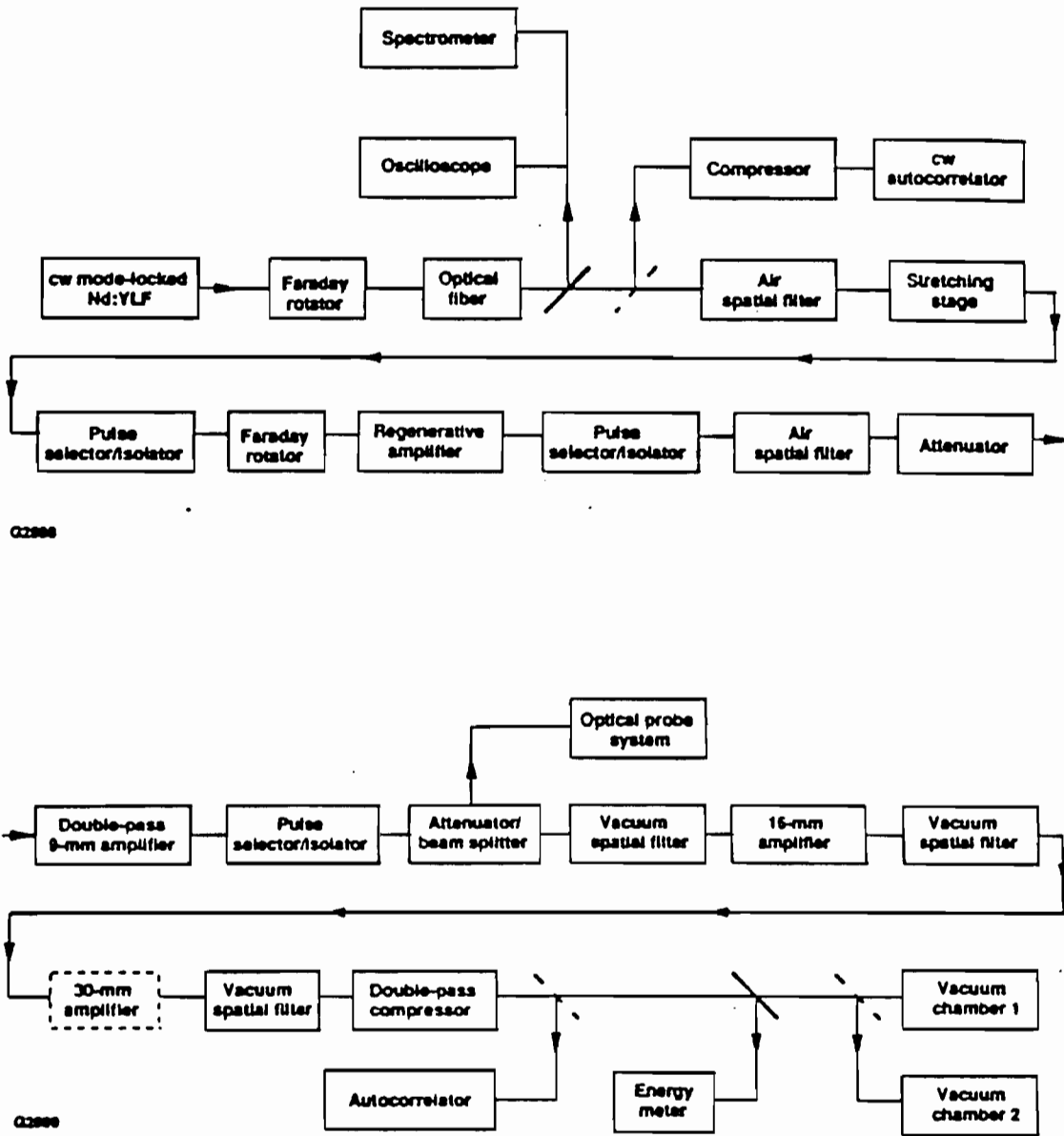


Fig. 2.1 The parts of the CPA laser system.

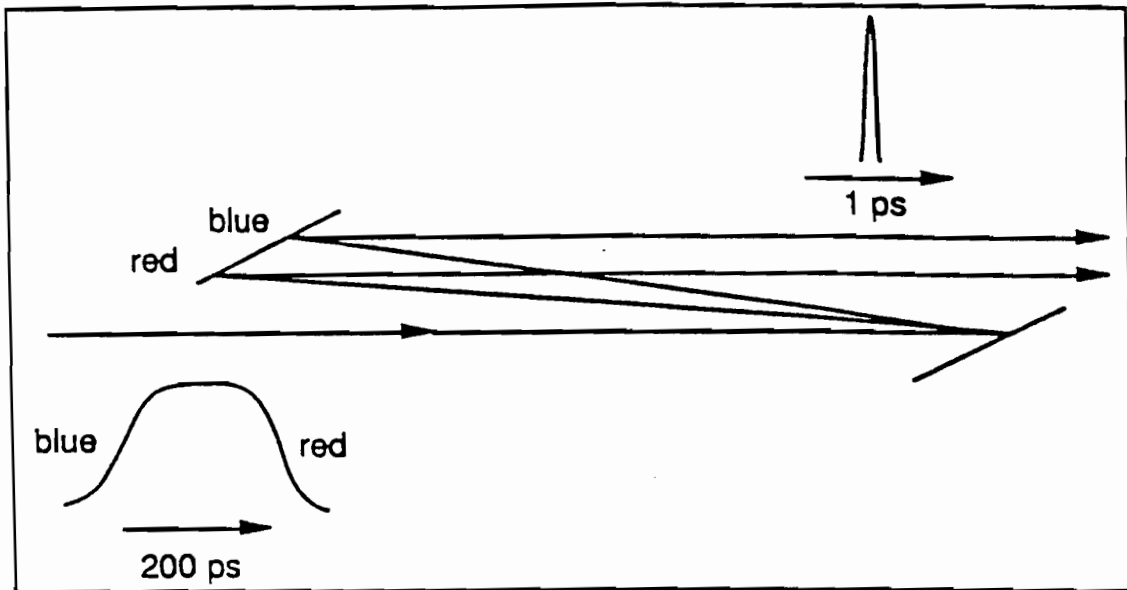


Fig. 2.2 Diagram showing how a chirped pulse can be compressed with a grating pair. The blue ray travels a shorter distance so it can catch up to the red ray. A single pass results in an oval beam and a double pass results in a circular beam. If a telescope with magnification of one is placed between the gratings, the separation of the gratings can be effectively negative. This results in a temporal expansion of the pulse.

Self-phase-modulation which occurs in the optical fiber is due to the optical Kerr effect.<sup>63,67</sup> The index of refraction of a medium is characterized by the constant  $n_0$  but at high intensities a non-linear contribution to the index of refraction becomes significant. The index of refraction can then be described by

$$n(z,t) = n_0 + n_2 I(z,t). \quad (2.1)$$

The phase of a light pulse traveling through this medium can be found by integrating  $n(z,t)$  over the length of the medium.

$$\phi(t) = \phi_0 + \frac{2\pi}{\lambda} \int_0^L n_2 I(z,t) dz. \quad (2.2)$$

In an optical fiber the light is approximately a plane wave so the integral over  $dz$  yields a term ( $n_2 I L$ ). This phase determines the propagation of the wave as

$$e^{i(\omega t - kz)} = e^{i(\omega t - \phi(t))}, \quad (2.3)$$

and the instantaneous frequency shift due to SPM can then be found from the derivative of  $\phi(t)$

$$\Delta\omega(t) = -\frac{d\phi(t)}{dt} = -\frac{2\pi}{\lambda} n_2 L \frac{dI(t)}{dt}. \quad (2.4)$$

For most media in the optical wavelength range  $n_2$  is positive, which results in a red shift of the frequency for increasing intensity and a blue shift for decreasing intensity. This, along with group velocity dispersion, creates a chirped pulse of about 100 ps and 40 Å at the output of our fiber. Near the center of the pulse ( $t_0$ ) the frequency chirp is approximately linear in time. This is important since a linear chirp can be compressed with a grating pair. Non-linear contributions to the chirp cannot be compressed (actually a *small* third order contribution can be corrected by tuning the angles of the compression gratings).

A single pulse with an energy of about 1 nJ is selected from the train of chirped pulses and injected into a regenerative amplifier where the pulse makes approximately 80 round trips through the cavity resulting in an output energy of about 1 mJ. The cavity is a confocal design which is currently end-dumped through a plane 50% mirror. This configuration results in better pointing stability than did a Q-switch dumped cavity. The Q-switched configuration was used for the experiments described in chapter three and the end-dumped configuration was used for the experiments described in chapter five. A single pulse is selected from the regenerative pulse train before the train has reached gain saturation in the amplifier. It is important to extract a pulse

before the amplifier has reached saturation since SPM effects will occur in the laser rod near saturation. In this case, SPM is an undesirable effect since the frequency chirp which is produced in the rod will be different from the chirp out of the fiber.<sup>63</sup> With two different chirps present it would be impossible to recompress the pulse without leaving a long, low-intensity pedestal underneath the short, compressed pulse.

This pulse is further amplified with two Nd:phosphate-glass amplifiers to a maximum energy of about 500 mJ. The laser operates with a bandwidth of approximately 15 Å which is limited by gain narrowing in the amplifiers. Gain-narrowing serves a useful purpose in a CPA system. The Gaussian gain profile produces a Gaussian temporal profile since the pulse is chirped.<sup>68</sup> Additionally, most of the non-linear chirp which is present in the pulse is far from the center frequency  $\omega_0$  so the non-linear chirp will not be amplified resulting in a nearly perfectly linear chirp which can be compressed cleanly.

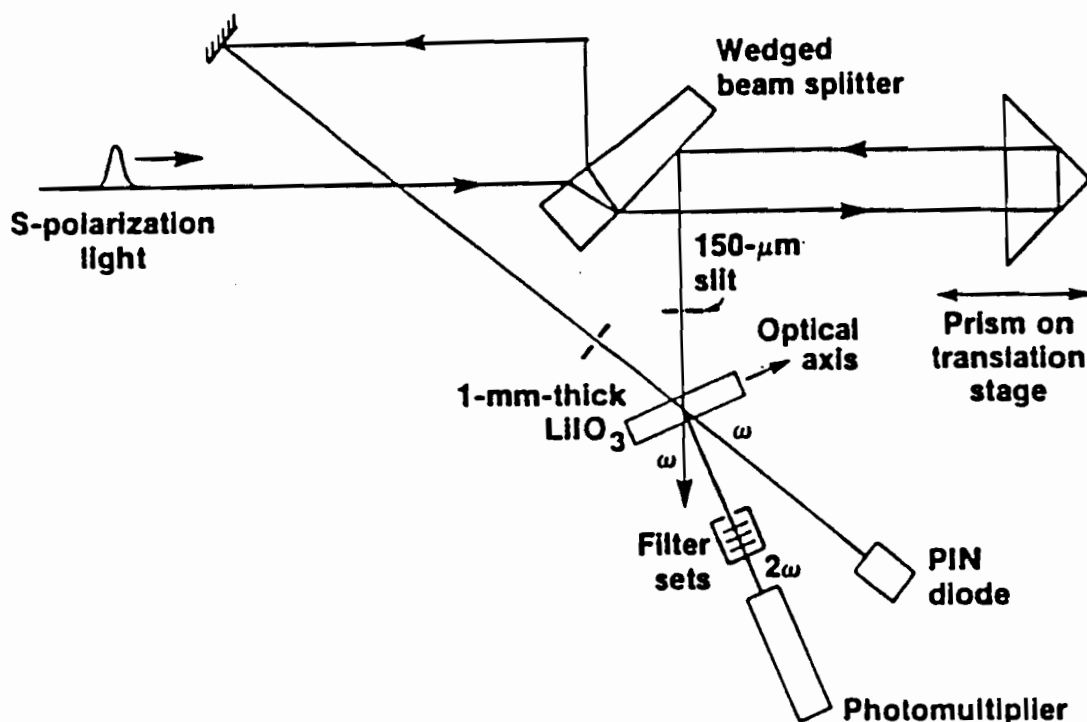
After amplification the pulse is recompressed with either a single or double pass through a 1700 l/mm grating pair to a pulse length of approximately 1 ps. Using a 20-cm-focal-length lens ( $f/5$  for single-pass and  $f/7$  for double-pass) we obtain peak intensities up to mid- $10^{16}$  W/cm<sup>2</sup>. To avoid damaging the gratings when the double-pass configuration was used, our energy was limited to 100 mJ with a maximum intensity of  $10^{15}$  W/cm<sup>2</sup>. The lower laser energy threshold results from the smaller usable area of the gratings in double-pass configuration. A double pass compression results in a more circular beam profile which can be focused to a smaller spot size than that from a single pass configuration, which produces an elliptical spot. The compression gratings were used in single-pass configuration for the experiments

described in chapter three and double-pass configuration for the experiments described in chapter five.

## II.B. Intensity Measurements

The measurement of intensities above  $10^{13}$  W/cm<sup>2</sup> is very difficult to do accurately. The experimental values for the intensity are determined by measuring the laser energy ( $E$ ), pulse width ( $T$ ), and focal spot size. We assume that the spatial distribution does not vary during the pulse so we can write  $I(r,z,t,E) = E \times F(r,z) \times G(t)$  then measure  $E$ ,  $F$ , and  $G$  independently.<sup>69</sup> Energy measurements are taken from a 4% reflection off a wedged beam splitter and are detected with a large area photodiode which has been calibrated using a pyroelectric energy meter. The pulse width is measured by a combination of methods. Second and third order correlation techniques are used to measure the absolute value of the pulse width and pulse shape<sup>70-72</sup> [see Figs. 2.3, 2.4]. Our set-up does not currently allow a second- or third-order correlation measurement on every laser shot so these measurement techniques can only give nominal values of the laser pulse width. It is possible to measure the relative pulse width on a shot-to-shot basis using a different technique.<sup>36</sup> A 4% reflection of the laser pulse is frequency doubled and the energy of the green second-harmonic light signal is measured. When the doubling crystal is operated below its saturation intensity the second-harmonic energy is proportional to the product of the fundamental power and energy ( $E_{green} = Const \times P_{ir} \times E_{ir} = Const \times (E_{ir}/T) \times E_{ir}$ ) [see appendix A]. Solving for  $T$  we see that the relative pulse width can be measured on each shot by measuring the energy of the  $1\omega$  and  $2\omega$  signals

$$T = Const \times (E_{ir})^2 / E_{green} . \quad (2.5)$$

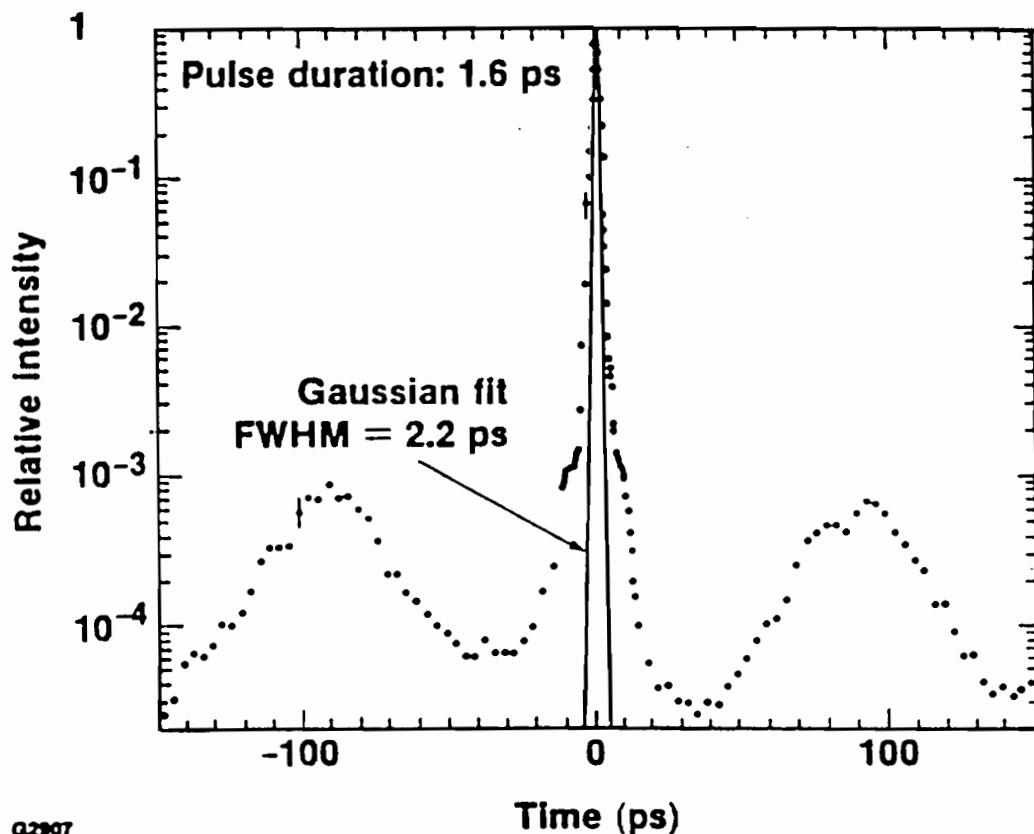


0.2908

Fig. 2.3 Autocorrelator. The wedged beam splitter and slits are used to prevent all étalon reflections from reaching the photomultiplier. The PIN diode detects shot-to-shot laser energy fluctuations. This setup becomes a single-shot autocorrelator when the slits are removed and the photomultiplier is replaced by a linear-array detector.

By comparing this relative pulse width to the second-order correlation pulse width which is obtained before and after each data run, the absolute pulse length of each laser shot in the data run can be determined.

The size of the focal spot cannot be easily measured on each shot without a CCD camera,<sup>69</sup> however, this measurement has been done many times with film and little variation from month to month is observed. Two methods are used to measure the



Q2907

Fig. 2.4 Autocorrelation trace of the compressed laser pulse for the experiments described in chapter five.

focal spot size. The first, and more accurate method, is to place a microscope objective after the focal spot to image the spot onto photographic film. A second measurement can be made by equivalent target plane (ETP) methods using a 200-cm lens. The 200-cm lens focuses the laser directly onto photographic film. If Gaussian beam propagation is assumed the spot size from a 200 cm lens has 10 times the diameter of the spot size of a 20 cm lens. This assumption was found to be quite accurate when

the results of the two methods were compared and each method produced the same spot size to within about 10%. The ETP method allows us to monitor the spot size from month to month more easily than does the microscope objective method. In the case of the shorter focal length lens it is not possible to focus the light directly onto the film since the digitizing equipment is not capable of measuring film densities on a scale smaller than a  $5 \mu\text{m}$  square. The film image obtained by either method is digitized showing an effective focal spot radius of  $12 \mu\text{m}$  for the experiments described in chapter three and  $19 \mu\text{m}$  for the experiments described in chapter five. It has been found that the spot size and shape do not measurably vary on a shot-to-shot basis. Also a comparison of low-energy laser shots where the last two amplifiers are not fired, and high-energy shots where all amplifiers are fired shows that the focal spot size and shape do not vary significantly with changes in the output laser energy.

The laser energy used in the spot size measurements had to be attenuated before the beam struck the film. This attenuation was done before the compression gratings. Additional distortions will be introduced to the beam as a result of non-linear effects in optical elements through which the compressed beam must pass. Our system has four glass elements after the compression gratings which have a combined thickness of about 5 cm. Phase distortion due to SPM can be described quantitatively by the "B-integral" which is the same as the second term in Eqn. (2.2). The value of the B-integral from these four elements is approximately 1 for the maximum intensities which were used ( $\sim 10^{10} \text{ W/cm}^2$ ). Values of about 3-5 do not cause non-linear distortion effects<sup>67</sup> when the beam is focused. This suggests that the focal spot size measurement done using low power beams is a good approximation of the spot size at full power.

It is possible to map out the focal volume by stepping the camera through the focus to obtain profiles at various planes near the beam waist. This measurement is being done to ascertain whether the focal volume we have used in calculations is an accurate description of the actual focal volume.

### **II.C. Intensity Measurements from Electron Energies**

Another method which was used to measure the laser intensity independently was to measure the energies of electrons coming from the focal volume. The electrons should acquire kinetic energy from the ponderomotive potential as they are leaving the laser focus.<sup>73</sup> Due to the short pulse length, however, they will not acquire the entire ponderomotive energy. Measured electron energies were compared to computer simulations which estimated the energy of ponderomotively accelerated electrons coming from the focus of a 1 ps pulse.

Electron energies were measured with a time-of-flight spectrometer [see Fig. 2.5]. A microchannel plate detector (MCP) was placed approximately 30 cm from the laser focus and the path between the focus and the detector was surrounded by  $\mu$ -metal to reduce stray magnetic fields. This is necessary since the earth's magnetic field will cause a 100 eV electron to have a gyro radius of about 10 cm. The time it takes ponderomotively accelerated electrons to reach the detector ranges from about 20 ns ( $\sim$ 600 eV) to about 200 ns ( $\sim$ 6 eV).

In addition to this field free setup, we have also measured the electron time-of-flight when an electric field was placed across the focal volume. The electron energy

was determined from the time of flight by the following formula

$$E = \frac{1}{2}m\left(\frac{\ell + x + \delta}{t - t_0}\right)^2 + \frac{V_1 x}{d}. \quad (2.6)$$

where  $t_0$  is a zero time offset and the remaining quantities are defined in Fig. 2.5. By varying the voltage  $V_1$  it was possible to add or subtract energy from the electrons (voltage  $V_2$  was kept at zero potential for this experiment). This produced energy measurements under different conditions which allowed us to make a least-squares fit to the three unknown parameters:  $E$ ,  $x$ , and  $t_0$ . The zero offset ( $t_0$ ) could be estimated to within about 2 ns by measuring cable lengths and light path distances. Also the value of  $x$  could be estimated from ion time-of-flight spectra since the ponderomotive acceleration of ions is very small and the ratio ( $V_1 x/d$ ) solely determines the ion velocity. Consequently the parameters  $x$  and  $t_0$  were allowed to vary over only a small range when performing the least-squares fit.

The electron energies could be measured with about a 10% uncertainty. The main contribution to this uncertainty was the limited temporal resolution of the digitizer. At  $3 \times 10^{15}$  W/cm<sup>2</sup> (about 300 eV ponderomotive potential) the maximum measured electron energy was 130 eV. This energy is consistent with that predicted by the calculation.

The calculation accounted for small fluctuations in the focal spot size and in the pulse length. These small fluctuations resulted in rather large changes in the final electron energy so this was determined to be a poor method of measuring laser intensity for short pulses. Uncertainties in the laser pulse length, focal spot size, and the electron energies resulted in an intensity measurement with an uncertainty of approximately a factor of three whereas the previously described method produced

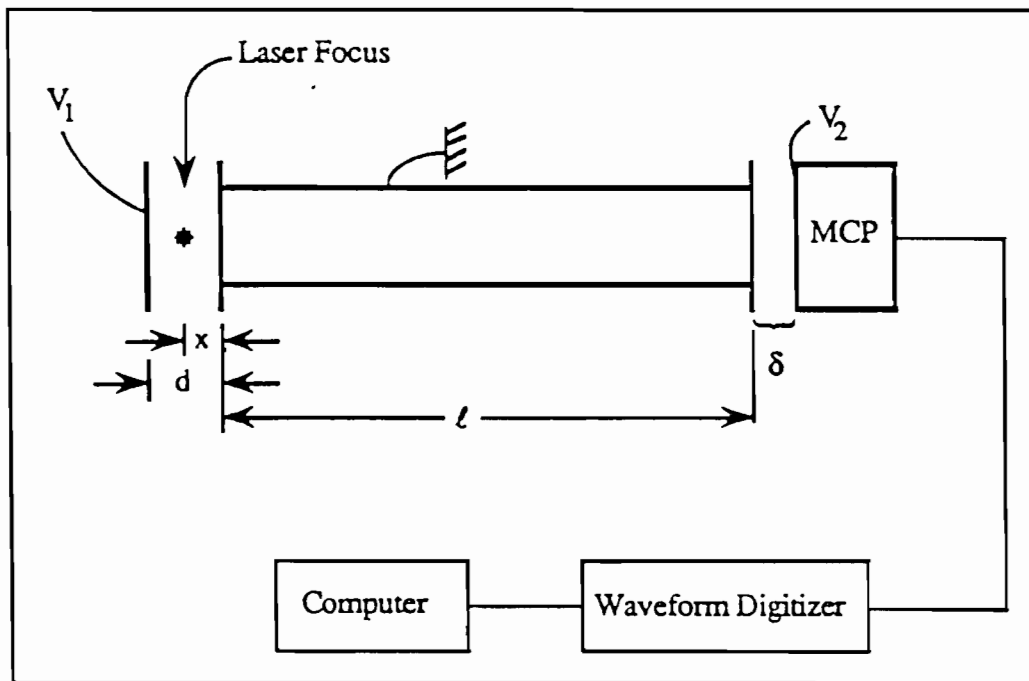


Fig. 2.5 Time-of-flight spectrometer used for measuring electron energies and ion mass-to-charge ratios.

uncertainties of a factor of two. Although this method of measuring laser intensity has a rather large uncertainty associated with it, it places a lower limit on the intensity of the laser.

#### II.D. Uncertainties in Intensity

In addition to the methods described above, uncertainties in the relative laser intensity were further measured by comparing ionization data taken on different days or at different gas pressures. Over the course of four months the data showed a relative intensity fluctuation of 25% or less. Further checks on the relative intensity measurements between gases were done by shooting mixed-gas targets, thus ensuring that intensity calibrations were the same for all gases.

There is a 25% error in relative intensity measurements, but there are also possibilities of absolute or systematic errors in the intensity due to uncertainties in energy, and absolute temporal and spatial shapes. The distinction between relative and absolute uncertainties is important. Relative uncertainties determine how our data compares with itself and absolute uncertainties determine how we compare our data to theoretical predictions or to experiments done by other groups. Absolute uncertainties come from errors in each of the three critical measurements: laser energy, focal spot size, and pulse length. The pyroelectric calorimeter can measure the laser energy with less than 10% uncertainty, but uncertainties in the laser energy can come from a number of sources such as poorly known transmission of the vacuum window and focusing lens. Additionally, neutral density filters must be placed in front of the calorimeter when the full laser energy is fired. These filters may partially saturate at high laser power causing their transmission efficiencies to vary from their calibrated values. The energy which is measured by the energy monitor may not all be focused or may not all be in the compressed pulse (see Fig. 2.4 autocorrelator trace). The amount of energy which was uncompressed in the experiments described in chapter three was approximately 70% of the total energy and was 10% in the experiments which are described in chapter five. The focusing lens has a hole drilled in the center of it to avoid damage from high power laser beams, consequently some of the laser energy is not focused. We have measured the amount of energy which is focused by placing a 300  $\mu\text{m}$  pinhole at the focal plane and we find that approximately 75% of the energy is transmitted through the pinhole.

The focal spot size measurement has several uncertainties associated with it. The imaging system is actually a set of two lenses with a total thickness of approximately 5 cm. The location of the principal plane of the two lens system was

difficult to determine to better than 0.2 cm, and the position of the laser focus was difficult to determine to better than 0.5 cm. These two uncertainties made it difficult to determine the magnification of the imaging system with better than a 10% uncertainty. This leads to about a 20% uncertainty in an area measurement. Additional errors are introduced by uncertainties associated with digitization of the film and conversion of the optical density of the film into laser intensity. These errors increase the uncertainty in the focal spot measurement to about 50%.

The experiments in chapter three had a rather large fluctuation in pulse width. The relative fluctuation could be measured by the method described above (Eqn. 2.5), but the absolute width of each pulse was difficult to determine since an absolute measurement was only taken before and after each data run. Of course these absolute measurements also had a fluctuation associated with them which caused some difficulty in assigning the correct pulse width to the average pulse width during the data run. This absolute uncertainty was about 30%. When all uncertainties are accounted for, the absolute uncertainty in the intensity measurement is approximately a factor of two. The stability of the laser pulse width has since been improved and the resulting uncertainty in the temporal width is approximately 10% for the experiments described in chapter five.

Each of the three measurements has good precision which results in a total relative uncertainty of 25%, but the accuracy is not as good, which makes the total absolute uncertainty a factor of two.

## II.E. Ion Spectrometer: Data Acquisition

The interaction of a high-intensity laser beam with atoms results in ionization of some or all of the atoms at the focus of the beam. The number of ions produced depends on the rate of ionization, the duration of the laser pulse, and the number of atoms initially in the focal region. There are a number of techniques to measure laser pulse lengths [see section II.B]. Also the number of atoms initially at the focus can be calculated by measuring the number density (or pressure) of the gas sample, and measuring the focal area of the laser beam and deducing the focal volume (actually the focal volume can be measured as described earlier). Consequently, it is possible to measure the rate of ionization. Of course the matter is somewhat complicated by a depletion of the neutral atoms at the focus. Fortunately it is possible to include these depletion effects in theoretical calculations by solving coupled rate equations which conserve the total number of atoms plus ions. The task of measuring the ionization rate then becomes equivalent to the task of measuring the number of ions created in the focal volume of the laser. If multiply charged ions are created, it is also necessary to know which charge states are present and how many ions of each charge state have been produced. The experimental set-up described below is designed to measure the number of ions with a given mass-to-charge ratio.

The ion spectrometer is enclosed in a high-vacuum chamber to insure the purity of our target gases (see Fig. 2.6). The targets used for these experiments are the five lightest noble gases (He, Ne, Ar, Kr, and Xe). The chamber is pumped down to a pressure of  $\sim 1 \times 10^{-8}$  Torr ( $3 \times 10^8$  cm<sup>-3</sup>) using a liquid nitrogen trapped diffusion pump. At times we found it helpful to use a titanium sublimation pump in conjunction with the diffusion pump. This combination gave us background pressures in the mid- to

low-  $10^{-9}$  Torr range. A low background pressure is necessary to ensure that the ion spectra are not cluttered with peaks due to impurity gases in the chamber.

It is not possible to eliminate all impurity signals. The main contribution is water which originally comes from humidity in the air. After baking the chamber and keeping it under vacuum for several months water is still present in the system. Additional contaminants come from diffusion pump oil or anything which has not been cleaned properly. This accounts for the presence of carbon in the spectra.

After an acceptable background pressure is achieved the target gas is introduced into the chamber with a precision leak valve. The target pressures range from  $5 \times 10^{-8}$  Torr to  $3 \times 10^{-5}$  Torr. Our detector has a dynamic range of more than  $10^3$  so this variation in the gas density increases the dynamic range of our ion number measurement to more than six orders of magnitude.

A time-of-flight spectrometer is used to separate the ions according to their mass-to-charge ratios. The spectrometer is the same as for the electron energy measurement which is depicted in Fig. 2.5. To collect ion spectra it is operated as follows. A uniform electric field is placed across the laser focal volume (nominally 800 V/cm). This field sweeps the ions into a field-free drift tube which is made of 2 inch copper pipe. The ends of the tube are covered with a wire grid to prevent leakage of the field into the drift region. Inside the tube the ions drift with a constant velocity until they reach the other end of the tube where they are accelerated into the detector. The velocity with which the ions drift depends on the mass-to-charge ratio of the given ion. Since the length of the drift tube is known, ( $\sim 30$  cm for the experiments described in chapter three and  $\sim 60$  cm for those in chapter five) the ion velocity can be determined from the time of flight.

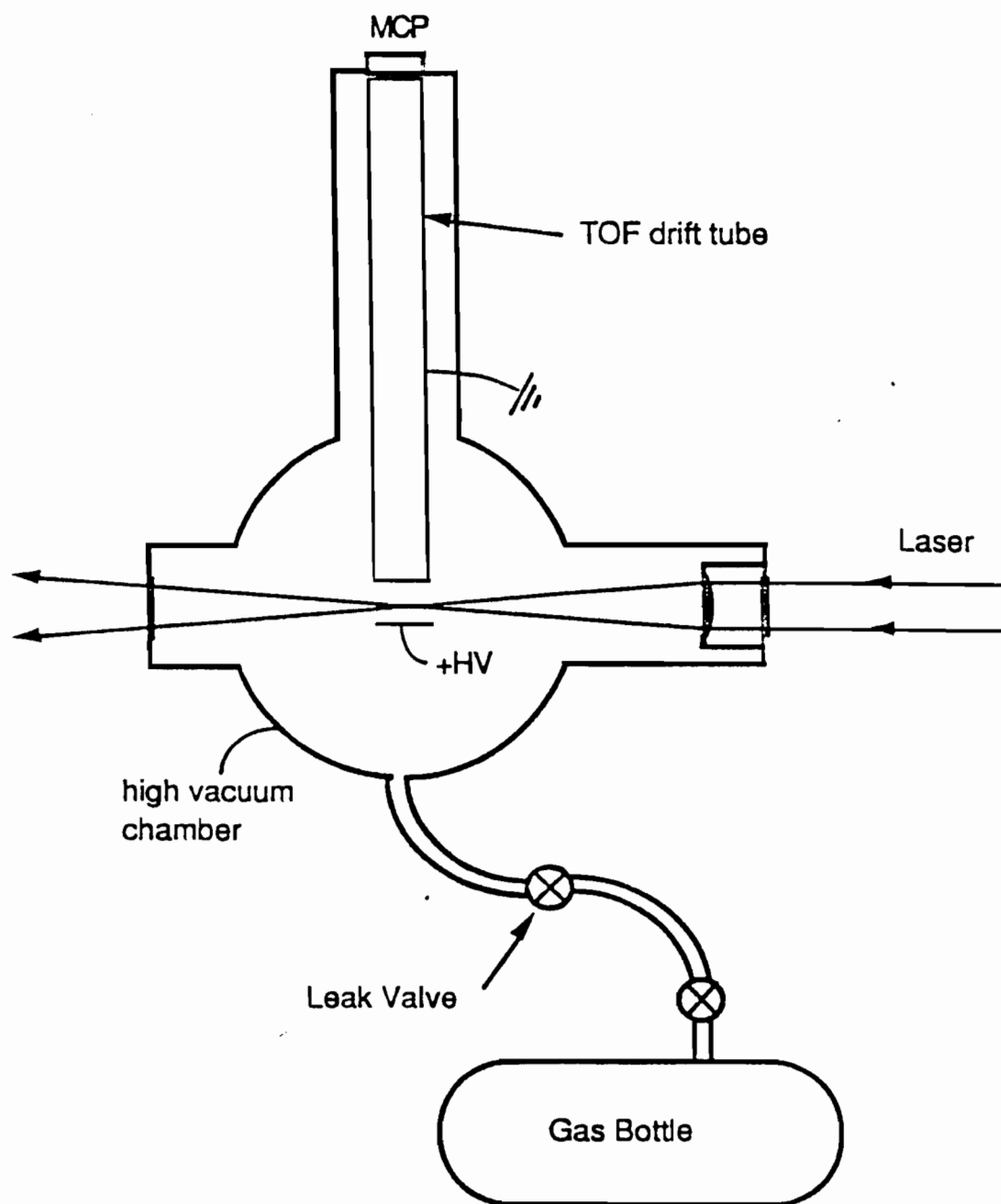
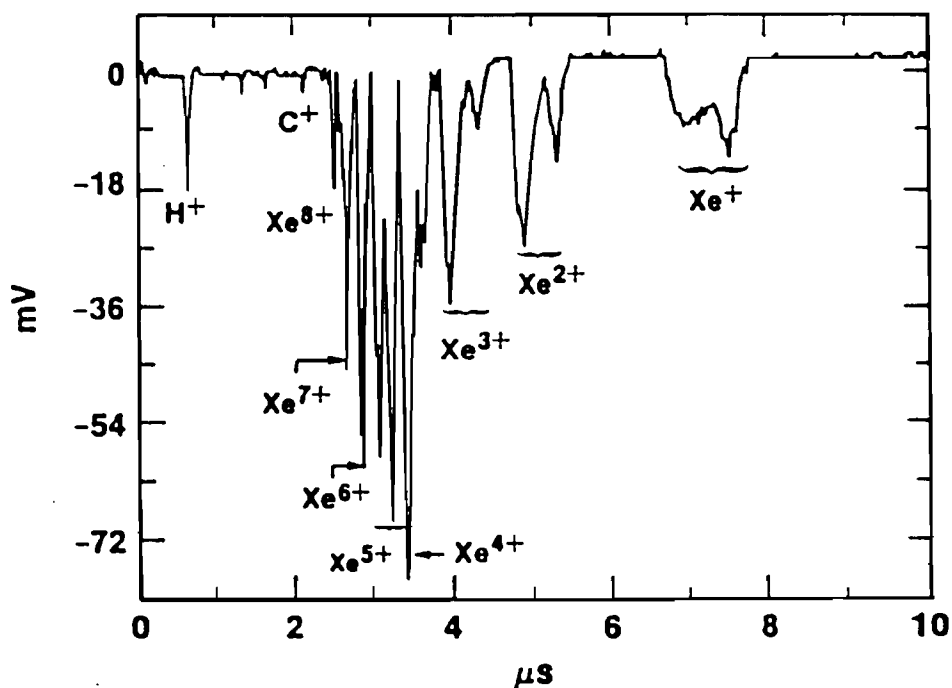


Fig. 2.6 Vacuum tank, TOF spectrometer, and gas delivery system.

A detailed derivation of the total time which it takes the ions to travel from the laser focus to the detector is given in appendix B, however it is sufficient to know that the time of flight is proportional to the square root of the mass-to-charge ratio.

$$t_T = t_H \times \sqrt{\frac{m}{q}} \quad (2.7)$$

where  $t_H$  is the time-of-flight of a hydrogen ion. The ion time of flight for the various gases in the chamber typically ranges from about 1  $\mu\text{s}$  to 15  $\mu\text{s}$  depending on the ionic species and on the strength of the extraction field. A typical TOF spectrum is shown in Fig. 2.7.



E5511

Fig. 2.7 Time-of-flight spectrum of xenon. The detector is saturated when the first charge state arrives (at about 7  $\mu\text{s}$ ).

The ions are detected with a dual microchannel plate (MCP) which has a total signal gain of approximately  $10^6$ . The spectra are recorded with a temporal digitizer which is interfaced to a PC computer. For the experiments described in chapter three we used a Hewlett-Packard digitizing scope (HP54201A) which has 6 bits of vertical resolution thereby limiting our dynamic range. The laser energy and second harmonic energy were recorded with paper and pencil and entered into the computer after the data run had been finished. For the experiments in chapter five we changed to a CAMAC (Computer Automated Measurement And Control) based system for the data acquisition. The waveform digitizer is an 8-bit Kinetic Systems CAMAC module 4030 operated at 100 MHz which is interfaced to a PC computer with a LeCroy 6010 GPIB CAMAC crate controller. Laser energy and second harmonic energy are measured with large area photodiodes and the signals are digitized with an 11-bit charge integrator (LeCroy 2249W).

## **II.F. Ion Spectrometer: Data Analysis**

After the spectra are stored, the individual ion peaks are integrated to determine the number of ions detected in each charge state. The MCP is capable of measuring single-ion events so several spectra were found which contained single-ion peaks. These peaks were integrated to find how many volt-seconds corresponded to one ion. This made it possible to find the number of ions which were in the larger peaks. This number calibration is useful only for a specific gas fill pressure, a specific laser focal volume, and a specific spectrometer efficiency. The data must be scaled accordingly for changes in any of these.

The number of ions is then plotted versus the peak laser intensity. The collection efficiency of the spectrometer and the quantum efficiency of the MCP have

not been fully calibrated so the data presented here represent the number of ions detected, not the number of ions produced. No correction has been made for the relative detection efficiency since the manufacturer's efficiency calibration indicates no significant difference among the various charge states (see Fig. 2.8).<sup>74</sup> The combined optical transmission of the three wire grids was about 5% for the experiments in chapter three. This coupled with the MCP quantum efficiency gives a total efficiency of about 2-3%. The experiments in chapter five used wire grids with a combined optical transmission of about 50% which yields a total efficiency of about 25-35%. These efficiencies have not been included in the ion graphs since we are not sure that the optical transmission is a good approximation of the ion transmission. The overall efficiency predicted using the optical transmission of the grids is consistent with the values which are suggested by theoretical curves shown in chapter four.

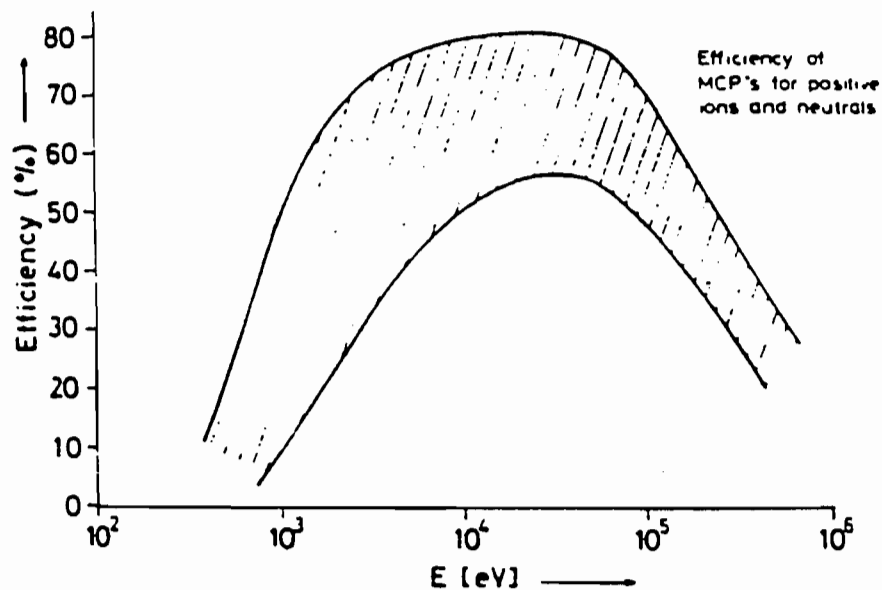


Fig. 2.8 Quantum efficiency of an MCP detector versus ion energy. Our ion energies range from 3 keV for singly charged particles to 27 keV for nine times ionized particles. [from reference 74]

The recovery time of each channel in the MCP detector is long relative to the time of flight of even the heaviest ions, thus each channel can only detect one ion per laser shot. Consequently, it is possible for the detector to saturate before the entire spectrum has been captured (see Fig. 2.7). By the time the third charge state arrives, the detector has already begun to saturate. This is evidenced by the flattening of the ion peaks. If the gas pressure in the chamber is decreased and the laser intensity is kept constant, the lower charge states become more sharply peaked. Since the ionization process is not a function of pressure (unless the pressure is high enough for collisional ionization to take place) the shape of the peaks should not change. Due to this saturation effect the data in chapter three covers only about three orders of magnitude in ion number. The technique of variable backfill pressures was used for the experiments in chapter five to compensate for this saturation problem. The effects of detector saturation can be clearly seen in figure 2.9 which shows a logarithmic graph of the

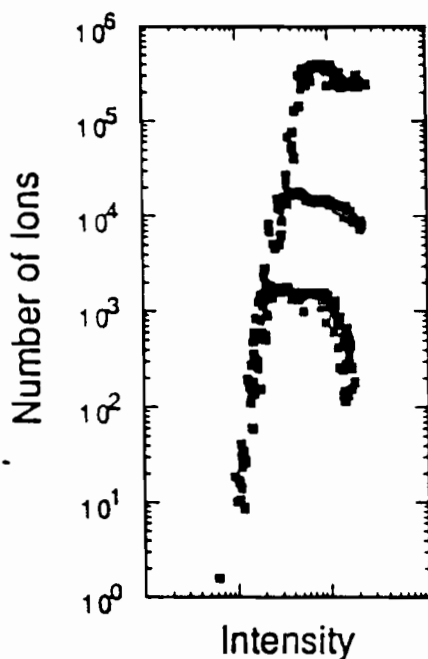


Fig. 2.9 Log-log plot of the production of  $\text{Xe}^+$  ions versus laser intensity using three different gas densities. Saturation of the detector is clearly seen for each of the three different backfill pressures.

number of  $Xe^+$  ions versus peak laser intensity. The graph contains data taken at three different fill pressures with the data from each pressure scaled to account for the different gas densities. The saturation of the MCP can be seen for the three different cases yet the data in the unsaturated portion of the curves line up for all three pressures. The agreement between different fill pressures is an indication of the relative uncertainty in the laser intensity. Subsequent graphs of ion number versus intensity will have the saturated portions of the data removed so that more than one charge state can be shown on each graph without loss of clarity.

## CHAPTER THREE

### ION EXPERIMENTS

#### III.A. The Data

Figures 3.1-3.5 show logarithmic plots of the number of ions created versus peak laser intensity for helium, neon, argon, krypton, and xenon. These data represent the first systematic experimental survey of the ionization of five noble gases in this intensity regime, exceeding the intensities of previous survey experiments by over an order of magnitude. The laser was operated in single-pass compression with an  $f/5$  focusing lens. These data were taken at a single fill pressure which limits the dynamic range along the vertical scale. The data shown in these graphs has been passed through a three-point digital smoothing filter. Further smoothing is not practical due to the small number of data points.

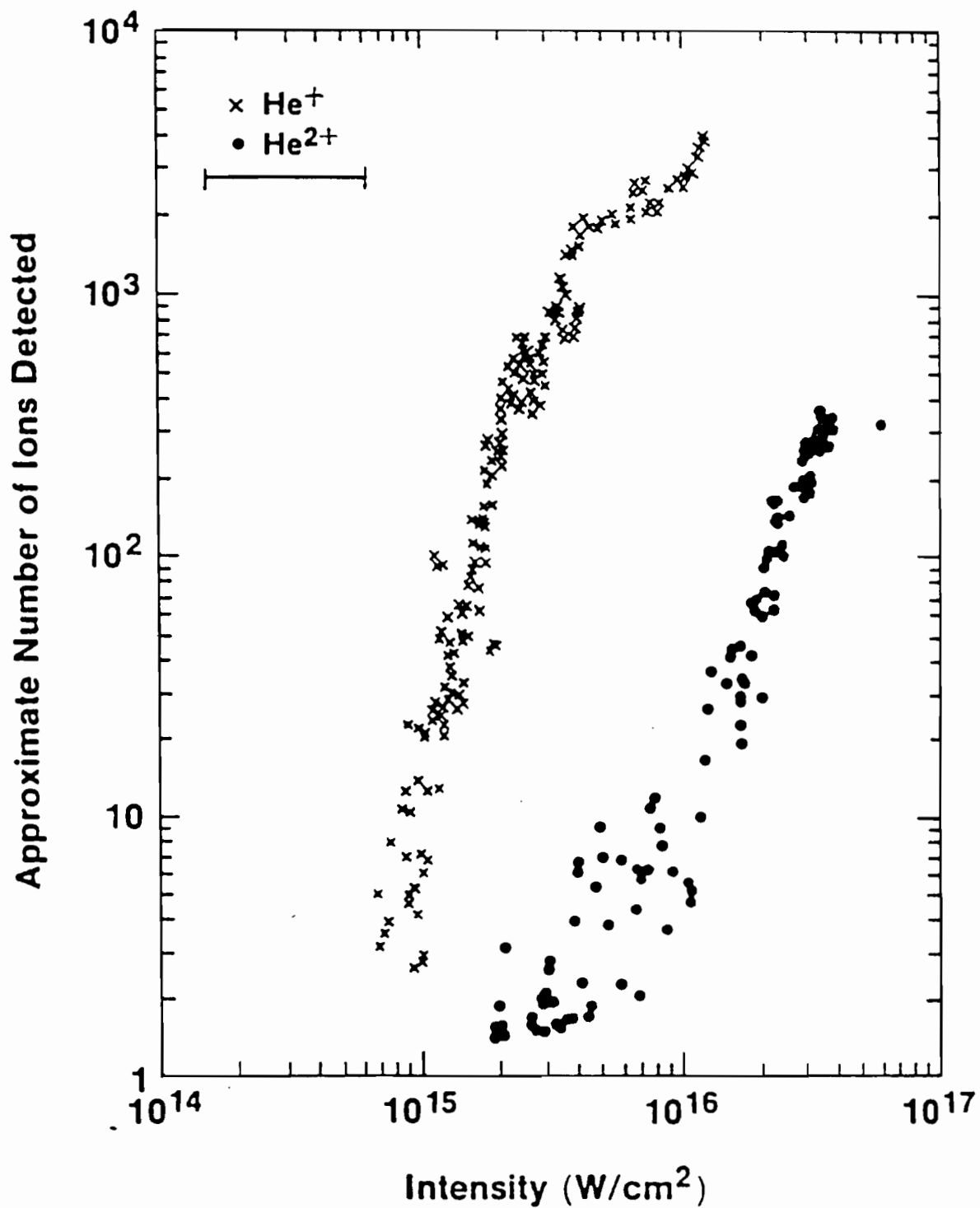


Fig. 3.1 Helium ion production rate as a function of peak laser intensity. The relative intensity error can be deduced from the scatter of the data points and the error bar represents the absolute intensity error. ( $P = 5 \times 10^{-6}$  Torr)

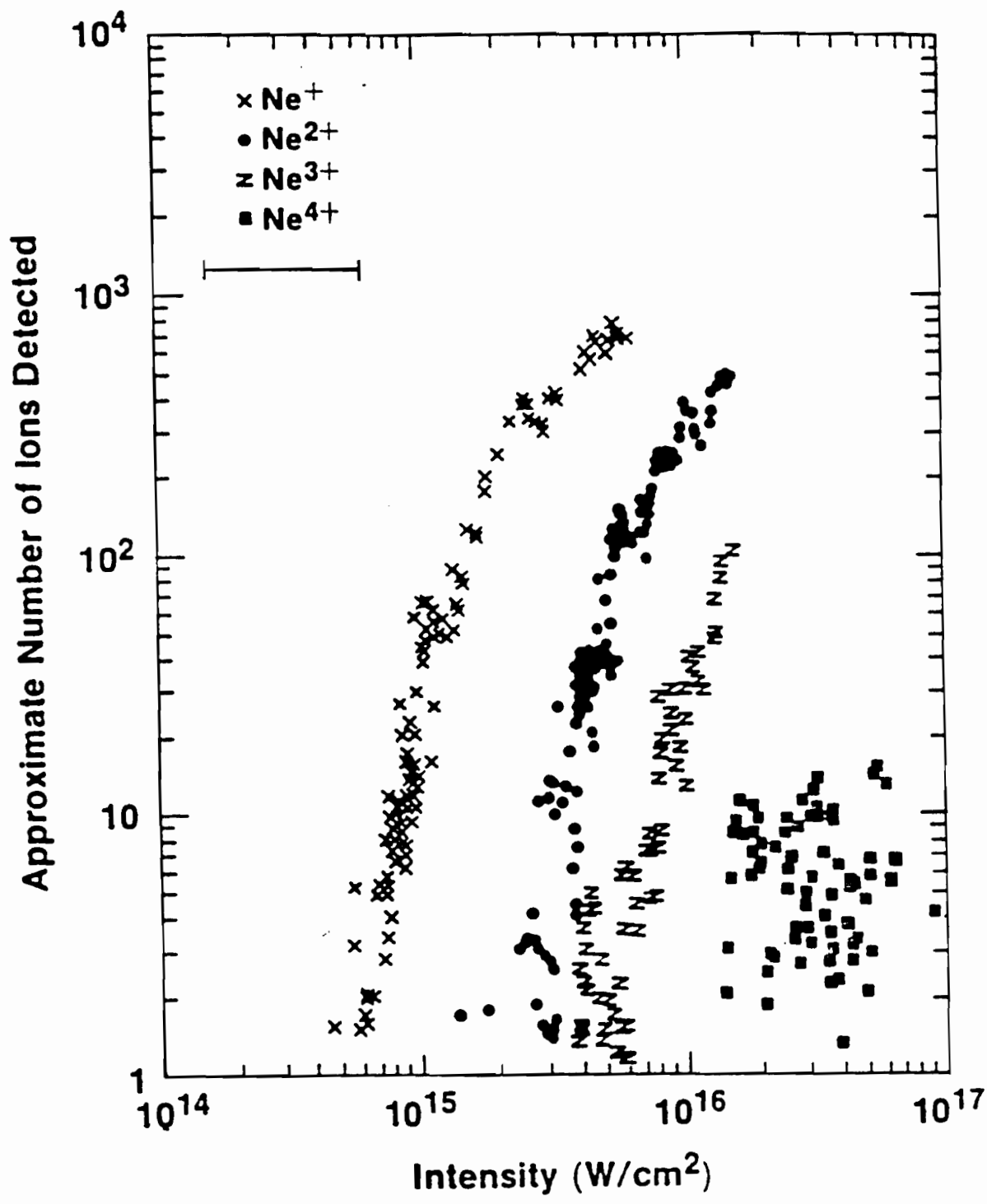


Fig. 3.2 Neon ion production rate as a function of peak laser intensity. The relative intensity error can be deduced from the scatter of the data points and the error bar represents the absolute intensity error. ( $P = 2.5 \times 10^{-6}$  Torr)

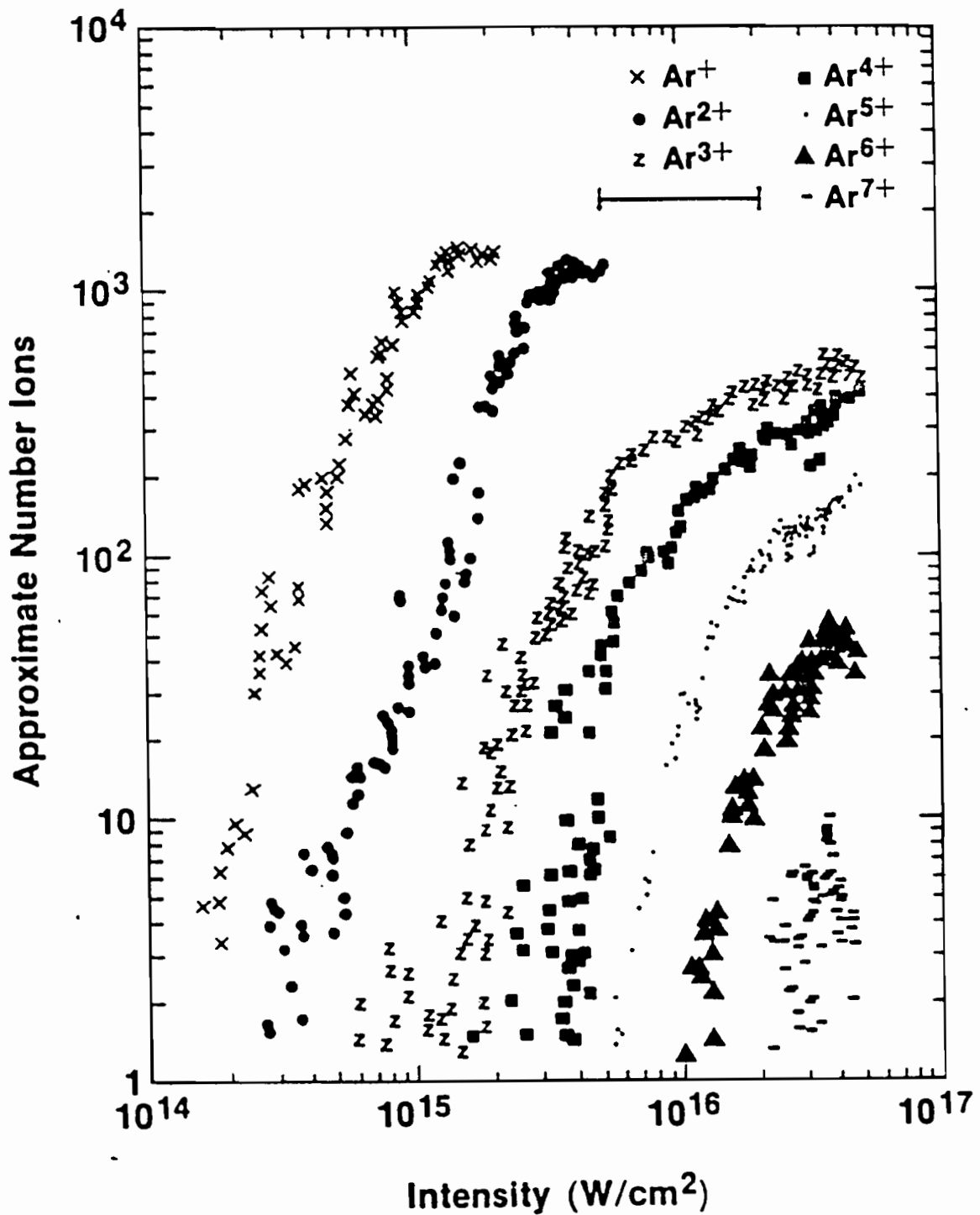


Fig. 3.3 Argon ion production rate as a function of peak laser intensity. The relative intensity error can be deduced from the scatter of the data points and the error bar represents the absolute intensity error. ( $P = 5 \times 10^{-6}$  Torr)

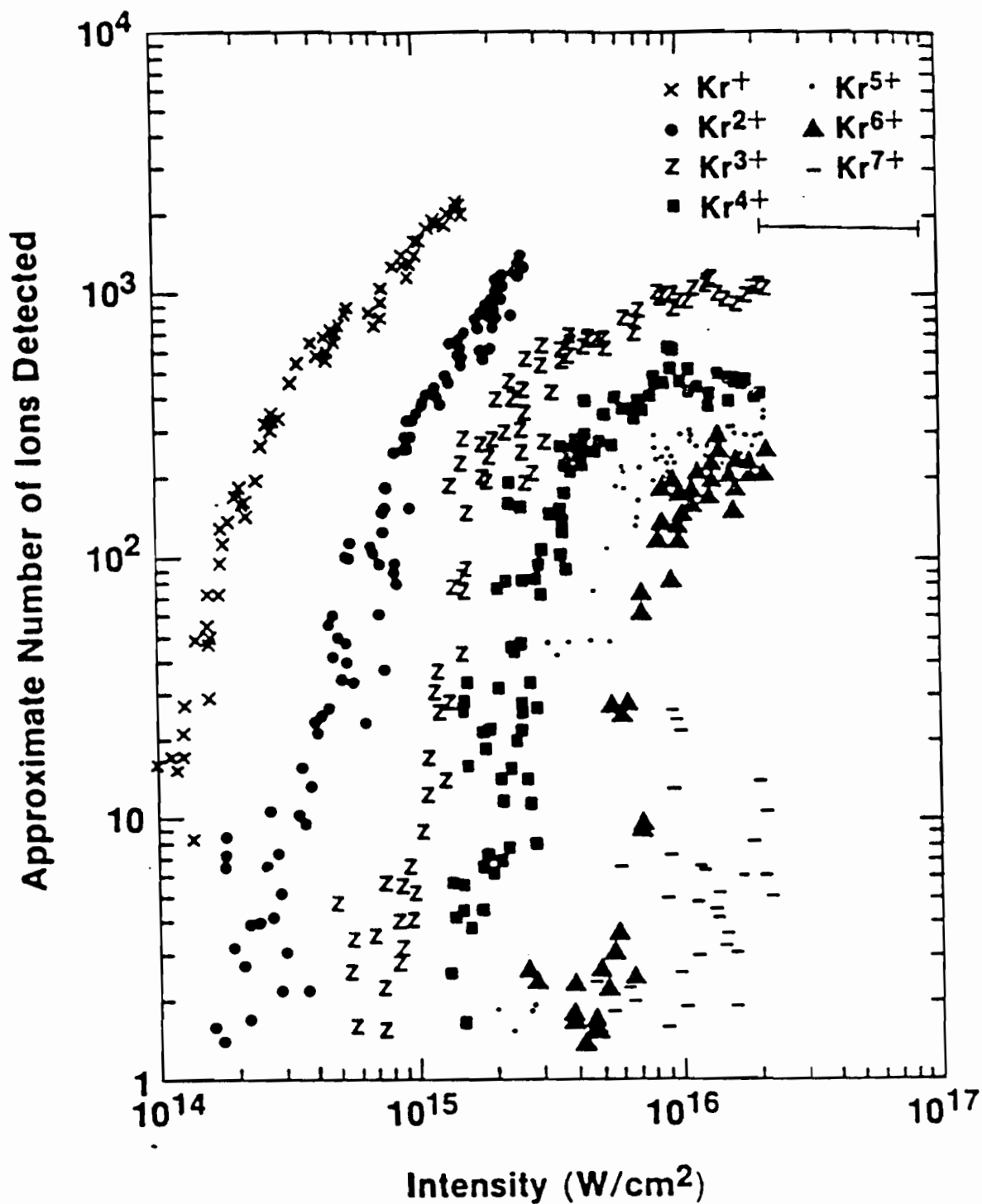


Fig. 3.4 Krypton ion production rate as a function of peak laser intensity. The relative intensity error can be deduced from the scatter of the data points and the error bar represents the absolute intensity error. ( $P = 5 \times 10^{-6}$  Torr)

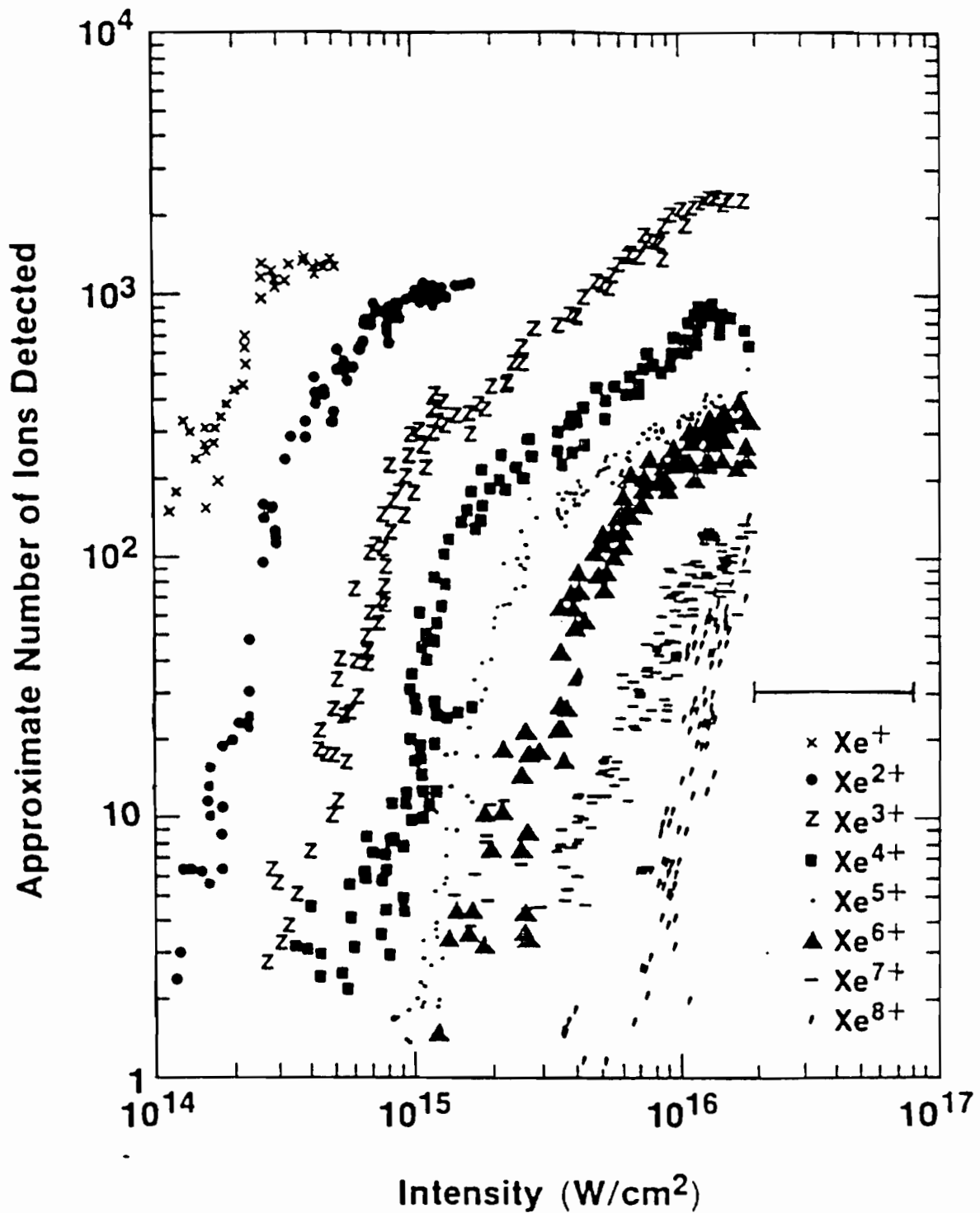
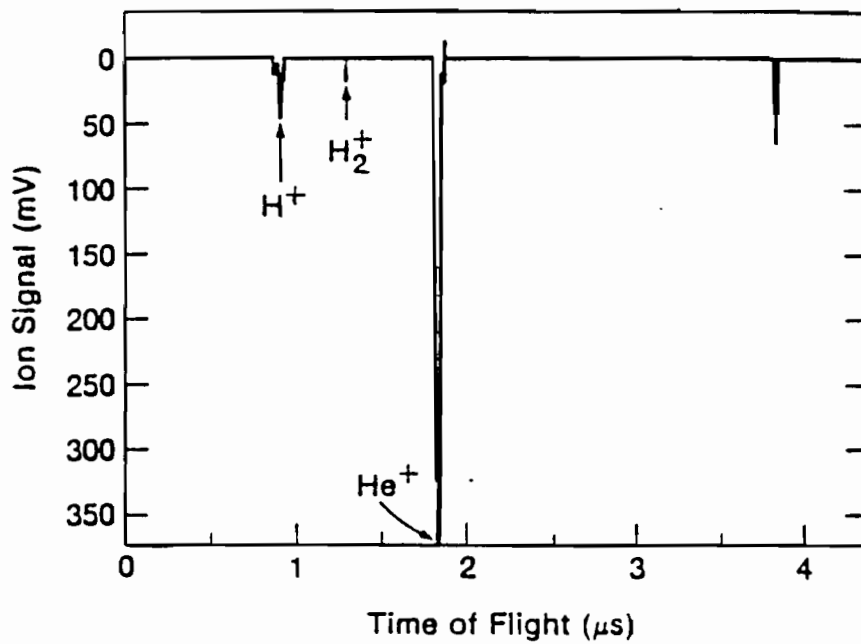


Fig. 3.5 Xenon ion production rate as a function of peak laser intensity. The relative intensity error can be deduced from the scatter of the data points and the error bar represents the absolute intensity error. ( $P = 5 \times 10^{-6}$  Torr)

The time-of-flight spectrometer separates ions according to their mass-to-charge ratios. For certain charge states this can cause an overlap between the noble gas which is under study and a background contaminant. The most obvious case of this is the overlap between  $\text{He}^{2+}$  and  $\text{H}_2^+$  which both have a mass-to-charge ratio of 2. The data shown in Fig. 3.1 shows a noise level of about 10 or 15 ions where we see a mixture of both  $\text{He}^{2+}$  and  $\text{H}_2^+$ . We are certain that above this level the signal is due primarily to  $\text{He}^{2+}$ . This determination was made by observing the ratio of the peak heights of  $\text{H}^+$  and  $\text{H}_2^+$  as a function of laser intensity. In data runs for the other four noble gases this ratio did not change significantly as a function of intensity, but for a helium target the peak located at a mass-to-charge ratio of 2 became much larger than the  $\text{H}^+$  peak when the laser intensity was increased (see Fig. 3.6). This increase in relative height could only be due to the creation of  $\text{He}^{2+}$ . In the future this experiment should be repeated using the helium isotope  $^3\text{He}$ .



Z492

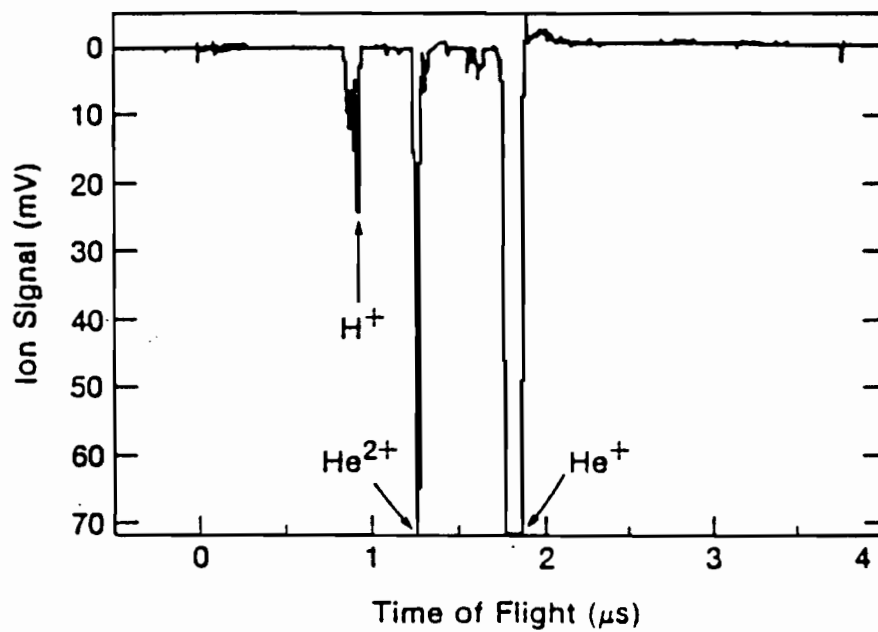


Fig. 3.6 Helium TOF spectrum at (a) low intensity and (b) high intensity.

$\text{He}^{2+}$  is present in (b) but not in (a).

Figures 3.1 to 3.5 provide an easy way to determine a detection threshold for ionization. We define the "threshold intensity" as the intensity required to detect 10 ions of a given charge state. This level is well above the detector noise level in most cases and also well below the focal volume saturation level by a factor of about 100. Since the ion curves are quite steep for low ion number, a detection level of either 1 or 100 ions would have caused the value of the absolute threshold intensity to change by less than a factor of 1.8 (recall that the absolute uncertainty in intensity is a factor of 2). Any threshold level which is at or below the saturation level would work equally well if it is applied to all the data in a consistent manner. The objective in defining a threshold intensity is to provide a means of comparing the ionization of various gas species. A change in threshold level would change the absolute intensity values but would have little effect on the relative threshold intensities.

Best-fit lines have been calculated for the lower portion of each charge state to determine the intensity where each curve crosses the 10 ion level. There is a statistical fluctuation of the data about these lines which causes about a 25% relative uncertainty in the threshold intensities. These threshold intensities are plotted versus the ionization potential of each ion in Fig. 3.7. Some higher charge states which were not previously shown<sup>17</sup> have been added to this graph. The heavier noble gases are easier to ionize than the lighter ones for a given ionization potential which suggests that a dependence on  $Z$  as well as on the ionization potential is required in theoretical models. This trend is described quite well by the BSI model which predicts a threshold intensity scaling of  $I_{th} \propto E^4/Z^2$ . The BSI model is discussed in chapter four.

It is possible to determine values of the Keldysh gamma parameter<sup>19</sup> (recall Eqns. 1.6, 1.7) at the threshold intensities. Recall that  $\gamma \ll 1$  suggests that a tunneling

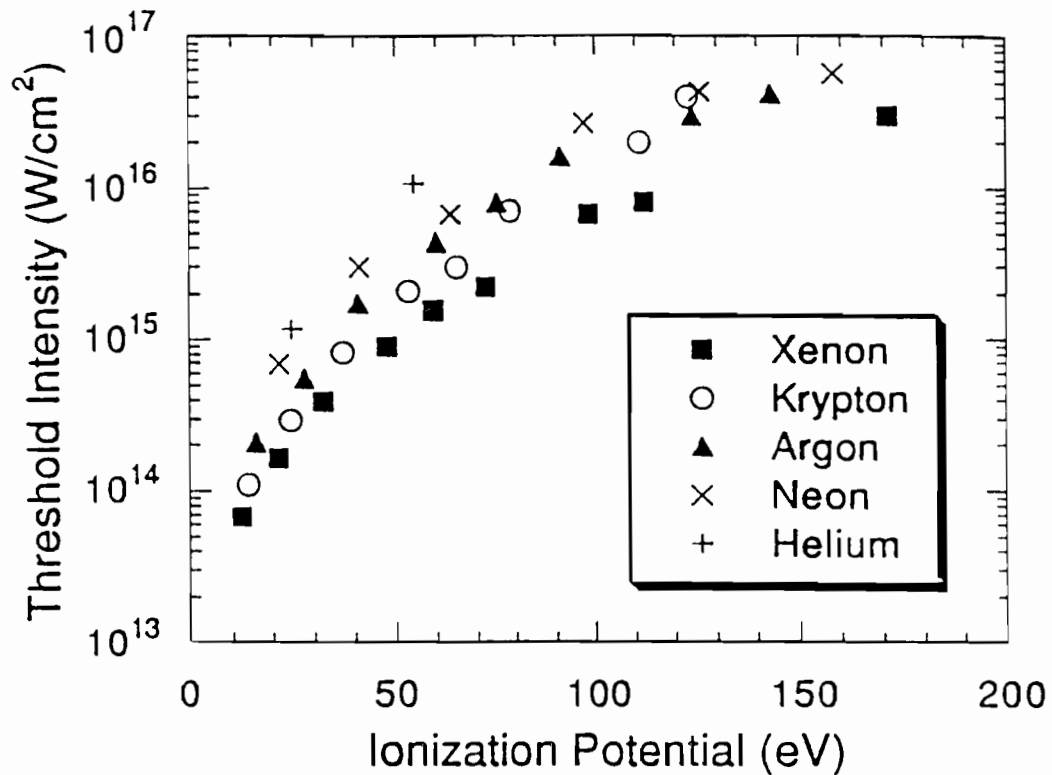


Fig. 3.7 Ion threshold intensity vs. sequential ionization potential for five noble gases. There is a clear species dependence present. The relative error in the laser intensity is approximately the size of the data symbols.

ionization approach should be valid and  $\gamma \gg 1$  suggests multiphoton ideas will work better. Figure 3.8 shows that at the threshold intensities the  $\gamma$  parameter has a value less than 1 in all cases. A lower threshold level would cause the values of  $\gamma$  to increase slightly causing some of the lower charge states to move to  $\gamma > 1$ , however most of the ion curves would remain in the  $\gamma < 1$  regime.

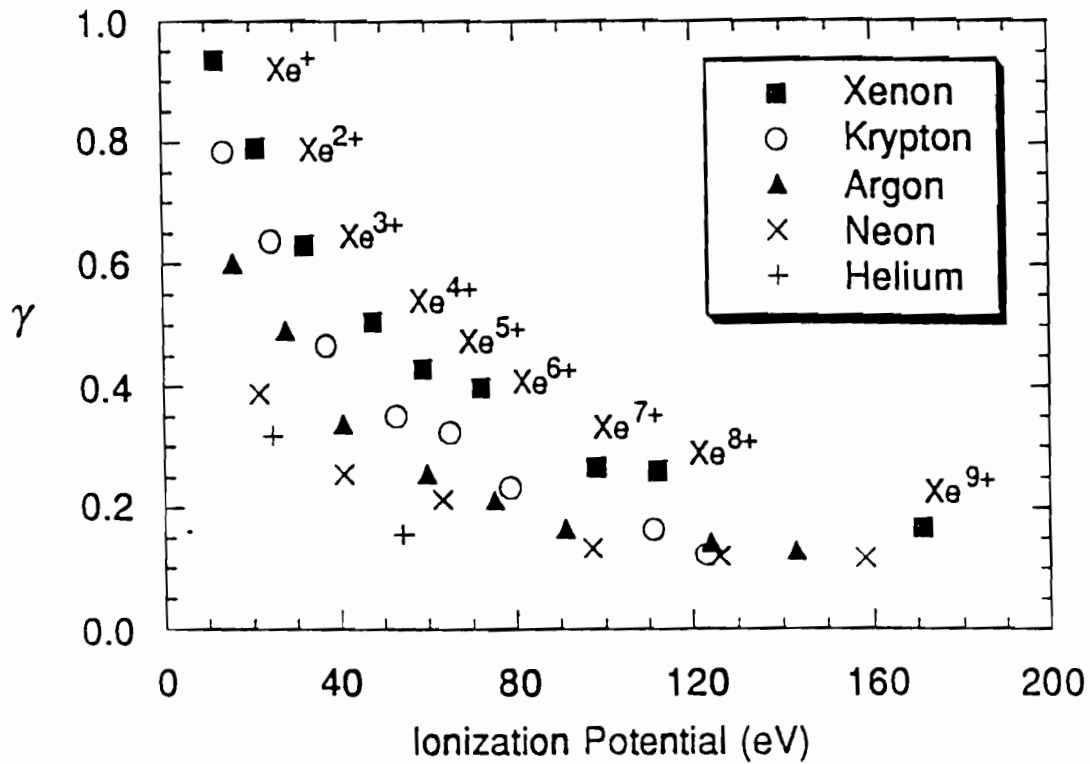


Fig. 3.8 Keldysh's  $\gamma$  parameter at the threshold intensity for each of the charge states. In each case  $\gamma < 1$  which indicates that ionization occurs in the tunneling regime.

### III.B. Comparison to Other Experiments

A comparison of threshold intensities which have been measured under a wide variety of conditions is made in Figs. 3.9-3.13. Various groups have used different criteria for determining the threshold intensities so, where it was possible, I have applied our threshold criterion to their ion production curves rather than use the values which were given by the authors. The threshold level which has been used here is 0.01 of the saturation level. This has been done for all references except Boreham,<sup>48</sup> Baldwin,<sup>49</sup> Gibson,<sup>58</sup> and Corkum<sup>73</sup> who only gave the values of the threshold

intensities so in these cases I have used the values which were given by the authors. Boreham and Baldwin did not measure ions so the threshold intensities must be inferred from the electron spectra. This makes it impossible to know exactly what the equivalent ion threshold level is. Gibson used a threshold level of 0.001 so the threshold levels would be slightly higher using the 0.01 criterion (by less than a factor of 2).

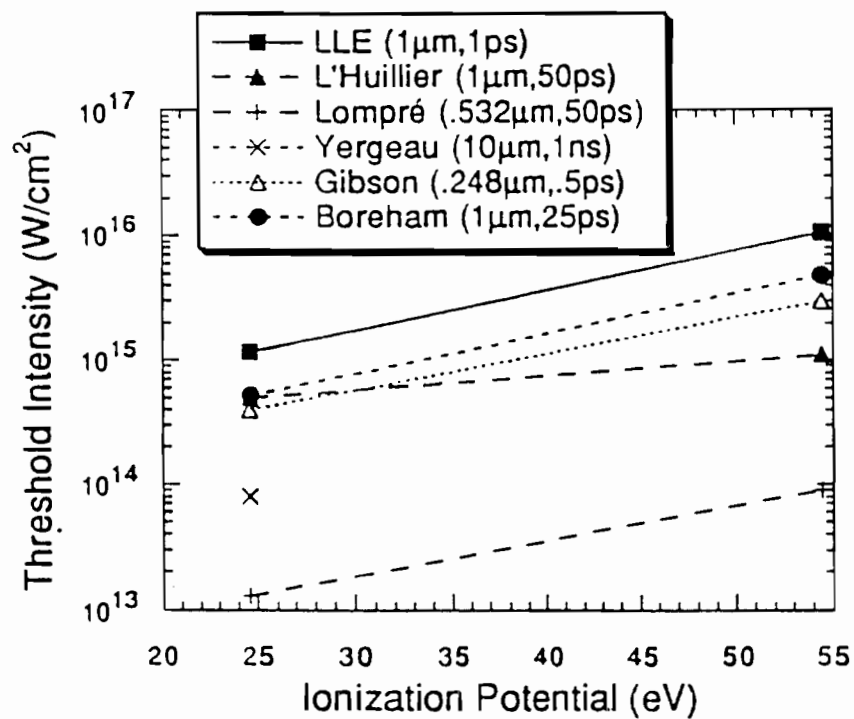


Fig. 3.9 Helium ion threshold intensities versus sequential ionization potential for various experimental groups. References are: L'Huillier,<sup>14</sup> Lompré,<sup>31</sup> Yergeau,<sup>50</sup> Gibson,<sup>58</sup> and Boreham.<sup>48</sup>

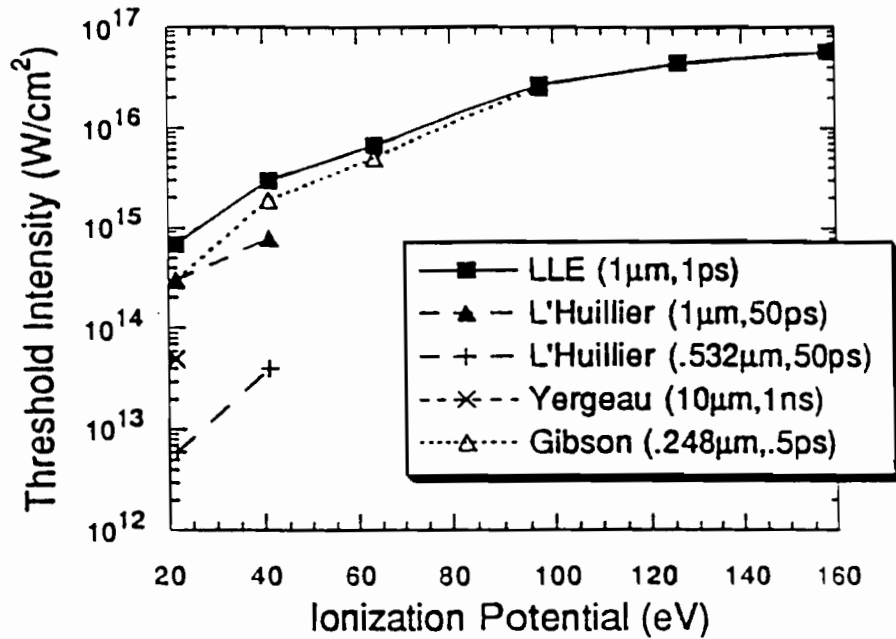


Fig. 3.10 Neon ion threshold intensities versus sequential ionization potential for various experimental groups. References are: L'Huillier,<sup>14,15</sup> Yergeau,<sup>50</sup> and Gibson.<sup>58</sup>

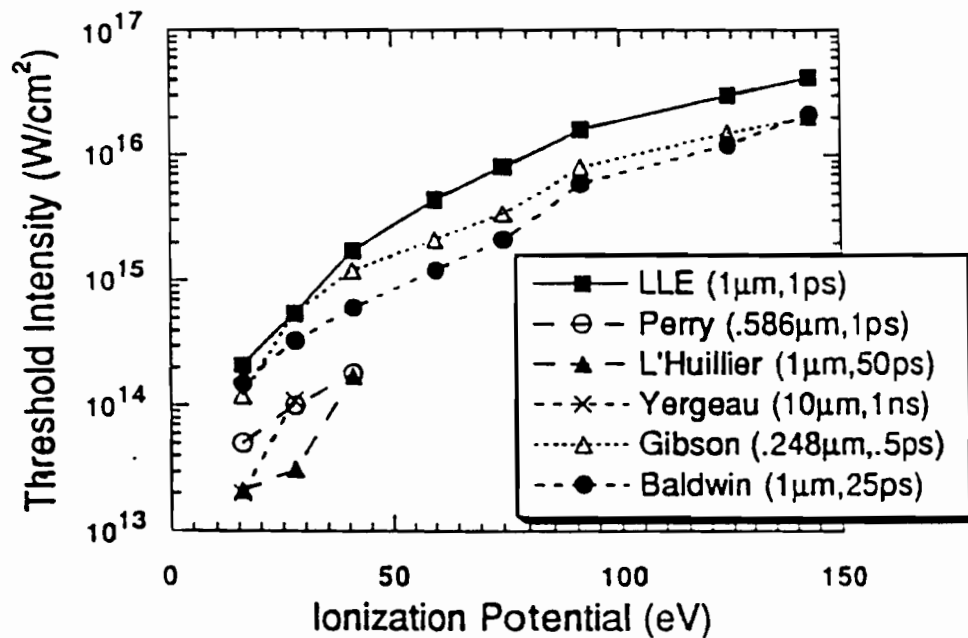


Fig. 3.11 Argon ion threshold intensities versus sequential ionization potential for various experimental groups. References are: Perry,<sup>36</sup> L'Huillier,<sup>14</sup> Yergeau,<sup>50</sup> Gibson,<sup>58</sup> and Baldwin.<sup>49</sup>

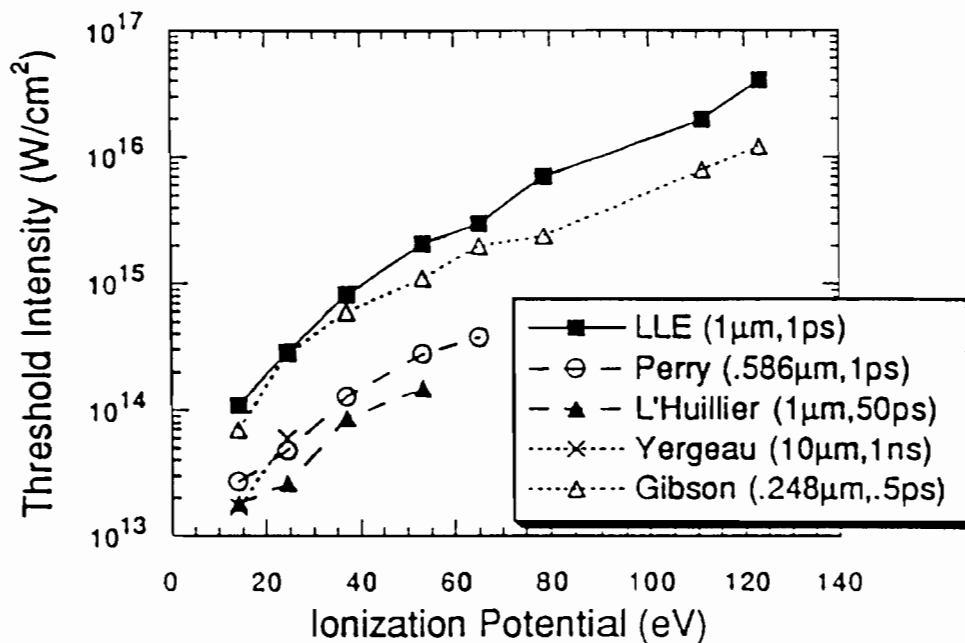


Fig. 3.12 Krypton ion threshold intensities versus sequential ionization potential for various experimental groups. References are: Perry,<sup>36</sup> L'Huillier,<sup>14</sup> Yergeau,<sup>50</sup> Gibson.<sup>58</sup>

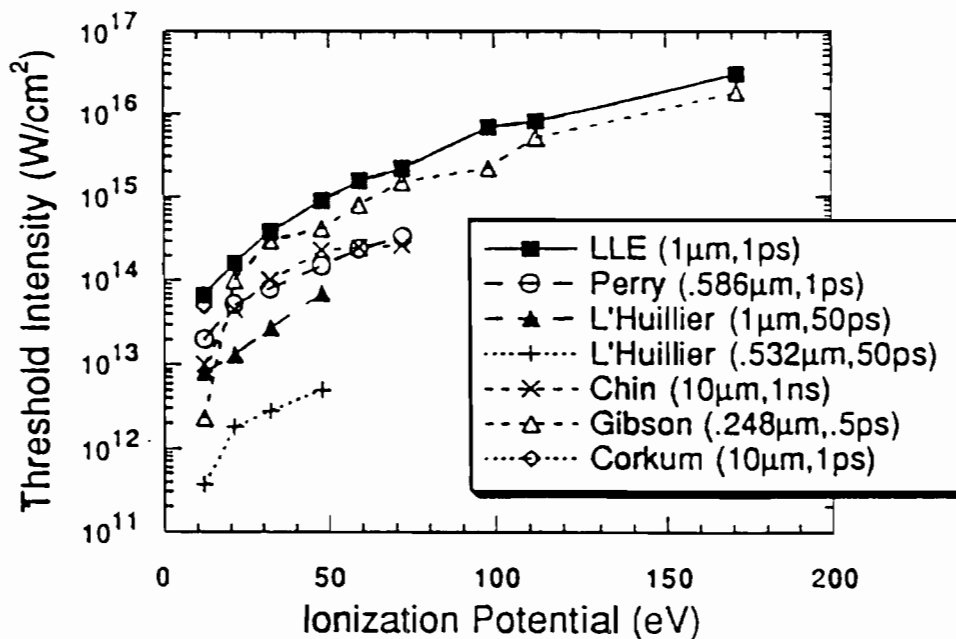


Fig. 3.13 Xenon ion threshold intensities versus sequential ionization potential for various experimental groups. References are: Perry,<sup>36</sup> L'Huillier,<sup>14,15</sup> Chin,<sup>50,51</sup> Gibson,<sup>58</sup> and Corkum.<sup>73</sup>

Some general features of these graphs are that the threshold intensity increases with increasing wavelengths or decreasing pulse length. The pulse length dependence at  $1 \mu\text{m}$  can be seen in the comparison of the LLE data, Boreham's and Baldwin's data, and L'Huillier's  $1 \mu\text{m}$  data. Another comparison which shows the importance of pulse length is between Corkum's 1 ps and Chin's 1 ns results at  $10 \mu\text{m}$ . The 1 ps results have a much higher threshold and are in agreement with our 1 ps results at a much shorter wavelength ( $1 \mu\text{m}$ ). For an  $I^N$  process the threshold intensity is expected to scale with pulse length as  $T^{1/N}$  so a change in pulse length by a factor of 50 should change the threshold intensity by  $50^{1/N}$ . For  $N = 11$  the shift in threshold intensity is expected to be 1.4.

Some differences in the data can be attributed to the use of different experimental techniques used by the various groups so it is interesting to note that the shorter wavelength data of L'Huillier and Lompré have much lower threshold intensities than the longer wavelength data. These two sets of results were performed at the same laboratory with nearly identical data acquisition and analysis procedures which eliminates most of the errors associated with determining the absolute threshold intensity measurements.

The values for  $\gamma$  which we have observed are not in agreement with L'Huillier's results. They observed values of  $1 < \gamma < 3$  for xenon, krypton, and argon and  $\gamma < 1$  for neon and helium. Thus it is not surprising that they have observed an  $I^N$  dependence on their ionization curves and we have observed an  $I^q$  dependence where  $q \sim 6$  for all gases.

The short pulse experiments done by Gibson agree with tunneling models even though the experiments were performed in a regime of  $1 < \gamma < 8$ . This suggests that the pulse length as well as Keldysh's  $\gamma$  parameter should be considered in determining whether a "tunneling" or perturbative approach should be taken.

## CHAPTER FOUR

### COMPARISON BETWEEN EXPERIMENTS AND THEORIES

#### IV.A. Procedure for Comparison

This chapter compares various theoretical predictions with the experimental results. Threshold intensities alone cannot determine the validity of a given model so in this chapter the entire ion spectrum will be compared to the data in order to understand better the validity of each model. It is not possible to determine ionization rates directly from the experimental data so a comparison of theory and data requires that the temporal and spatial dependence of the laser intensity be folded into the theoretical calculations. Ion production curves can then be generated and compared to the data, allowing the associated ionization rates to be determined.

The theoretical ion production curves are obtained by integrating coupled rate equations for the number of ions in each charge state [see appendix C].

$$\frac{dN_i}{dt} = N_{i-1}W_{i-1} - N_iW_i \quad (4.1)$$

where  $W_i$  is the ionization rate of charge state  $i$ , and the initial conditions are  $N_0 = \text{initial gas density}$  and  $N_i = 0$  for  $i > 1$ . There are some basic assumptions implicit in Eqn. (4.1): 1) sequential ionization is assumed to be the only pathway for ionization (recall the discussion in chapter one regarding sequential versus direct ionization), 2) a slowly-varying envelope approximation is used which means that we assume the laser pulse turn-on and turn-off can be treated adiabatically. The sequential ionization assumption should be valid since our data show no evidence of a direct ionization process. The adiabatic approximation should be valid since our pulses

contain about 500 optical cycles and the intensity does not change significantly during a cycle. Here a significant change in intensity is defined by the change in the ionization rate. If we assume an ionization rate dependence of  $I^6$  (which is what is suggested by our data and is contrary to the LOPT prediction of  $I^{11}$ ) we can calculate the relative change in ionization rate per laser cycle. This relative change is shown in Fig. 4.1 for a Gaussian pulse shape. A Lorentzian pulse shape of equal width would yield approximately the same changes in the rate since the maximum slope on a Lorentzian is only slightly less than that of a Gaussian.

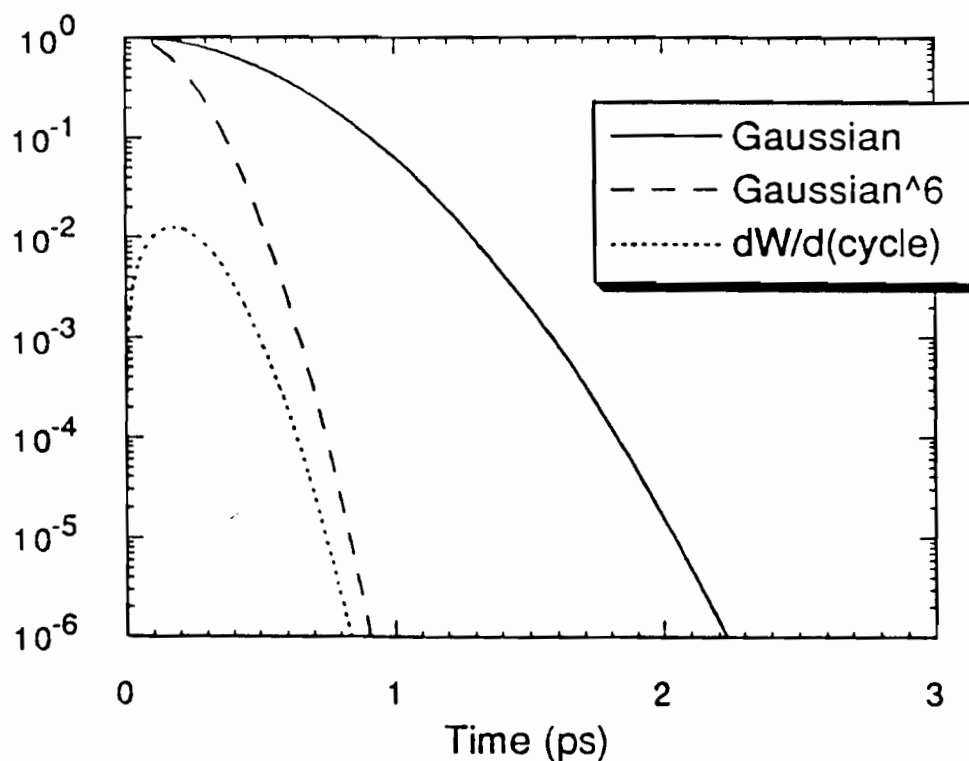


Fig. 4.1 The change in ionization rate per laser cycle never exceeds  $10^{-2}$  of the ionization rate. An  $I^6$  rate is assumed since this is suggested by our data. A Gaussian intensity profile and an  $I^6$  profile are also shown.

The spatial and temporal dependence of the intensity, and consequently of the ionization rates, is accounted for in the calculation. The integration is performed by finding the volume of each iso-intensity shell and then propagating a laser pulse through that volume. The ion velocities are slow so we can assume no ion motion between the shells during a 1 ps pulse. This means that the total number of particles in each shell is conserved which accounts for focal volume saturation effects. The intensity distribution is modeled as temporally Lorentzian (1 ps FWHM) and spatially Gaussian<sup>62</sup> ( $w_o = 12 \mu\text{m}$  in chapter four and  $w_o = 19 \mu\text{m}$  in chapter 5). The experiments in chapter five used a Gaussian pulse (1.9 ps FWHM) but most of the ionization occurs near the peak of the pulse so the results are insensitive to the exact temporal profile and a Gaussian pulse yields nearly identical results. The volume of an iso-intensity shell is (derivation in appendix D):

$$Volume = \pi z_R w_o^2 \left[ \frac{4(c_1 - c_2)}{3} + \frac{2(c_1^3 - c_2^3)}{9} - \frac{4}{3}(\tan^{-1}(c_1) - \tan^{-1}(c_2)) \right], \quad (4.2)$$

where  $w_o$  is the  $1/e^2$  radius of the intensity profile,  $z_R = \pi w_o^2 / \lambda =$  the Rayleigh range of the focus and  $c_j = [(I_o - I_j) / I_j]^{1/2}$  with  $I_o$  being the peak laser intensity and  $I_j$  the intensity within shell  $j$ . The calculation ignores collisional ionization. The amount of collisional ionization depends on the gas pressure. Since the gas fills the entire tank, the gas pressure at the MCP detector is the same as at the focus of the laser and the gain of the MCP makes the electron densities several orders of magnitude higher than at the focus. Collisional ionization inside the MCP channels can create a very noisy signal, but noise due to collisional ionization of gas is not present in the MCP signal at pressures below  $\sim 2 \times 10^{-5}$  Torr which suggests that no significant collisional ionization is present at the laser focus either.

Collisional ionization rates at the laser focus can also be calculated. The ion temperature at the focus is significantly less than the electron temperature so ionization due to ion-ion collisions is negligible compared to that due to electron-ion collisions. The collisional ionization rate of the  $i^{\text{th}}$  charge state can be approximated by<sup>75</sup>

$$W_i = \left[ \frac{10^{-5} n_e (T_e / E_i)^{1/2}}{E_i^{3/2} (6.0 + T_e / E_i)} \right] \exp\left(\frac{-E_i}{T_e}\right) \quad (4.3)$$

where  $n_e$  is the electron density ( $\sim 10^{12} \text{ cm}^{-3} = 3 \times 10^{-5} \text{ Torr}$  for 100% singly ionized particles),  $T_e$  is the electron temperature in eV, and  $E_i$  is the ionization potential of the  $i^{\text{th}}$  charge state in eV. An estimate of the electron temperature can be obtained from the electron energy measurements described in chapter two ( $T_e \sim 130 \text{ eV}$  when  $I = 3 \times 10^{15} \text{ W/cm}^2$ ). We want an upper bound on the collisional ionization rate so we want to use the ionization potential of the first charge state ( $E_1 \sim 15 \text{ eV}$ ). This yields an ionization rate of  $3 \times 10^4 \text{ s}^{-1}$  which is negligible compared to the non-collisional ionization rates which are larger than  $10^{10} \text{ s}^{-1}$ . The electron density would have to be much higher before we would have to consider collisional ionization processes in the theoretical calculations.

The agreement between the theoretical and experimental spacing between charge states is important to know since this is a way of checking the functional dependence of the theory. If the spacing of a particular model is correct but the curves are uniformly shifted in one direction or the other we can guess that the functional dependence is good and that the ionization rate that is predicted by the model is off by some multiplicative factor. On the other hand if no shift is required for the first charge state but the spacing is wrong, we know that the functional dependence of the theory is incorrect for higher

charge states, which makes the model less useful when making predictions of what will happen as the laser intensity is increased.

All the theoretical curves shown have been shifted along the vertical scale to account for the fact that our detection efficiency is less than 100%. The overall efficiency of the spectrometer has been estimated as 2-3% (see section II.F). A comparison between two sets of theoretical curves (the models in sections (IV.B) and (IV.C)) and the experimental ion production curves suggests an efficiency of approximately 1%–5% which is consistent with the estimates made in chapter two. The comparison with theory suggests that the overall efficiency of the spectrometer decreases as the atomic mass increases. This is probably due to a momentum dependent quantum efficiency of the MCP (rather than an energy dependence as shown in Fig. 2.8).

In the following sections we will compare the ion production curves of various theoretical models to our data. The two criteria we use to determine the applicability of a particular model are the agreement between 1) the absolute magnitudes of the theoretical and experimental intensities, and 2) the spacing among different charge states. The theoretical models under consideration are briefly described in decreasing order of agreement based on these two criteria. The model which are described are: a barrier suppression model, a species dependent tunneling model, three versions of Keldysh's model, and a classical Thomas-Fermi model.

Atomic units will be used in the following sections where  $m = \hbar = e = 1$ . Conversions to more familiar units can be made by using the following values:  $\omega_A = 4.134 \times 10^{16} \text{ s}^{-1}$ ,  $\mathcal{E}_A = 5.142 \times 10^9 \text{ V/cm}$ ,  $I_A = 3.509 \times 10^{16} \text{ W/cm}^2$ , and  $E_A = 27.212 \text{ eV}$ .

#### IV.B. Barrier Suppression Ionization (BSI) Theory

This theory is based on a simple one-dimensional model for ionization, and begins with the superposition of the Coulomb potential and a quasi-static laser field where the quasi-static condition is satisfied when the laser frequency  $\omega_L$  is much less than the electron orbital frequency. The resulting total potential at peak field strength is written as:

$$V(x) = -\frac{Z}{|x|} \pm \mathcal{E}x . \quad (4.4)$$

This potential (which is graphed in Fig. 1.1b) has a relative maximum located at  $x_{max}$  which can easily be found by setting  $[\partial V(x)/\partial x]_{x=x_{max}} = 0$  and solving for  $x_{max}$ . Equating  $V(x_{max})$  to the ionization potential ( $E$ ) of the atom or ion permits us to find the critical electric field which is necessary to allow the bound electron to escape without tunneling. This critical electric field for the  $i^{th}$  charge state is:

$$\mathcal{E}_{crit}^{(i)} = \frac{E_i^2}{4Z_i} . \quad (4.5)$$

When the peak electric field of the laser equals this critical field strength, the atomic electron can freely escape and the corresponding laser intensity can be called the threshold intensity

$$I_{th}^{(i)} = \frac{E_i^4}{16Z_i^2} ,$$

$$I_{th}^{(i)} [W / cm^2] = 4.00 \times 10^9 \frac{E_i^4 [eV]}{Z_i^2} . \quad (4.6)$$

In a purely Coulombic field, the ionization potential is uniquely dependent on the ionic charge  $Z$  and the principal quantum number  $n$ :  $E = Z^2/(2n^2)$ . However, for

the complex atoms used in our experiments, electron shielding occurs and its effects can be accounted for by using values of  $E$  which have been determined independently, either experimentally or by use of more sophisticated atomic structure calculations. Alternatively, we could think of the principal quantum number  $n$  being replaced by the effective principal quantum number  $n^*$ , where  $n^*$  is simply the principal quantum number after it has been corrected for the quantum defect ( $\delta_l$ ):<sup>76</sup>

$$n_i^* = n - \delta_l^{(i)} = \frac{Z_i}{\sqrt{2E_i}}, \quad (4.7)$$

where  $Z$  is the charge of the ion created, and  $E$  is the atomic or ionic ionization potential of the initial state. Threshold intensities calculated using Eqn. 4.6 are compared to the experimentally determined threshold intensities (see Fig 4.2). In all cases the theory and experiment agree within the absolute uncertainty of the laser intensity.

The choice of experimental threshold levels was chosen somewhat arbitrarily at 10 ions. A change in threshold level to 1 or 100 ions results in a shift of the threshold intensities by a factor of about 1.8 or less as described in Sec. (III.A). This shift is less than the absolute intensity uncertainty which is a factor of two. For example, if a level of 1 ion had been chosen for the threshold, all the data points in Fig. 4.2 would be shifted to the left by a factor of approximately 1.8, but most of the data would still be within an experimental uncertainty of the line of exact agreement. The important point here is not that the absolute intensities of the data and experiment agree, but that the data shows an  $E^4/Z^2$  dependence for the threshold intensities. It should be noted that Gibson<sup>58</sup> has also observed this  $E^4/Z^2$  species dependence using a much shorter wavelength (248 nm).

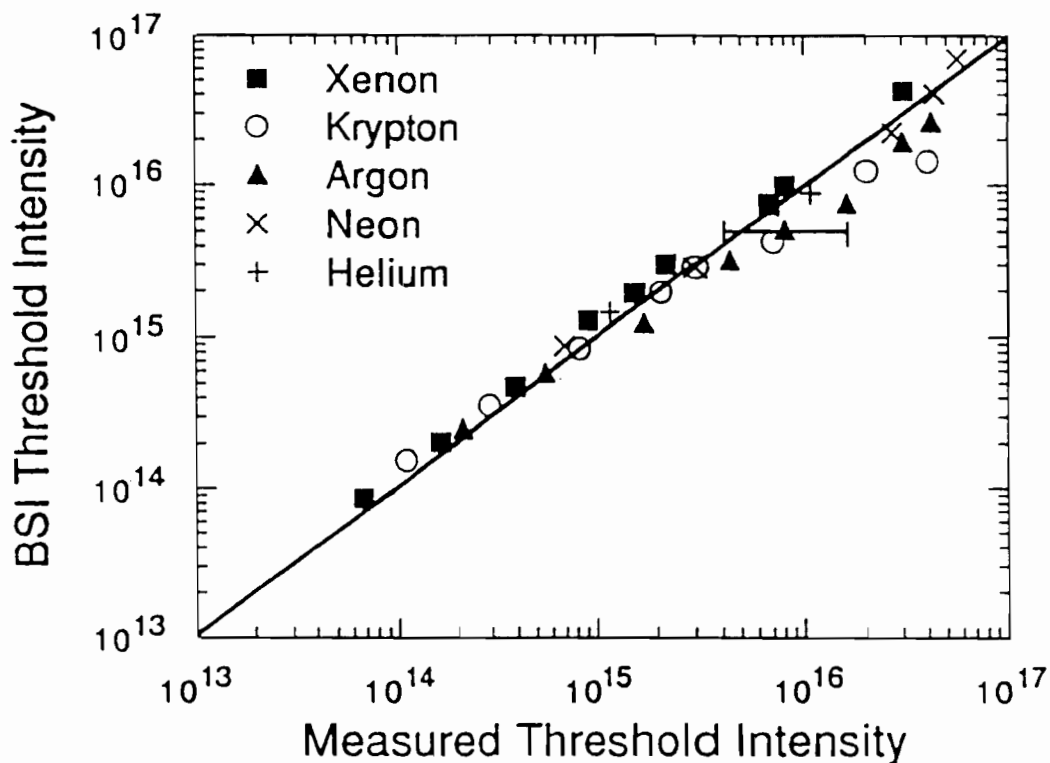


Fig. 4.2 Comparison of experimentally determined and theoretically predicted threshold intensities using the BSI model. The solid line corresponds to exact agreement. Some of the higher charge states shown on this graph are not included on the ion curves since the production of these charge states occurred on only a few laser shots.

The BSI model can be used to predict the laser intensities which would be required to see the next higher charge states than was observed. These values are given in Table 4.1.

<u>Ion</u>	<u>Intensity (W/cm<sup>2</sup>)</u>
Xe <sup>10+</sup>	6.7×10 <sup>16</sup>
Kr <sup>9+</sup>	1.4×10 <sup>17</sup>
Ar <sup>9+</sup>	1.6×10 <sup>18</sup>
Ne <sup>7+</sup>	1.5×10 <sup>17</sup>

Table 4.1 BSI Threshold intensities for the next higher charge state than was observed. The intensities exceed those which were used in the experiment so it is reasonable that we did not see these charge states.

The entire ion production curves are calculated for BSI theory by integrating over the laser pulse and assuming an ionization probability of unity for  $I \geq I_{th}$  and zero for  $I < I_{th}$ . The resulting BSI theory curves are shown in Figs. 4.3-4.7 with a shift in the vertical scale which accounts for spectrometer efficiency. These zero-parameter fits show satisfactory agreement with the ionization data.

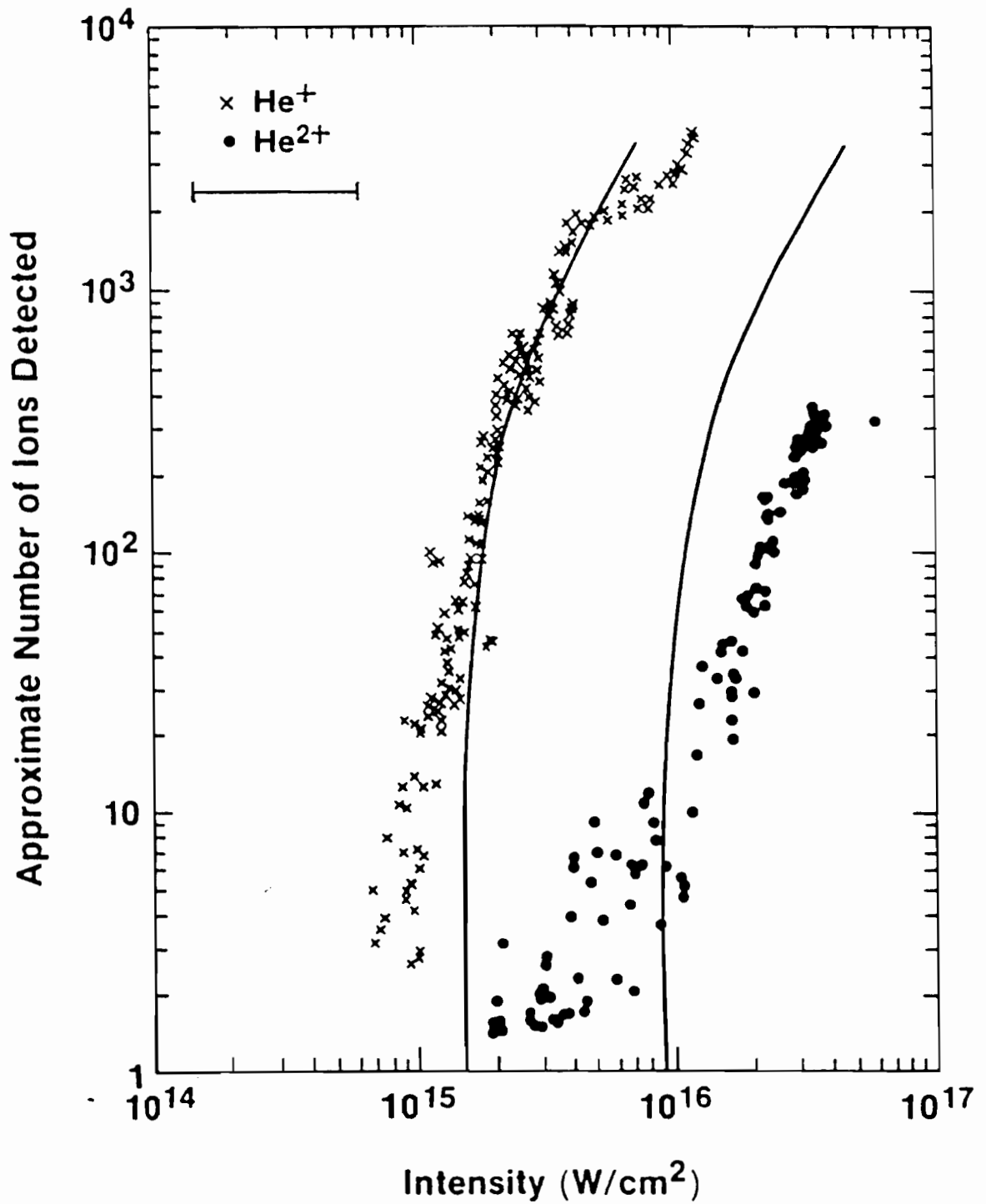


Fig. 4.3 Comparison of helium ion data with theoretical curves calculated using the BSI model. The absolute intensity uncertainty is indicated.

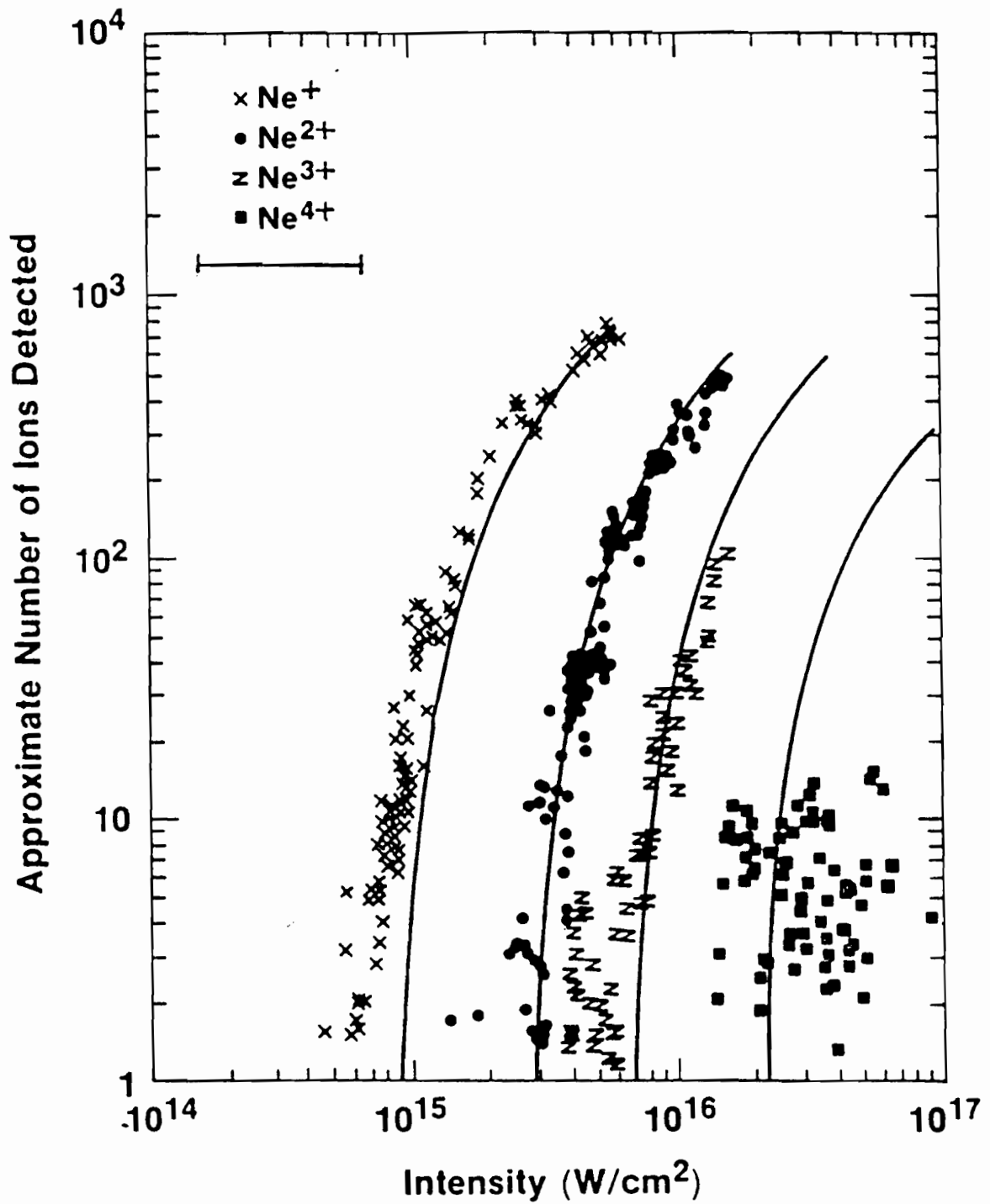


Fig. 4.4 Comparison of neon ion data with theoretical curves calculated using the BSI model. The absolute intensity uncertainty is indicated.

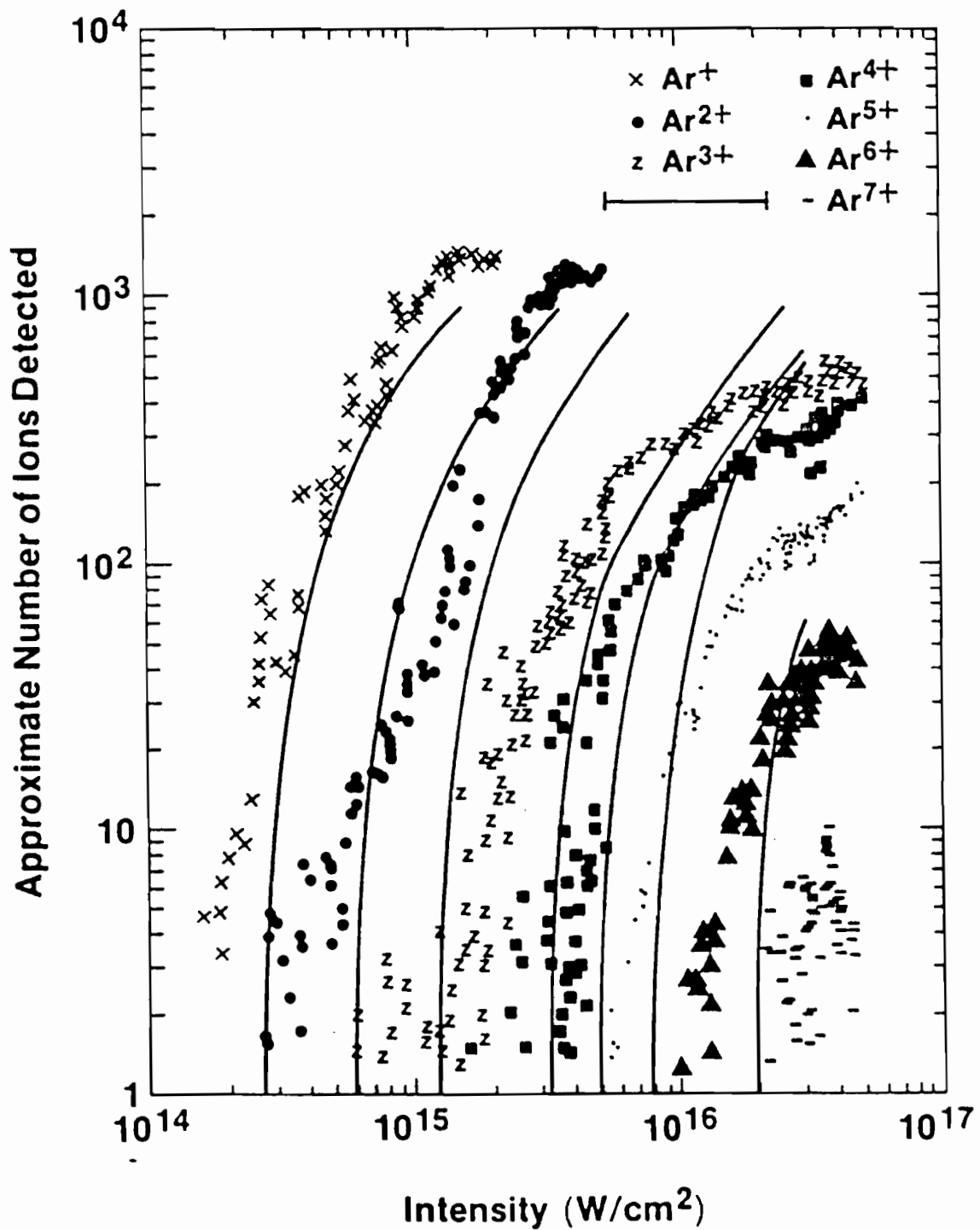


Fig. 4.5 Comparison of argon ion data with theoretical curves calculated using the BSI model. The absolute intensity uncertainty is indicated.

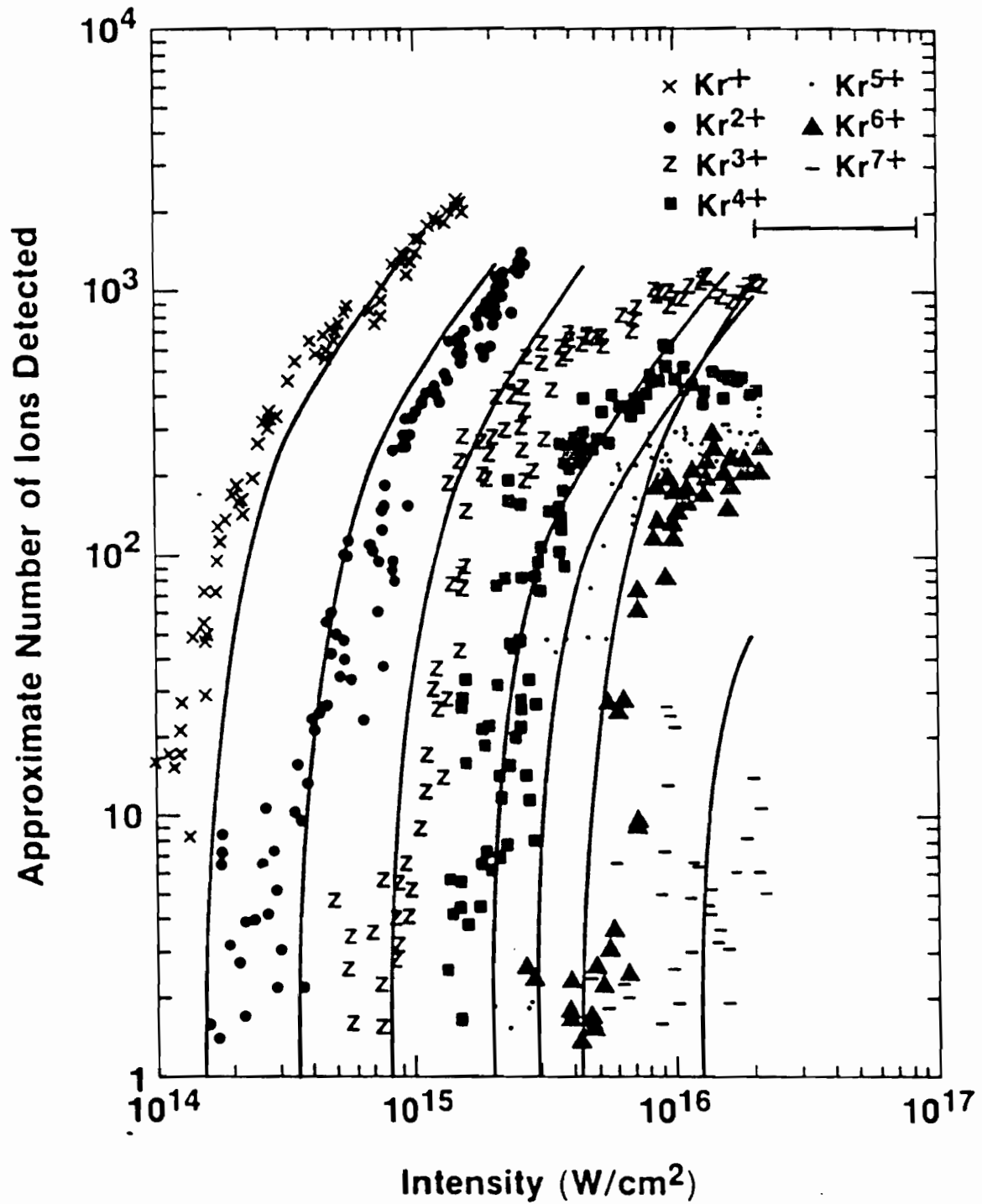


Fig. 4.6 Comparison of krypton ion data with theoretical curves calculated using the BSI model. The absolute intensity uncertainty is indicated.

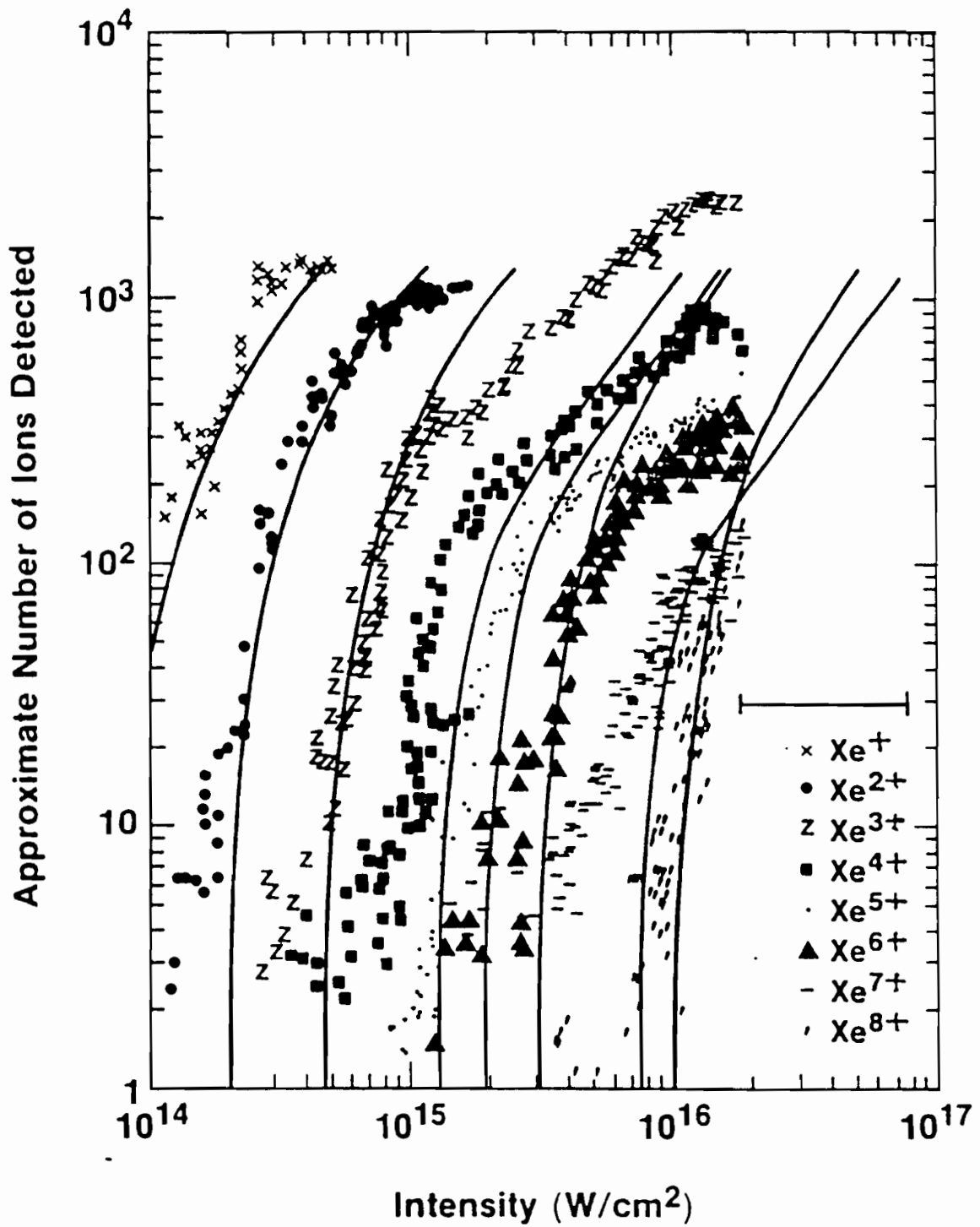


Fig. 4.7 Comparison of xenon ion data with theoretical curves calculated using the BSI model. The absolute intensity uncertainty is indicated.

A feature of the theoretical curves which might cause some confusion is the crossing of the seventh and eighth charge states. The xenon data (Fig. 4.7) also shows some experimental evidence for this crossing although the evidence is suggestive rather than conclusive. This crossing is present in all the theoretical ion curves and it is due to volumetric effects. Since the eighth ionization of a noble gas removes the last electron from a closed shell, a very large increase in intensity is needed to remove the ninth electron which comes from another shell. As the intensity is increased well beyond the threshold for creation of the eighth charge state a large percentage of the 7+ ions become further ionized to 8+ but very few of the 8+ ions become ionized to 9+. This means that the eighth charge state is severely depleting the population of the seventh but very little depletion of the eighth charge state occurs from the creation of the ninth charge state which results in a crossing of the ion production curves.

For example, the BSI threshold intensities for the seventh, eighth, and ninth charge states of xenon are  $7.5 \times 10^{15}$ ,  $9.8 \times 10^{15}$ , and  $4.2 \times 10^{16}$  W/cm<sup>2</sup>. If the laser intensity is  $4.2 \times 10^{16}$  W/cm<sup>2</sup> then the volume inside the 23% contour will be totally Xe<sup>8+</sup> and the volume between the 18% and the 23% contour will be Xe<sup>7+</sup>. If we use a value of  $w_o = 19 \mu\text{m}$  in the volume formula (Eqn. 4.2) we find a volume of  $1.7 \times 10^{-6}$  cm<sup>3</sup> between the 18% and the 23% contours and  $2.5 \times 10^{-6}$  cm<sup>3</sup> inside the 23% contour. The volume with Xe<sup>8+</sup> is approximately twice as big as the volume with Xe<sup>7+</sup> resulting in  $6.0 \times 10^5$  Xe<sup>8+</sup> ions and  $3.1 \times 10^5$  Xe<sup>7+</sup> ions for a gas density of  $5 \times 10^{-6}$  Torr ( $1.8 \times 10^{11}$  cm<sup>-3</sup>).

#### IV.C. ADK Theory

The model developed by Ammosov, Delone, and Krainov (ADK)<sup>76</sup> is an extension of the 3-dimensional dc tunneling model. The 3-dimensional dc tunneling model supplies the tunneling ionization rate for a hydrogen atom in a static electric field and is given by<sup>73,77</sup>:

$$W_i = 4\omega_A \frac{(2E_i)^{5/2}}{\mathcal{E}} \exp\left[-\frac{2(2E_i)^{3/2}}{3\mathcal{E}}\right]. \quad (4.8)$$

Perelomov *et al.*<sup>78</sup> introduced an atomic shell dependence and an oscillatory electric field to this model resulting in an ionization rate of

$$W_i = \omega_A C_{n^*l}^2 f_i(l,m) E_i \left(\frac{3\mathcal{E}}{\pi(2E_i)^{3/2}}\right)^{1/2} \left[\frac{2}{\mathcal{E}}(2E_i)^{3/2}\right]^{2n^* - |m| - 1} \\ \times \exp\left[-\frac{2}{3\mathcal{E}}(2E_i)^{3/2}\right], \quad (4.9)$$

where the factor  $f$  is given by

$$f(l,m) = \frac{(2l+1)(l+|m|)!}{2^{|m|}(|m|)!(l-|m|)!}. \quad (4.10)$$

The term  $[3\mathcal{E}/\pi(2E)^{3/2}]^{1/2}$  in Eqn. (4.9) results from averaging over one period of the laser, and for the laser parameters discussed here, it is typically of order  $10^{-1}$ . Atomic structure is introduced through the factors  $f(l,m)$  and  $C_{n^*l}$ , but Perelomov *et al.*<sup>78</sup> did not derive an expression for the  $C_{n^*l}$ 's. Ammosov *et al.*<sup>76</sup> extended the theory by deriving an approximate expression for the  $C_{n^*l}$ 's. This was accomplished by joining the asymptotic wave function of the free electron with the quasiclassical radial wave function of a bound electron.<sup>79</sup> The quasiclassical condition

is satisfied when the de Broglie wavelengths of particles are small compared to the characteristic dimensions which determine the conditions of the problem, or more specifically "... the wavelength of the particle must vary only slightly over distances of the order of itself."<sup>79</sup> This implies that the momentum of the particle cannot be too small since the de Broglie wavelength would then become large. The constraint on the momentum is why this is called the quasiclassical approximation.

The approximation begins by defining the wavefunction as

$$\psi = A \exp(i\sigma/\hbar) \quad (4.11)$$

and expanding  $\sigma$  in a power series in  $\hbar$

$$\sigma = \sigma_0 + (\hbar/i)\sigma_1 + (\hbar/i)^2\sigma_2 + \dots \quad (4.12)$$

Using this wavefunction in Schrödinger's equation and keeping terms to order  $\hbar$ , appropriate boundary conditions can be applied and a solution for  $\sigma$  and  $A$  can be found. This procedure was performed by Perelomov and Ammosov to yield the quasiclassical tunneling ionization rate (Eqn. 4.9).

The initial atomic or ionic state is described by the effective principal quantum number  $n^*$ , the orbital angular momentum, and the magnetic quantum numbers  $l$  and  $m$ . A species dependent ionization rate results from this inclusion of  $n^*$  in the theory. The expression for  $C_{n^*l}$  is given by Ammosov as<sup>76</sup>

$$C_{n^*l} = \left(\frac{2e}{n^*}\right)^{n^*} \frac{1}{(2\pi n^*)^{1/2}}, \quad (4.13)$$

where  $e = 2.71828\dots$ . For ionization rate calculations, we have used the ground state values<sup>80</sup> for  $n^*$  and  $l$  and a summation over the degenerate  $m$  states.

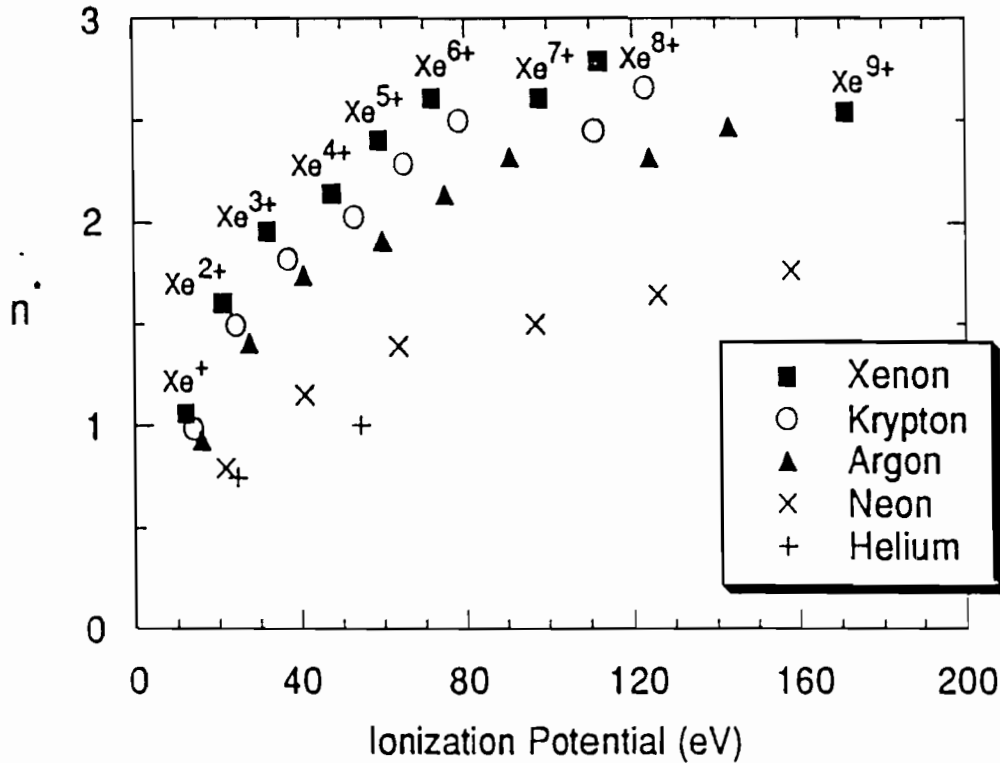


Fig. 4.8 The effective principal quantum number  $n^*$  versus the sequential ionization potential for each of the charge states observed. ADK theory is expected to be valid for  $n^* \gg 1$ .

Equation (4.9) is an approximation valid for  $n^* \gg 1$ ,  $\mathcal{E}_{Laser} \ll \mathcal{E}_{Binding}$ , and  $\omega_L \ll E$ . The validity of the ADK theory improves as  $n^*$  increases, and larger  $n^*$  occurs for heavier atoms and higher charge states. A plot of  $n^*$  versus the ground state ionization potential of each of the charge states can be seen in Fig. 4.8. This graph shows that for the five noble gases under study, the agreement is expected to be best for xenon and worst for helium. A calculation of ion production is shown with the experimental data in Figs. 4.9-4.13, where the agreement is satisfactory even though  $n^*$  never exceeds a value of 3. Very large values of  $n^*$  can be obtained by exciting the atom into high lying bound levels (Rydberg atoms). It has been found that ionization

of highly excited Rydberg atoms by microwave radiation does not agree with the ADK formula.<sup>81</sup> The three validity criteria mentioned at the beginning of this paragraph remain valid for microwave ionization of Rydberg atoms (for values of  $n$  less than about 50) so it is not clear why the ADK model does not work in this case.

It should be noted that ADK and BSI theories both predict the correct spacing for all charge states observed ( $E^4/Z^2$  dependence), but the fit between the ADK theory and the data from the lighter noble gases (helium, neon, and argon) has an absolute error in the threshold intensities. The agreement with ADK improves for increasing atomic number since  $n^*$  is also increasing, and the slope for low ion number agrees with experiment better than the BSI theory. It should be noted that the absolute error in threshold intensities which ADK predicts for the lighter noble gases is never larger than the experimental uncertainty present in our absolute intensity measurements (a factor of 2), but it is larger than the relative uncertainty.

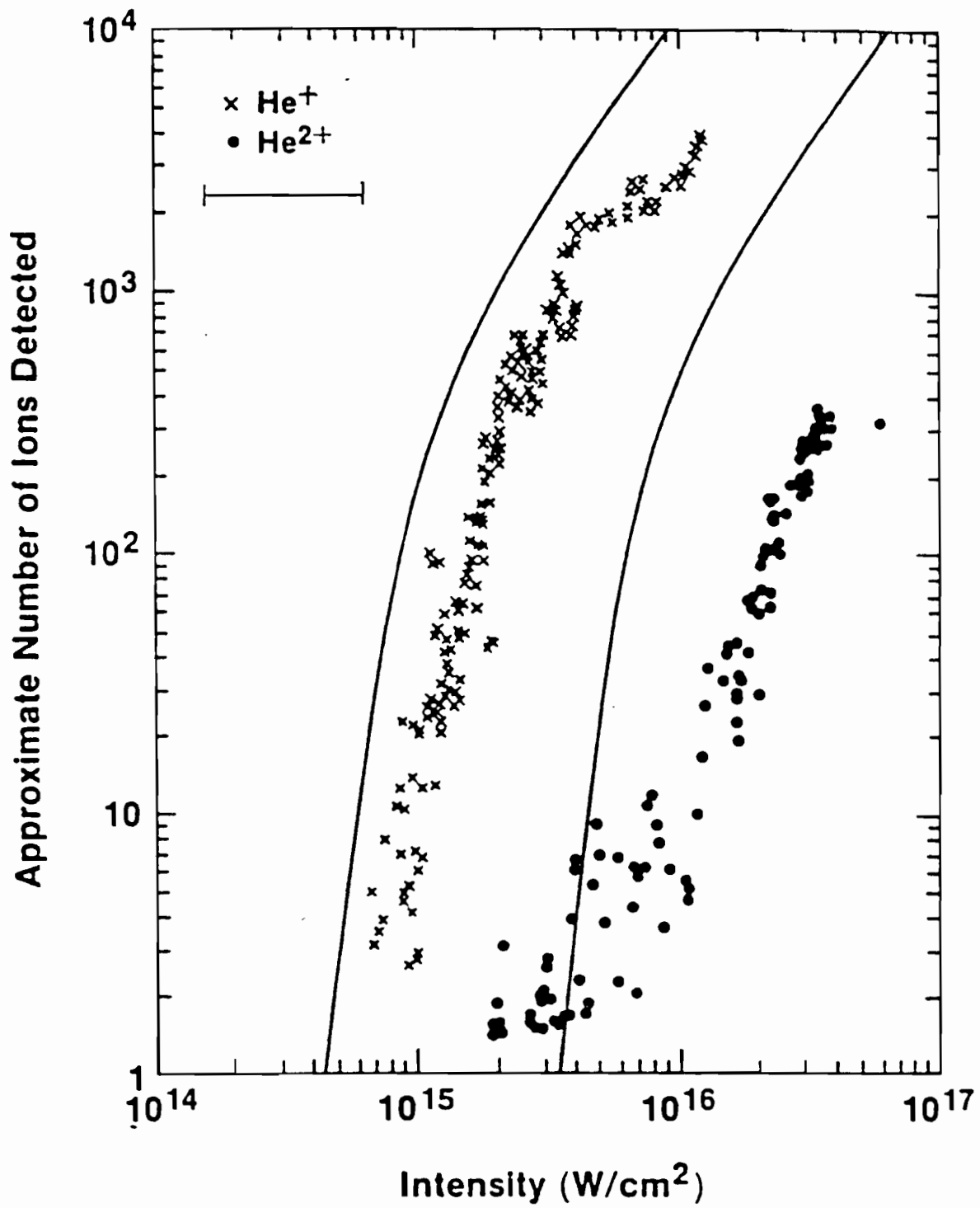


Fig. 4.9 Comparison of helium ion production and that predicted by ADK theory. The absolute intensity uncertainty is indicated.

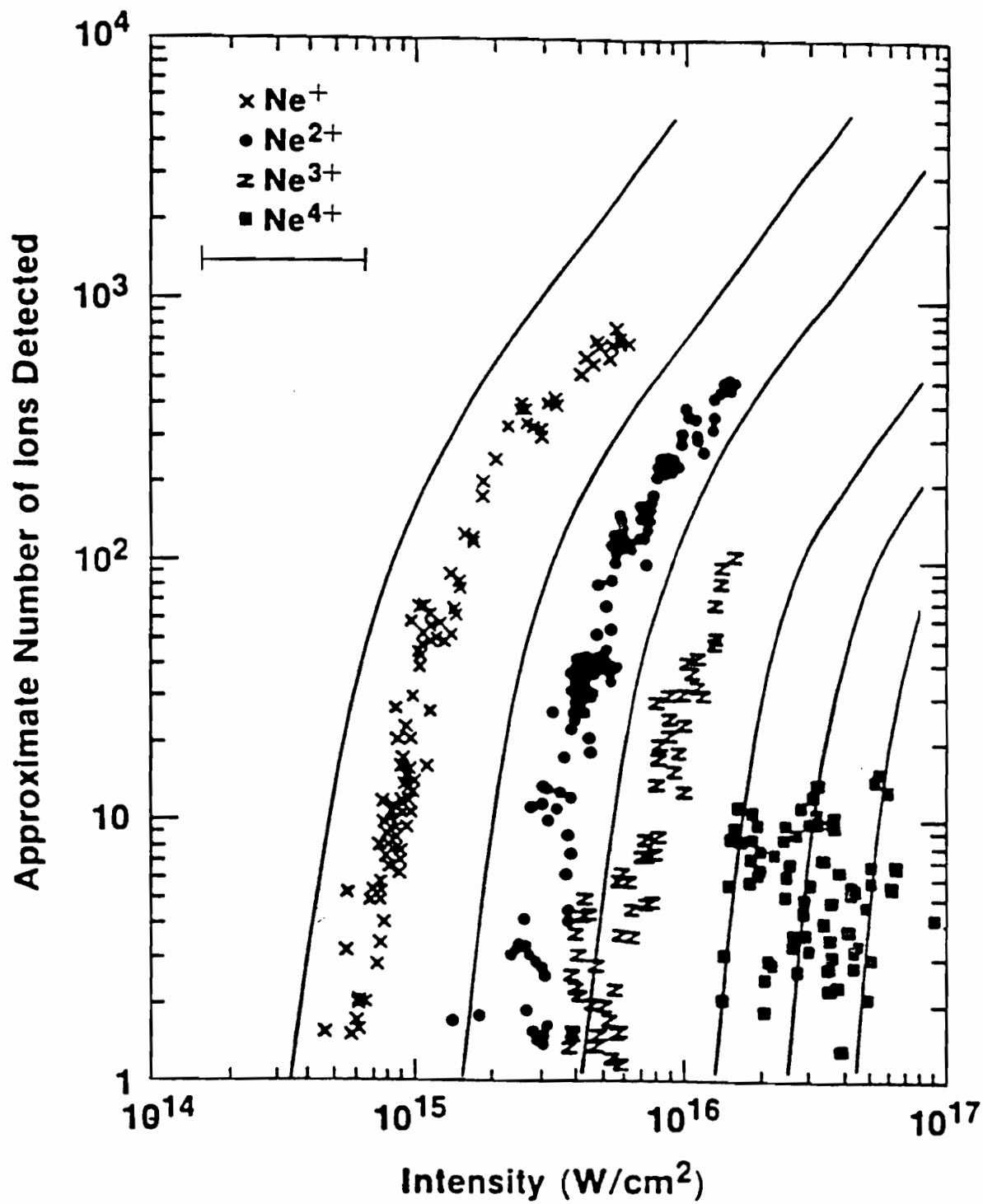


Fig. 4.10 Comparison of neon ion production and that predicted by ADK theory.

The absolute intensity uncertainty is indicated.

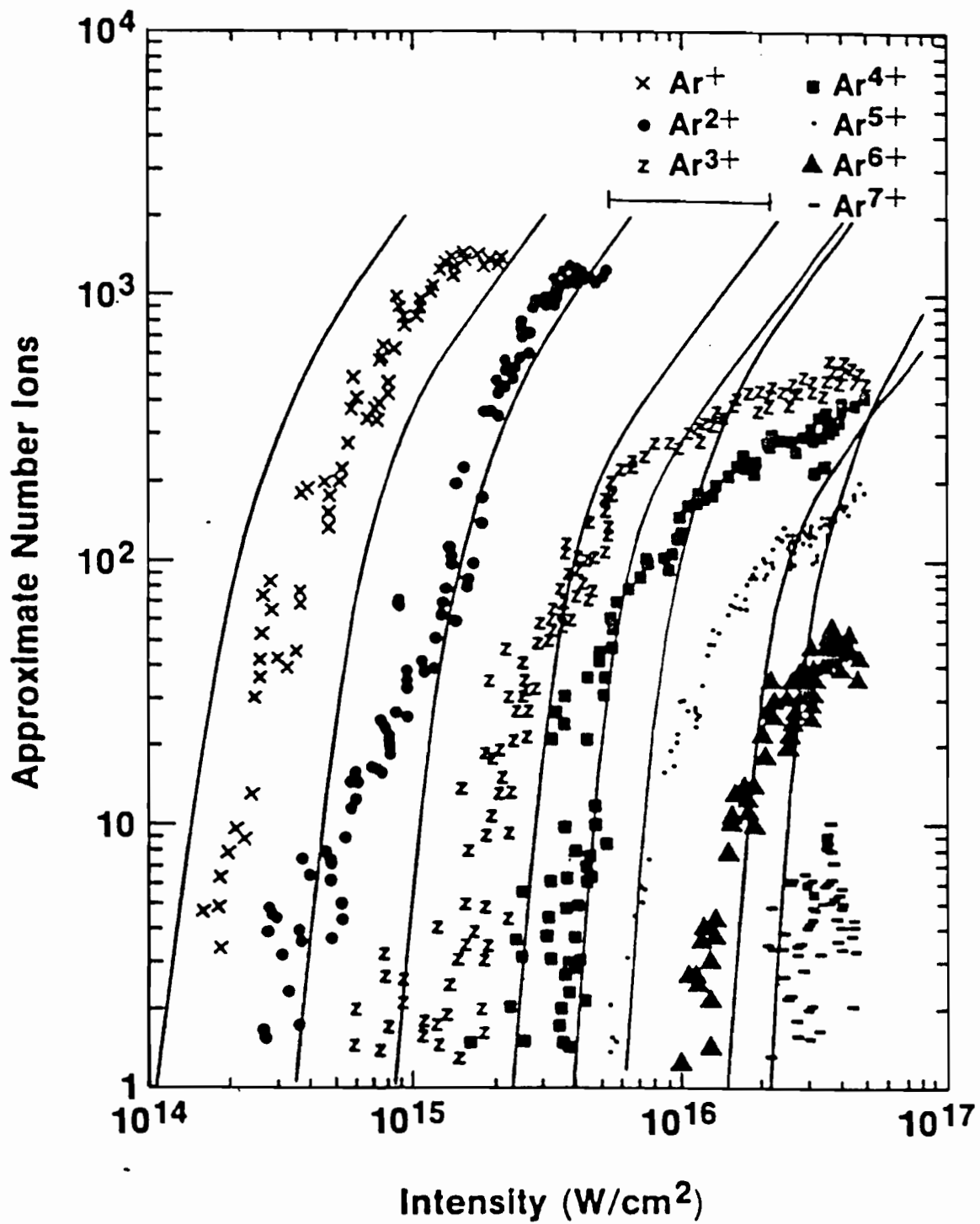


Fig. 4.11 Comparison of argon ion production and that predicted by ADK theory.

The absolute intensity uncertainty is indicated.

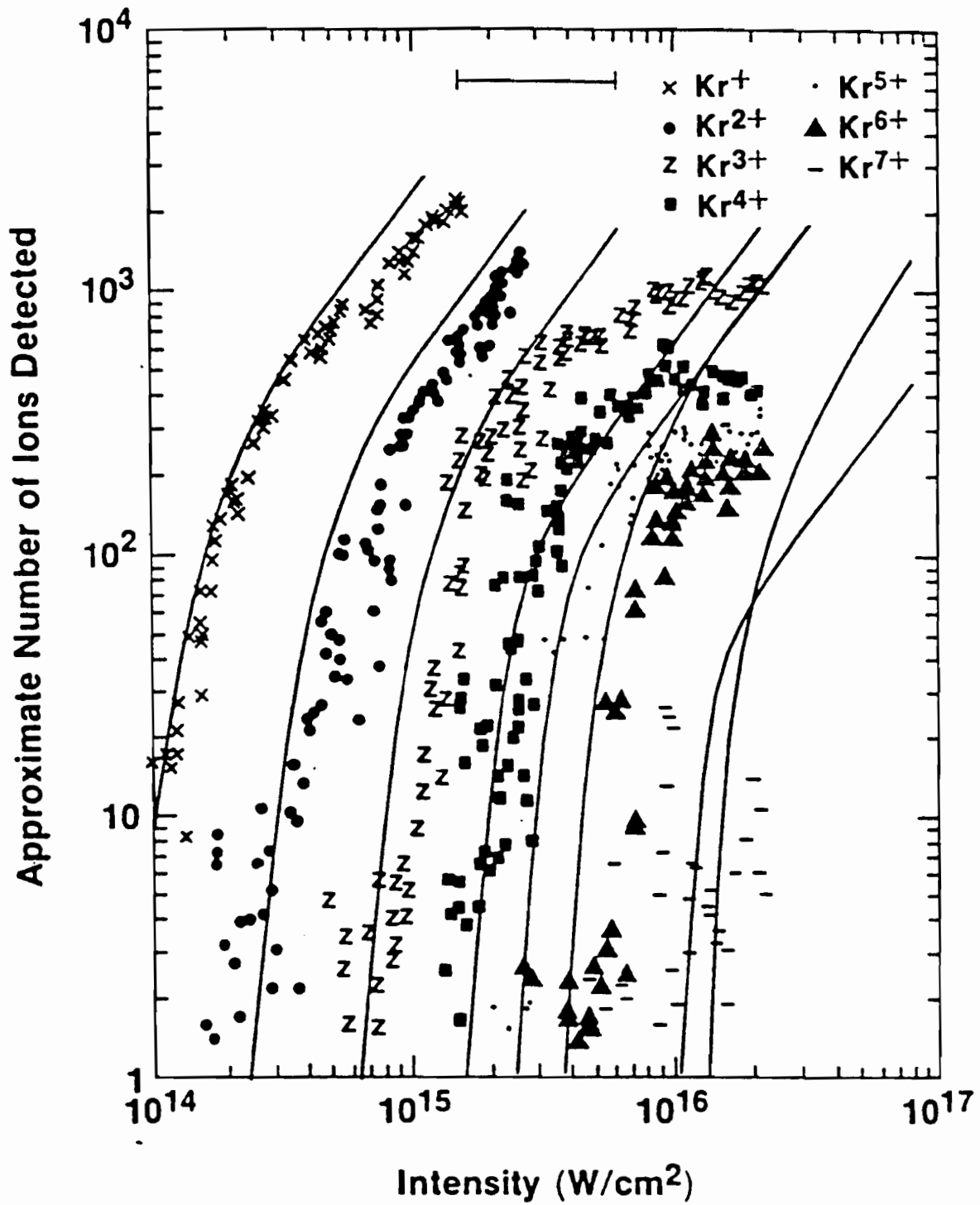


Fig. 4.12 Comparison of krypton ion production and that predicted by ADK theory. The absolute intensity uncertainty is indicated.

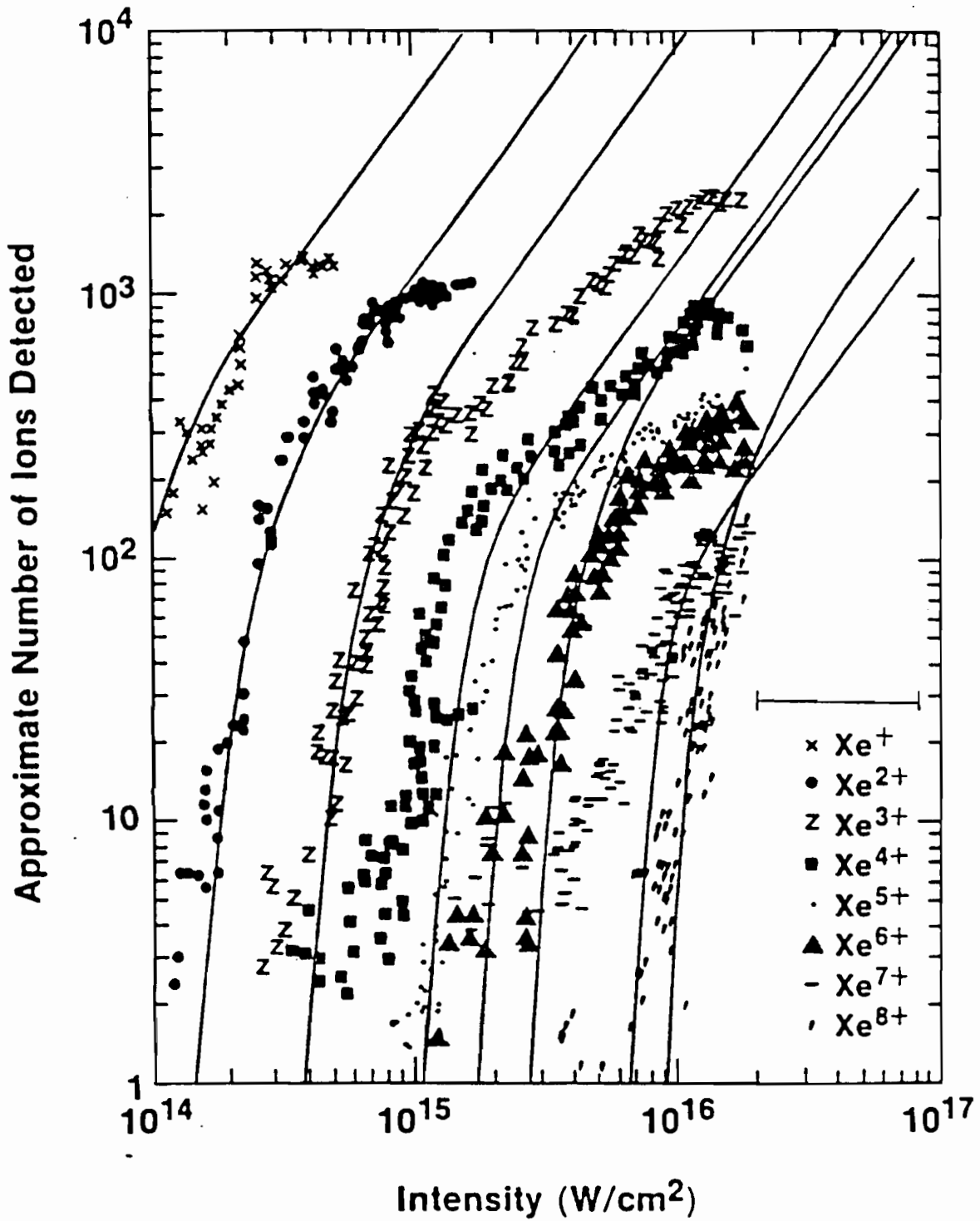


Fig. 4.13 Comparison of xenon ion production and that predicted by ADK theory.

The absolute intensity uncertainty is indicated.

The ADK theory provides an ionization rate in contrast to the BSI model which predicts an ionization probability of 100% for intensities above a certain threshold and 0% ionization probability below the threshold. This means that the BSI will show discontinuous jumps in the spatial profile of ion density and the ADK theory will have continuous transitions across the threshold. Figure 4.14 shows the charge distribution as a function of radial position at the focal waist assuming the ionization occurs according to either the BSI or the ADK tunneling model. Despite the fact that the ADK model does not have discontinuities built into the theory, the high degree of non-

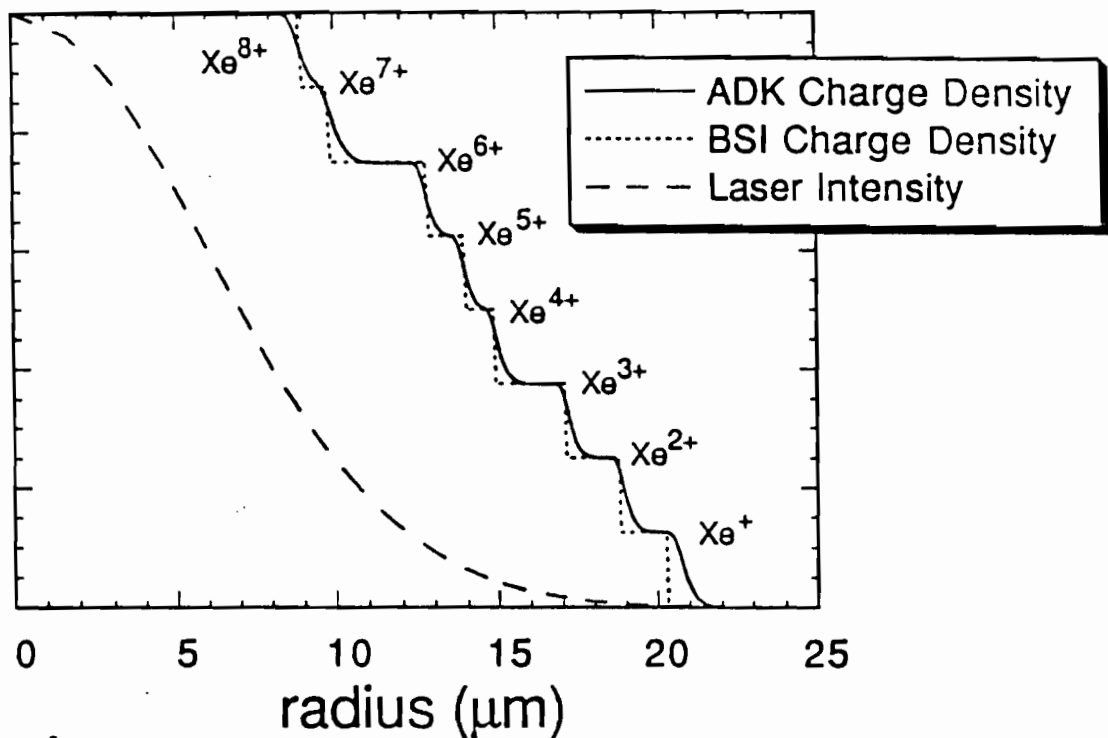


Fig. 4.14 Predicted charge density as a function of radial distance using the ADK and BSI models at a laser intensity of  $3 \times 10^{16}$  W/cm<sup>2</sup>. The corresponding laser profile is also shown.

linearity in the ionization process causes the charge distribution to display large gradients similar to BSI as the ionization moves from one charge state to the next. This again leads to a larger volume of  $\text{Xe}^{8+}$  than  $\text{Xe}^{7+}$  and a crossing of the ion production curves occurs.

The remaining four theories cannot fit all of the data since they include no species dependence, but they are still of interest for several reasons. First, a comparison of spacing among charge states can be made with the data; and second, the absolute magnitude of the ionization probabilities can be compared to those shown in the data. Also, the theory described in section (IV.F.) has been shown to be in good agreement with previous experiments<sup>24</sup> so here we test whether it is still applicable under different laser conditions.

#### IV.D. Keldysh Theory

This theory<sup>19</sup> perturbatively calculates the transition rate from a hydrogenic ground state to a free electron oscillating in the laser field (a nonperturbative Volkov final state<sup>20</sup>). The difference from usual perturbation theory is only that the final state is not stationary but it exactly accounts for the oscillation of the electron in the laser field. The residual influence of the long-ranged Coulomb potential of the remaining ion is not directly included in the final state, but Keldysh introduces a correction factor (for which no derivation is given) to account for the Coulomb interaction. The ionization rate in the limiting case of small  $\gamma = (2E)^{1/2}\omega_L/\mathcal{E}$  (i.e., large ponderomotive potential) is given [by Eqn. (20) of Ref. 19] as:

$$W_i = \frac{\omega_A \sqrt{6\pi}}{2^{3/4}} E_i \left( \frac{\mathcal{E}}{(2E_i)^{3/2}} \right)^{1/2} \exp\left( - \frac{2(2E_i)^{3/2}}{3\mathcal{E}} \left( 1 - \frac{\omega_L^2 E_i}{5\mathcal{E}^2} \right) \right). \quad (4.14)$$

The Coulomb correction factor which Keldysh introduces can be included by multiplying the right side of Eqn. 4.14 by

$$\frac{\sqrt{2E_i^3}}{\sqrt{E^2 + 2E_i\omega_L^2}} \quad (4.15)$$

A comparison of the uncorrected and corrected forms is shown in Fig. 4.15. The correction for the Coulomb field reduces the ionization rate and consequently a higher intensity is needed to produce the same number of ions. When the correction factor is included, the theoretical prediction matches our data better than when the correction factor is ignored. A comparison between the corrected theory and our xenon data is shown in Fig. 4.16. The first charge state is matched quite well but the spacing between charge states is too wide. This theory does not incorporate any charge state dependence into the rate calculation.

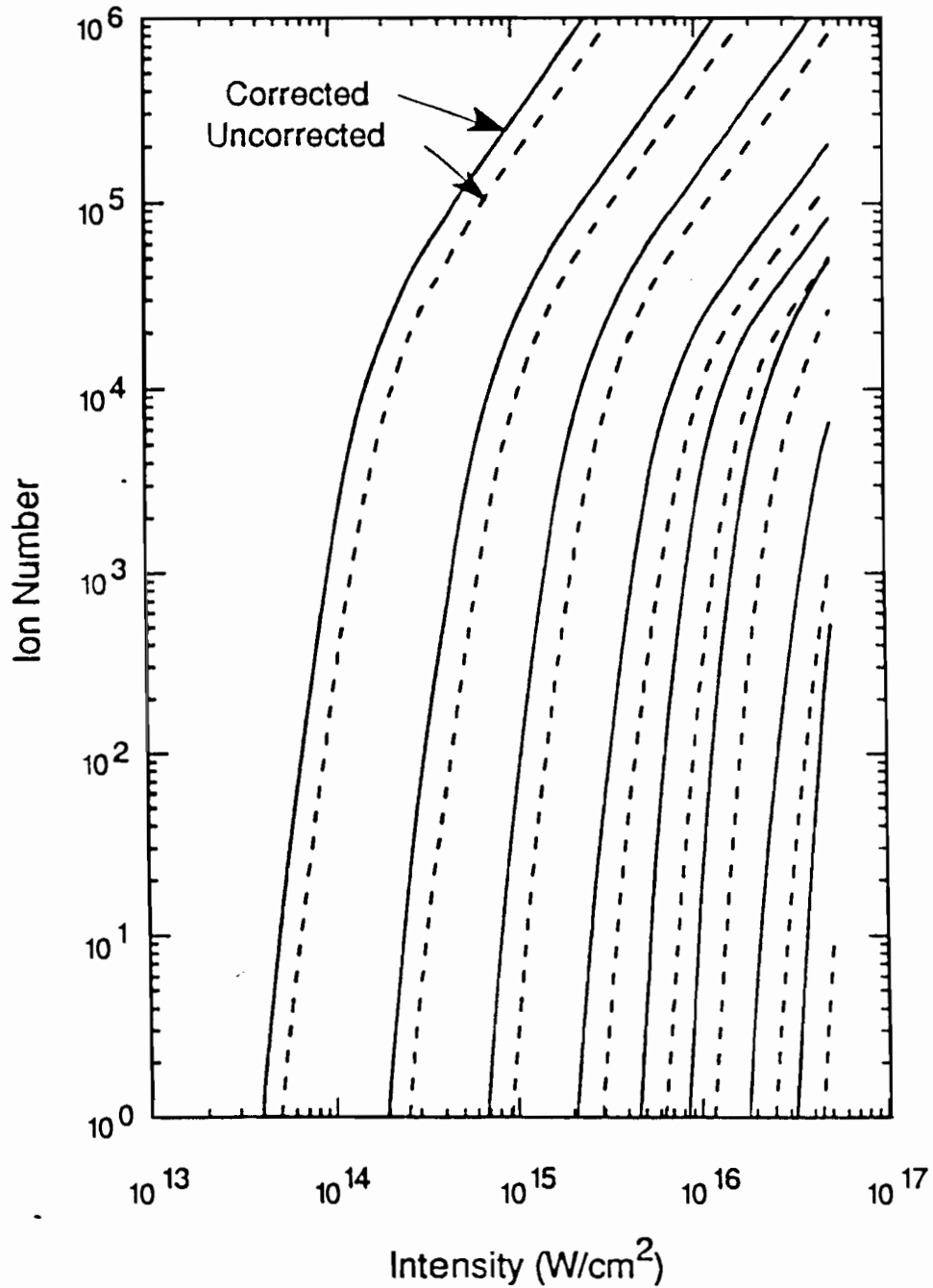


Fig. 4.15 Comparison of the two forms of Keldysh's theory for ionization of xenon at 1  $\mu\text{m}$  wavelength and 1 ps pulse length. The corrected form accounts for the Coulomb potential in the wavefunction of the ionized electron.

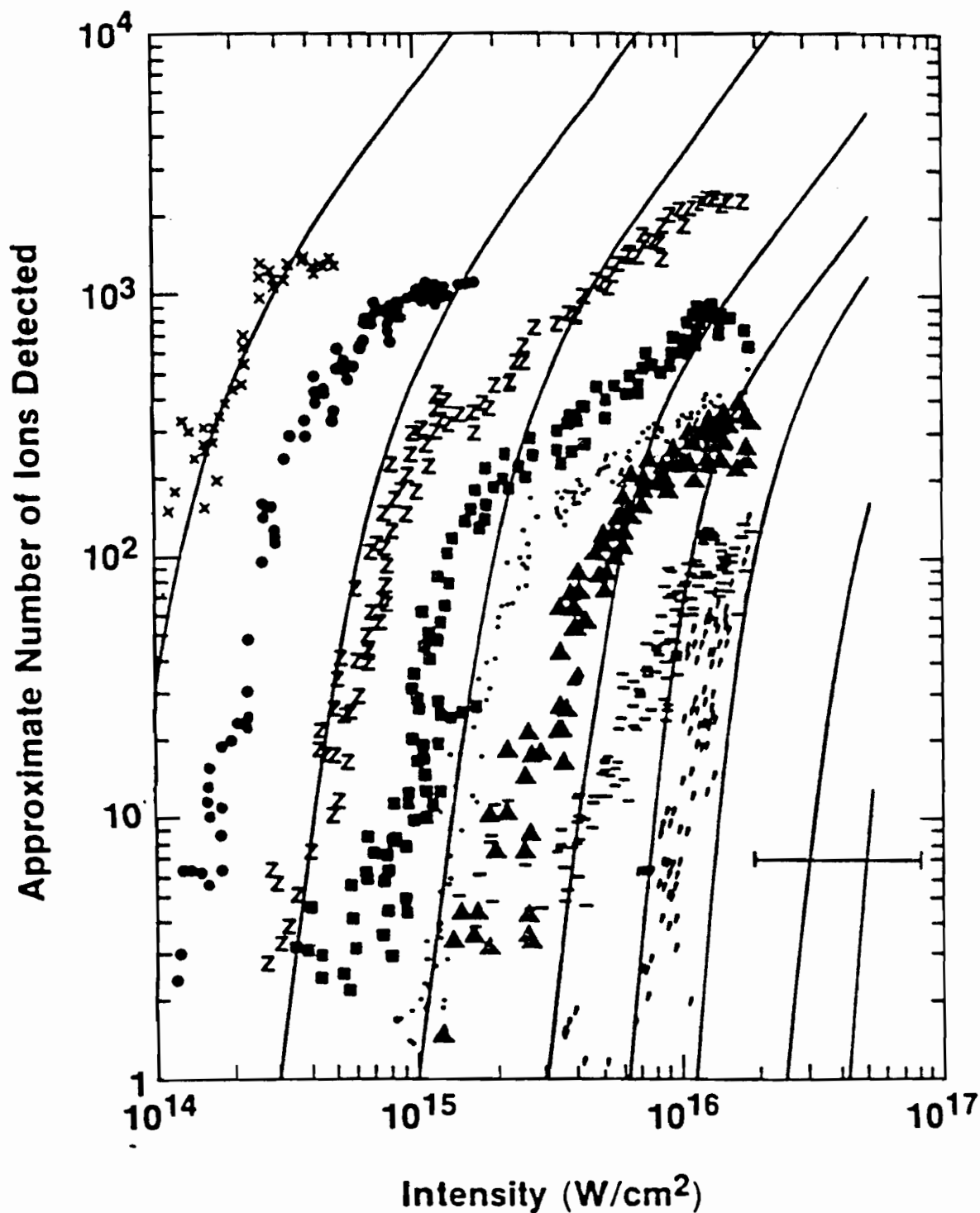


Fig. 4.16 Comparison of xenon ion production and that predicted by the Coulomb-corrected Keldysh theory. The absolute intensity uncertainty is indicated.

#### IV.E. Keldysh-Faisal-Reiss (KFR) Theory

Keldysh-Faisal-Reiss theory<sup>19,21,22</sup> is based upon the "Keldysh approximation" which means the ionization rate is again found by calculating the transition rate from an initial bound state to a final Volkov state. The modification which KFR theory makes to Keldysh theory is that the calculations are done in "radiation gauge" instead of "electric-field gauge" which makes it easier to solve for the ionization rate analytically without resorting to the low field-frequency approximation which Keldysh employed in his calculation. The residual effects of the Coulomb potential on the final state are ignored completely. Reiss derives an expression for the differential transition rate [Eqn. (45) in Ref. 22]  $dW/d\Omega$  which depends upon the initial momentum-space wave function  $\phi(\mathbf{p})$ . For linearly polarized light

$$\frac{dW_i}{d\Omega} = \frac{(2\omega_L^3)^{1/2}}{(2\pi)^2} \sum_{n=N^{(i)}}^{\infty} (n - n_{osc})^2 (n - n_{osc} - n_b^{(i)})^{1/2} |\phi(\mathbf{p})|^2 J_n^2\left(n_f^{(i)}, -\frac{1}{2}n_{osc}\right). \quad (4.16)$$

The momentum-space wavefunction can be found by taking the Fourier transform of the spatial coordinate wavefunction. Momentum-space hydrogenic wavefunctions can also be found by transforming Schrödinger's equation and then solving for the momentum-space wavefunctions directly.<sup>82</sup> The initial state wavefunction in Eqn. (4.16) can be approximated with a hydrogenic ground state wave function which is given by

$$\phi(\mathbf{p}) = \frac{8(\pi a_0^3)^{1/2}}{(1 + p^2 a_0^2)^2}. \quad (4.17)$$

where  $a_o$  is the Bohr radius ( $a_o^{-2} = 2E$ ) and energy conservation constrains the momentum to values of  $p = [2\omega_L(n - n_{osc} - n_b)]^{1/2}$ . This yields an ionization rate of:

$$W_i = 32 \omega_L (n_b^{(i)})^{5/2} \sum_{n = N_o^{(i)}}^{\infty} \frac{(n - n_{osc} - n_b^{(i)})^{1/2}}{(n - n_{osc})^2} \int_0^1 J_n^2\left(n_f^{(i)}, -\frac{1}{2} n_{osc}\right) d\mu, \quad (4.18)$$

where  $\omega_L$  is the laser frequency,  $J_n(\mu, \nu)$  are generalized Bessel functions,<sup>22</sup>  $n_{osc} \equiv U_p/\omega_L$  is the ratio of the ponderomotive potential to the photon energy,  $n_b \equiv E/\omega_L$  is the ratio of the binding potential to the photon energy,  $N_o$  is the smallest integer which exceeds  $(n_b + n_{osc})$ ,  $n_f = [8n_{osc}(n - n_{osc} - n_b)]^{1/2}\mu$ , and  $\mu = \cos\theta$ , where  $\theta$  is the angle between the direction of motion of an outgoing electron and the polarization of the laser field.

In the high intensity limit Eqn. (4.18) predicts an exponential dependence for the rate:

$$W_i \propto \exp\left[-\frac{2(2E_i)^{3/2}}{3\mathcal{E}}\right] \quad (4.19)$$

which is the standard tunneling factor. The initial-state wave function used in the derivation of Eqn. (4.18) was a ground-state hydrogen wave function. In the case of helium, both electrons are in the 1s shell, and the singly charged ion is exactly hydrogenic. This is in contrast to the other four gases which have  $p$ -orbital initial states. Since an  $s$ -shell is assumed in Eqn. (4.17), one would expect Eqn. (4.18) to predict the ionization rate more accurately for helium than for the other four gases. This is the case, and in fact KFR theory predicts ion production for the helium charge states more accurately than any other theory mentioned here [see Fig. 4.17]. For comparison Fig. 4.18 shows the calculated curves for xenon. The calculated appearance intensities

for xenon are high by almost a factor of 2 and the spacing between charge states is too large. Only the first five charge states are shown since this rate becomes computationally lengthy at high intensities. The good agreement with helium and the poor agreement with xenon suggest that the primary limitation of Eqn. (4.18) is its use of a ground-state hydrogenic wavefunction to model complex atoms.

Recent calculations by Reiss<sup>83</sup> have shown better agreement with our ionization data. The modification which he has employed is to use a more accurate initial state wavefunction. The initial wavefunction is still hydrogenic but a scaled  $n = 5, l = 1$  state is used with the ionization potential scaled appropriately. Further details of the calculation are not currently known.

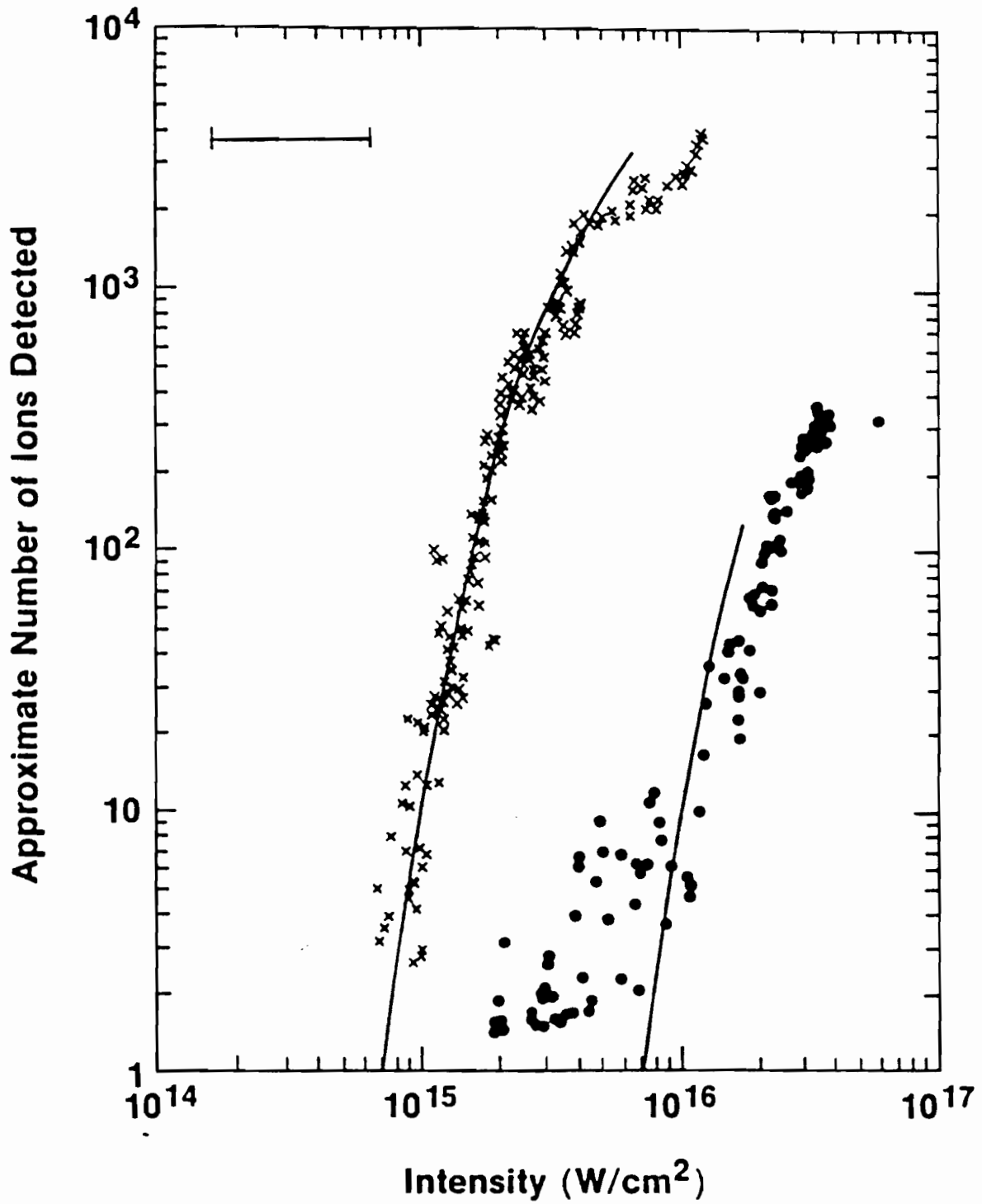


Fig. 4.17 Comparison of helium ion production and that predicted by KFR theory. The absolute intensity uncertainty is indicated.

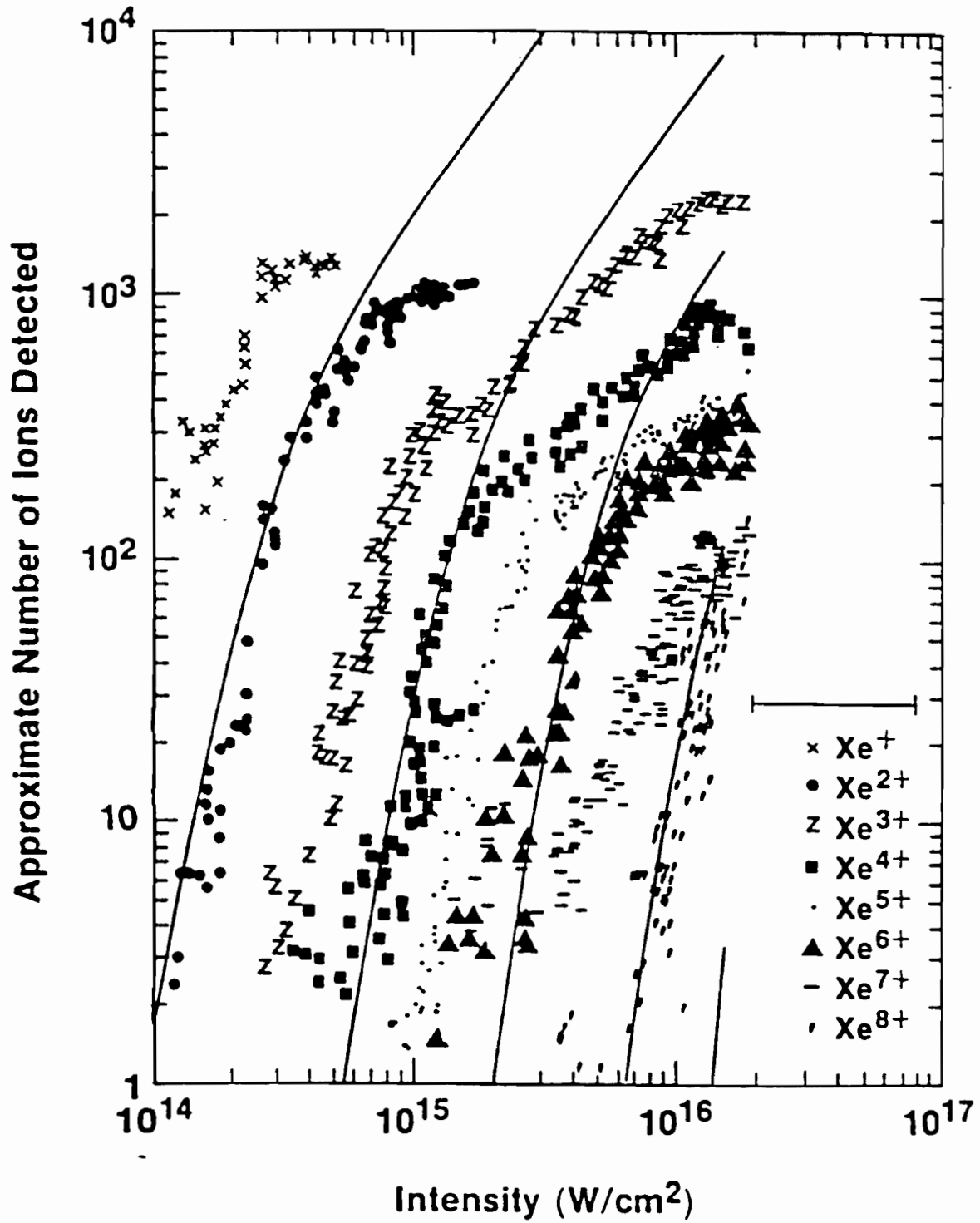


Fig. 4.18 Comparison of xenon ion production and that predicted by KFR theory.

The absolute intensity uncertainty is indicated.

#### IV.F. Constant Potential Modification to KFR Theory

This theory<sup>23,24</sup> is a modification of Keldysh-Faisal-Reiss (KFR) theory.<sup>19,21,22</sup> The modification superimposes a constant potential (whose depth is equal to the ionization potential) and the oscillating electric field potential of the laser to calculate the final Volkov state. The resulting ionization rate is very similar to that given for KFR theory above. The two differences occur in the pre-integral factor containing "n's" and in the definition of  $n_f$ . The rate is given as:<sup>23,24</sup>

$$W_i = 32 \omega_L (n_b^{(i)})^{5/2} \sum_{n=N_b^{(i)}}^{\infty} \frac{n^2 (n - n_b^{(i)} - n_{osc})}{(n - n_{osc})^{1/2} (n + n_b^{(i)} - n_{osc})^4} \times \int_0^1 J_n^2 \left( n_f^{(i)}, -\frac{1}{2} n_{osc} \right) d\mu, \quad (4.20)$$

where  $n_f = [8n_{osc}(n - n_{osc})]^{1/2} \mu$  and a ground state hydrogenic wavefunction is used for the initial state. Although this theory agrees well with results obtained at a wavelength of 586 nm,<sup>24</sup> the agreement with our higher intensity data acquired using a 1.053- $\mu$ m wavelength laser is rather poor. This is not surprising since the *ad hoc* constant potential cannot correctly model the Coulomb potential when the range of the classical quiver motion of the electrons is of the order of or larger than the atomic radius.<sup>24</sup> The calculated appearance intensities are a factor of 4 low at best, and the theoretical spacing between charge states is much closer than that observed in our experiments [see Fig. 4.19].

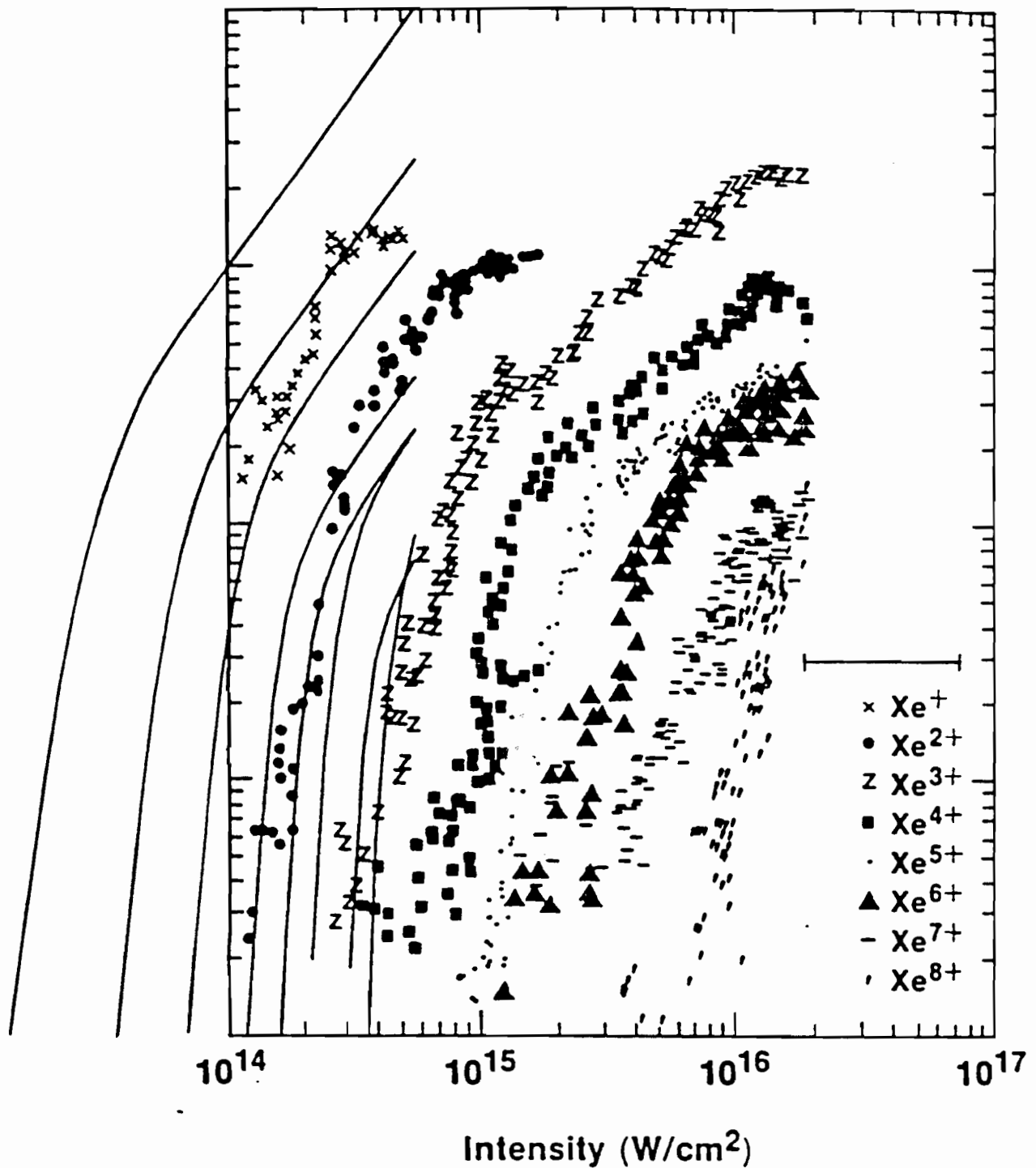


Fig. 4.19 Comparison of xenon ion production and that predicted by the Constant Potential Modification to Keldysh-Faisal-Reiss (KFR) theory. The absolute intensity uncertainty is indicated.

#### IV.G. Thomas-Fermi models

Thomas-Fermi models which utilize the superposition of a Coulomb field and a static electric field have recently been proposed.<sup>84-87</sup> These models, in contrast to BSI, present a self-consistent expression for the ionization potential. At the time of this writing, we have not calculated ion production rates using these models, but the authors have made this comparison for us. The two theoretical groups have obtained different results [see Fig. 4.20]. As the authors say:<sup>87</sup> "... the source of the discrepancy [between the two results] is unclear." The model used by Brewczyk *et al.*<sup>84</sup> shows much better agreement with longer pulse length experiments done at a 10  $\mu\text{m}$  wavelength<sup>84</sup> than it does with the LLE data. This is most likely due to the lower frequency which makes a quasi-static approximation more valid.

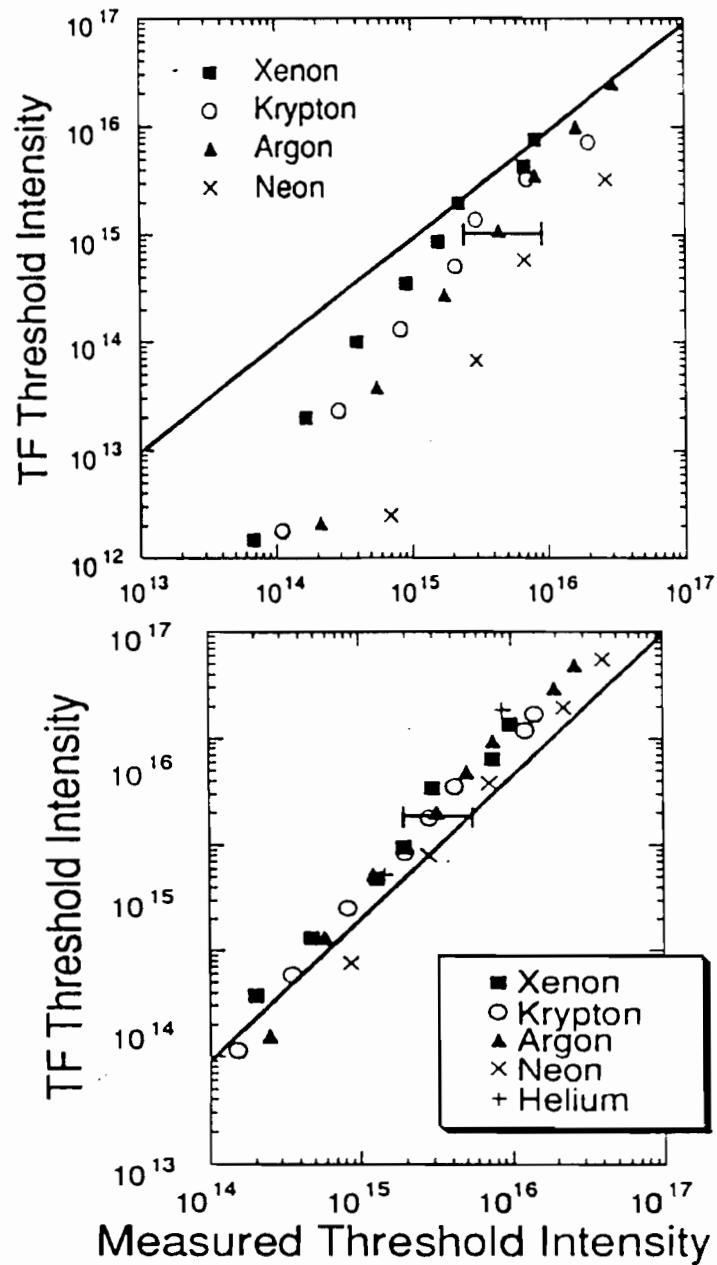


Fig. 4.20 Comparison of experimentally determined and theoretically predicted threshold intensities using two Thomas-Fermi models. The solid line corresponds to exact agreement. (a) is from reference [86] and (b) is from Fig. 4 of reference [87] ( $Xe^+$  is missing in their Fig. 4 so it could not be plotted here either).

## CHAPTER FIVE

### ADDITIONAL IONIZATION EXPERIMENTS

A second set of ionization experiments has been performed to address some questions which arose while analyzing the first set. These results are incomplete in some cases and in the next chapter I will suggest additional experiments which should be done in the future. All data shown in this chapter have been taken with multiple fill pressures and in some cases differing focal length lenses so the ion number in each graph has been scaled to  $5 \times 10^{-5}$  Torr pressure and  $w_0 = 19 \mu\text{m}$ .

#### V.A. Linear versus Circular Polarization and Resonant Ionization

We have measured the ion production of xenon and neon using both circularly and linearly polarized light. A lower ionization rate is expected for circular polarization since intermediate resonances between bound levels within the atom are much less accessible. Even if energy conservation predicts that a level will be resonant, circular polarization selection rules might forbid it since the electron must absorb many photons (and hence acquire a large angular momentum) before any resonance level is within reach. For example, in the noble gases the lowest excited state is at least 8 eV (at least 7 photons using  $1 \mu\text{m}$  wavelength) above the ground level. Thus, with circularly polarized excitation, an atomic level which is potentially resonant must have at least  $\ell = m = 7$  for its angular momentum quantum numbers. Figure 5.1 shows which levels are available for electron transitions resulting from the first few photons of either linear or circular polarization.

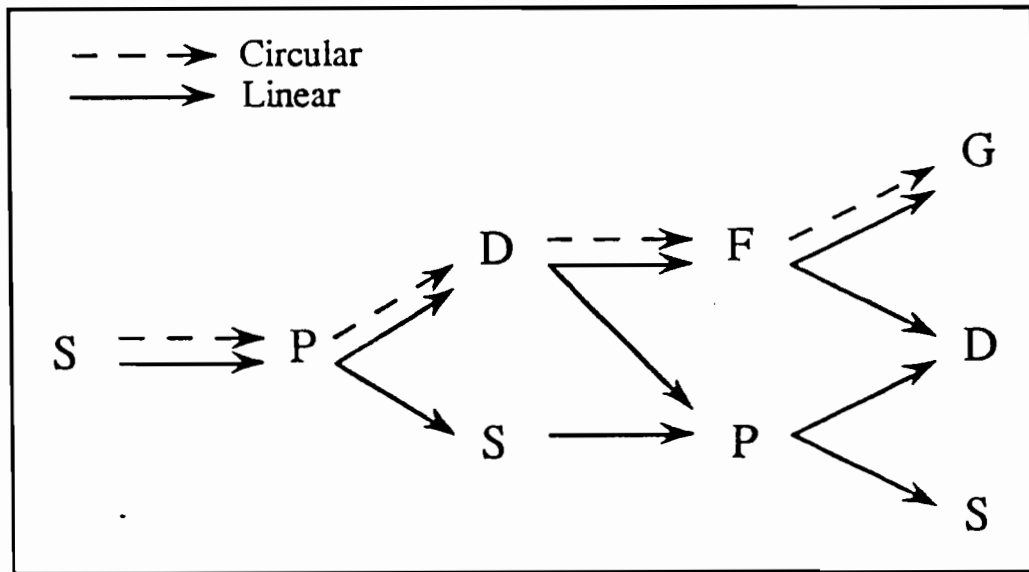


Fig. 5.1 Angular momentum channels available for dipole transitions of linearly or circularly polarized light [from Fig. 13 in reference 9]. For large photon number there will be many more resonant channels available for linearly polarized light.

Field ionization models also predict a polarization-dependent shift and this shift is a factor of two for slowly oscillating fields. The amount of predicted shift decreases somewhat for field frequencies which are larger than the ionization rate since a cycle average must then be included in the ionization rate calculation. The exact amount of shift is model and frequency dependent. The predicted shift is due to differences in peak electric field strengths. In the cases of linear and circular polarization, equal peak fields result in differing intensities. For linear polarization the electric field varies as  $\mathcal{E}_L = \mathcal{E}_0 \times \cos(\omega t)$  and for circular polarization  $\mathcal{E}_C = \mathcal{E}_0 (x \cos(\omega t) + y \sin(\omega t))$  where  $x$  and  $y$  are unit vectors. The intensity which we measure is actually the time average of the square of the electric field. In the case of linear polarization  $\langle |\mathcal{E}_L|^2 \rangle = \mathcal{E}_0^2/2$  and for circular polarization with an equal peak field  $\langle |\mathcal{E}_C|^2 \rangle = \mathcal{E}_0^2$ .

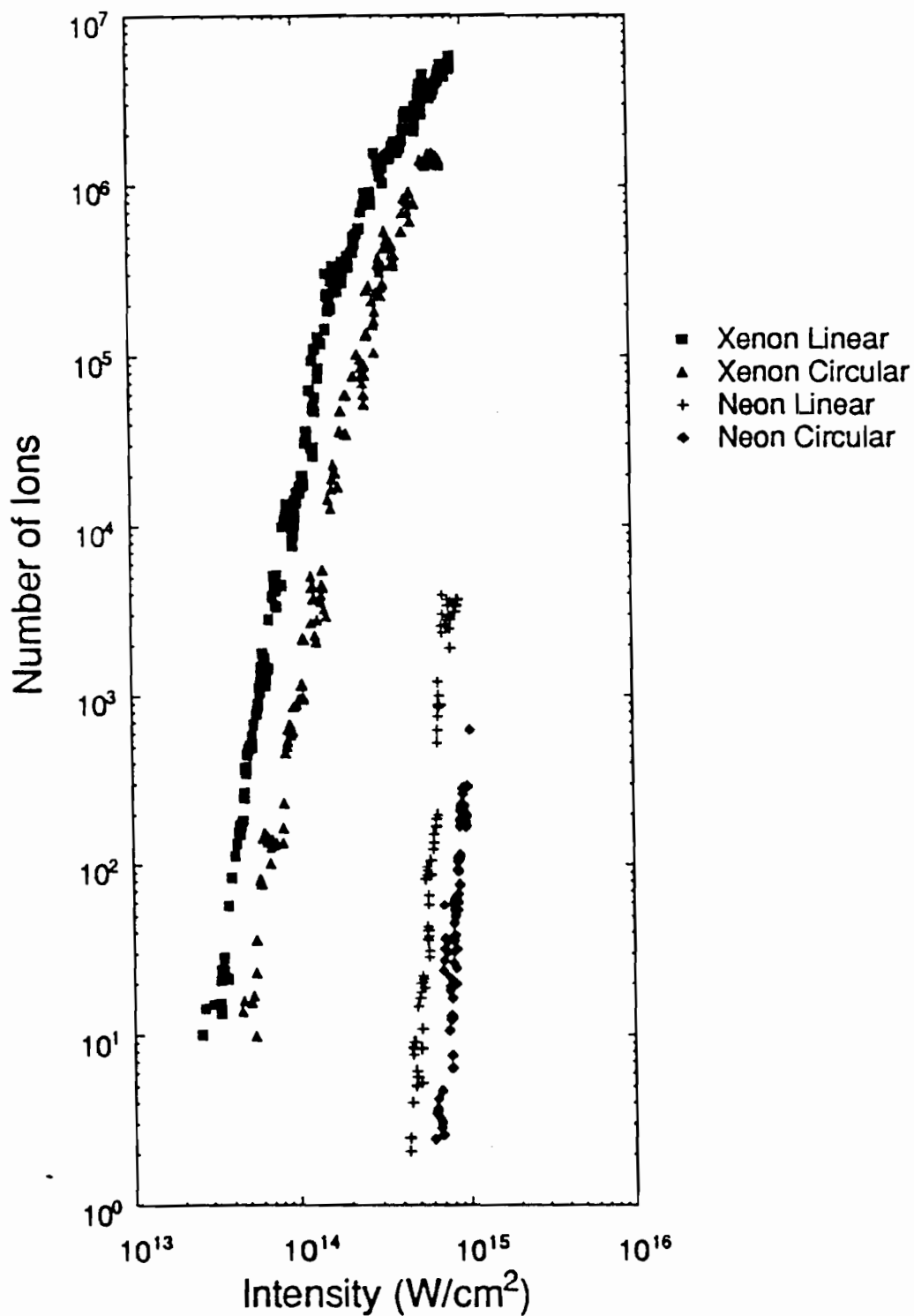


Fig. 5.2 Comparison of the production of  $\text{Xe}^+$  and  $\text{Ne}^+$  ions for linearly and circularly polarized light. The laser pulse length is 1.9 ps.

This means that to reach equal peak field strengths, circularly polarized light requires twice the intensity of linearly polarized light. If the linearly polarized case is also resonantly enhanced then the separation of the two curves will be more than a factor of two.

A comparison of the production of singly ionized xenon and neon for linearly and circularly polarized light is shown in Fig. 5.2. In the case of circular polarization an intensity increase of about  $1.7 \pm 0.1$  is required to produce the same number of xenon ions as in the linear polarization case, and a factor of  $1.5 \pm 0.1$  is required for neon. Figure 5.2 suggests that our data obtained with linearly polarized light is a non-resonant ionization process. A resonant ionization would make the linearly polarized results appear at a significantly lower intensity than seen here. This seems to contradict the electron experiments described in chapter one<sup>43-47</sup> which show that short pulse ionization is a resonant process. The difference is probably due to the laser wavelength. All of these resonant ionization experiments were done at wavelengths of about 620 nm or shorter. Our experiments are done at 1053 nm. This increase in wavelength nearly doubles the number of photons which must be absorbed.

A wavelength dependent transition from resonant to non-resonant ionization can be qualitatively understood by considering several factors. The resonant ionization rate must be larger than the non-resonant rate in order to see a difference between the two, consequently when the number of photons required for ionization becomes large, the difference between an  $(N-1)$ -photon transition and an  $N$ -photon transition can become quite small.

Ponderomotive shifts become larger as the laser wavelength increases. This means that the upper levels are being shifted in and out of resonance much faster than

they would be at a shorter wavelength. At the same time the laser period is longer which means that the atom must be in resonance for a longer period of time before any resonant enhancement can be seen.

This suggests that REMPI will not occur if the ponderomotive potential is large. A possible criterion is that it be much larger than the photon energy:  $U_p/\omega_L \gg 1$ . A large value of  $U_p$  would cause an  $N$ -photon process to become an  $N+k$  process. This increase in order makes the resonant process less significant in comparison to the non-resonant process. Very large values of  $U_p$  cause a transition from MPI to tunneling ionization which appears to be a non-resonant process. The  $U_p/\omega_L \gg 1$  criterion can be rewritten as  $\mathcal{E}^2 \gg 4\omega_L^3$  so a decrease in frequency by a factor of two means the intensity can be decreased by an order of magnitude before resonant enhancement effects become important (see Table 5.1). The  $\mathcal{E}^2 \gg 4\omega_L^3$  criterion has not been exceeded in any short pulse REMPI experiments published to date. The LLE experiments have been performed mainly in the  $\mathcal{E}^2 \gg 4\omega_L^3$  regime so resonant enhancement may not be expected.

<u>Wavelength (nm)</u>	<u>Frequency (a.u.)</u>	<u>Intensity (W/cm<sup>2</sup>)</u>
1053	0.043	$1.1 \times 10^{13}$
620	0.075	$5.6 \times 10^{13}$
290	0.157	$5.4 \times 10^{14}$

Table 5.1 Laser intensity at which  $\mathcal{E}^2 = 4\omega_L^3$  for various wavelengths.

Resonant enhancement is not expected for  $\mathcal{E}^2 \gg 4\omega_L^3$ .

A set of experiments which used a Q-switched Nd:glass laser (1  $\mu\text{m}$  wavelength) have observed a 10-photon resonant enhancement of 11-photon ionization in xenon.<sup>88</sup> These experiments were performed with a 1-ns pulse length having a maximum intensity of  $3 \times 10^{12} \text{ W/cm}^2$  so resonant enhancement was possible since  $\mathcal{E}^2 < 4\omega_L^3$  in this case. The long pulse length and the multi-mode nature of the light made it possible to detect ions at this low intensity. Additionally, no resonant enhancement was seen for circularly polarized light.

Another way of looking at the frequency dependence of resonant ionization is to consider the Breit-Wigner formula (Eqn. 1.11). For a large ionization rate from the resonant level  $\gamma_2$  is large, and Eqn. 1.11 reduces to  $W = \Omega^2/\gamma_2$ . The value of  $\gamma_2$  can be estimated in the quasiclassical approximation as<sup>89</sup>

$$\gamma_2 \approx 2\pi \left[ \frac{C\mathcal{E}}{\omega_L^{5/3} n^{3/2}} \right]^2, \quad (5.1)$$

where  $n$  is the principle quantum number and  $C$  is a constant of order 0.1. This implies that the resonant ionization rate  $W$  is proportional to  $\omega^{10/3}$ . Additionally, as  $\omega$  increases, the Rabi frequency ( $\Omega$ ) increases as the order of the process decreases. This means that the rate  $W$  actually increases with  $\omega$  faster than  $\omega^{10/3}$ .

Resonant enhancement may break down when the width of the resonant level is equal to the level spacing. For large  $n$  the level spacing is proportional to  $n^{-3}$ . When the width of the level is determined by  $\gamma_2$  (*i.e.* when  $\gamma_2$  is large), resonant enhancement should not occur when  $\gamma_2 \gg n^{-3}$  or equivalently

$$\mathcal{E}^2 \gg \frac{\omega_L^{10/3}}{2\pi C^2}, \quad (5.2)$$

which has nearly the same dependence on  $\omega$  as was determined from the ponderomotive potential argument.

### V.B. Pulse Duration and Bandwidth Experiments

The threshold intensities for our 1 ps data are higher than those seen by the Saclay group <sup>14</sup> at 50 ps (by approximately a factor of 10 in xenon). The agreement improves for the lighter noble gases. Some decrease in the number of ions is expected since the total probability is equal to the product of the ionization rate and the pulse length. This suggests that a 50 ps pulse should produce about 50 times the number of ions that are produced by a 1 ps pulse at the same intensity. Since the slope of the ion production curves is very steep, a difference of 50 should not translate into a large intensity shift. In fact, for an  $I^N$  dependence where  $N = 11$  the expected shift is a factor of 1.4 and for  $N = 6$  the expected shift is 1.7. So the observed shift is much larger than can be accounted for by pulse length arguments.

There were actually two differences between the 1 ps experiments done at LLE and the 50 ps experiments done at Saclay. The pulse length was different but the bandwidth of the light was also narrower in the Saclay experiments. In an attempt to understand this suppression of the ionization, we performed experiments using 55 ps laser pulses. With our CPA laser system it is possible to vary the pulse length and bandwidth independently so we were able to do experiments with 55 ps laser pulses which were either bandwidth limited at  $\Delta\lambda \approx 0.3 \text{ \AA}$  or far from bandwidth limited at  $\Delta\lambda \approx 7 \text{ \AA}$ . The 7  $\text{\AA}$  experiments actually used a pulse which was frequency chirped in time. This may be significant since the atoms do not simultaneously see the full 7  $\text{\AA}$  of bandwidth, but are exposed to small portions of it over a 55 ps time period.

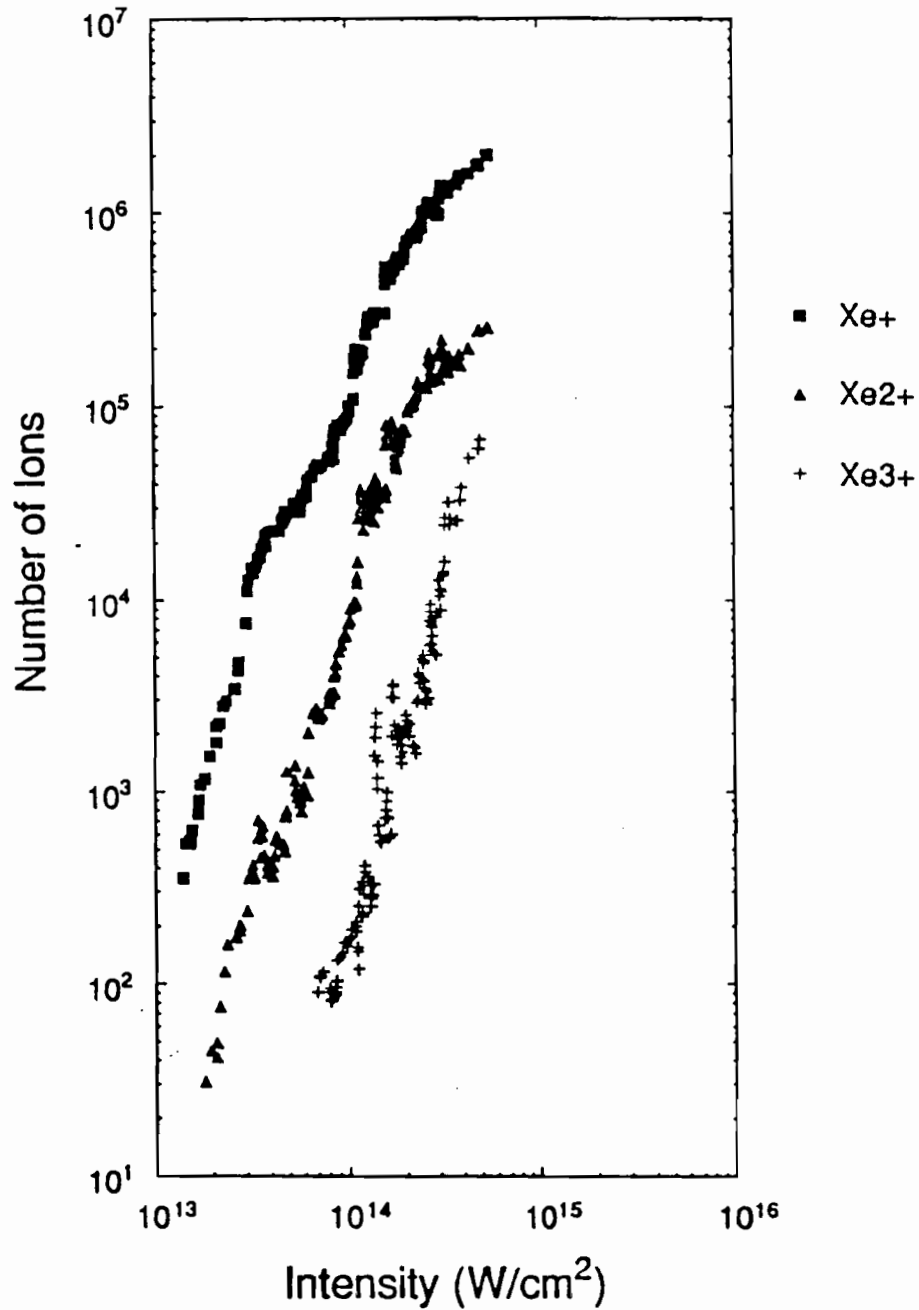


Fig. 5.3 Xenon ion production for 55 ps laser pulse with 0.3 Å bandwidth.

The results of these experiments are shown in Figs. 5.3 and 5.4. If the two figures are overlaid the ion curves overlap to within about 10% (hold the two pages up to the light to see this). We currently have no explanation for the presence of the kink

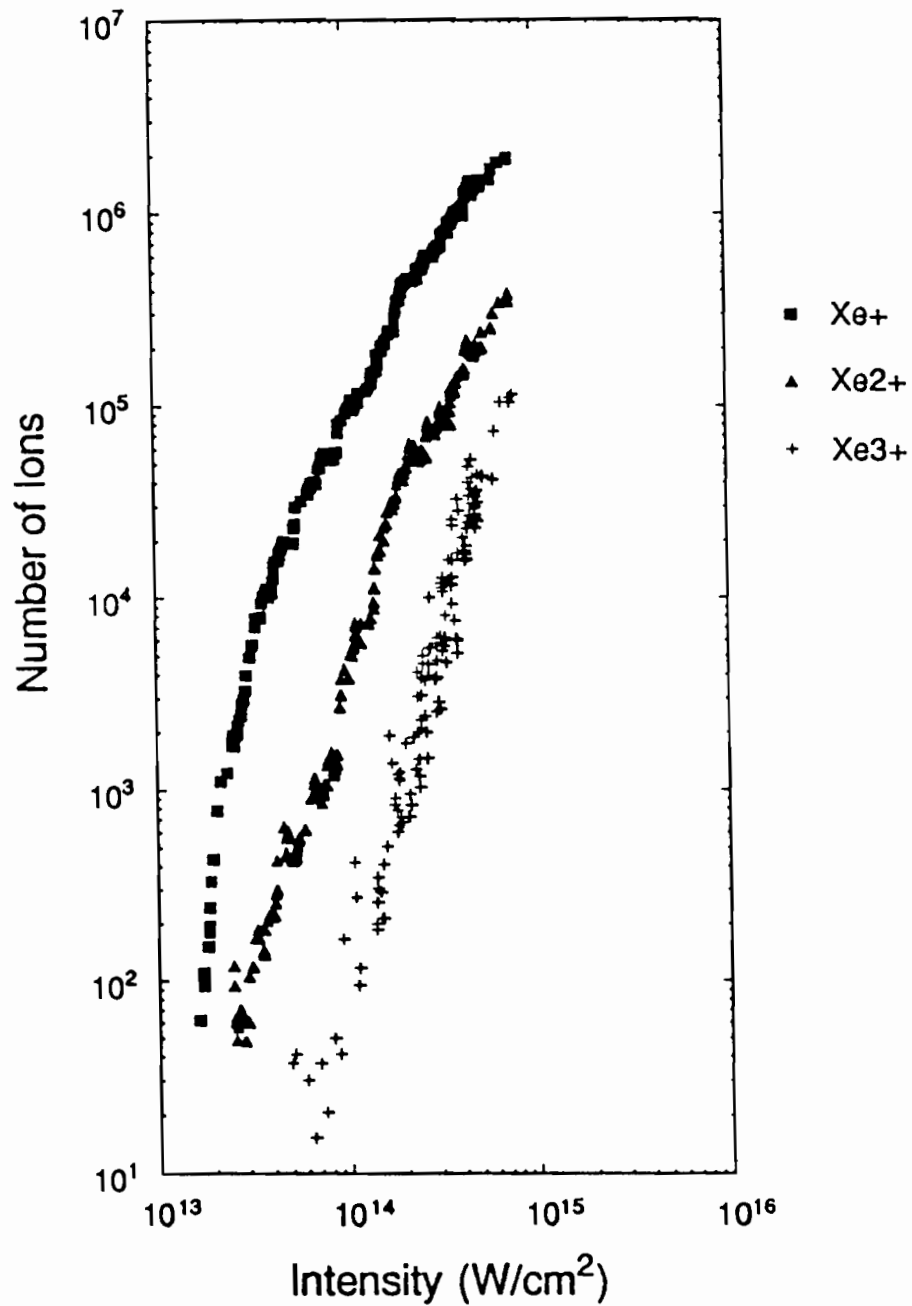


Fig. 5.4 Xenon ion production for 55 ps laser pulse with 7 Å bandwidth.

in the first charge state of Fig. 5.3 (bandwidth limited case). The close agreement between the two cases suggests that the apparent suppression of ionization for the 1 ps data is not due to the increased bandwidth which is associated with the 1 ps pulse.

Figure 5.5 reproduces the data from Fig. 5.3 with an additional 2 decades in ion number. The additional data with low ion number was taken with a 60 cm focal length lens rather than the original 20 cm lens. A longer focal length lens produces a larger focal spot and consequently a larger focal volume (recall Eqn. 4.2). The focal diameter increases linearly with the  $f\#$  of the lens so an increase of three in focal length results in a volume increase of 81. The ion number in Fig. 5.5 drops below one since it is scaled to the volume associated with the shorter focal length lens.

The data shown in Fig. 5.5 suggests that there may be a transition from the multiphoton regime to the tunneling regime. At about 400 ions the slopes of the ion curves decrease and the spacing between the charge states increases. The kink in the second charge state could be attributed to a transition from a direct ionization process to a sequential process but this explanation cannot be applied to the first charge state. The 700 ion level in this chapter corresponds to a level of about 1 ion for the 1 ps data shown in chapter three. There are three factors which helped to extend the curves to lower ion number: 1) the transmission efficiency of the spectrometer was improved by about a factor of ten by using more transmissive wire grids as described in chapter two, 2) the focal spot was enlarged somewhat due to the increase in f-number which results from the smaller beam diameter associated with double-passing the compression gratings, and 3) the data in chapter three is referenced to  $5 \times 10^{-6}$  Torr and the data in chapter five is referenced to  $5 \times 10^{-5}$  Torr. The 1 ps data in chapters three and five are in good agreement when these three things are accounted for.

A comparison between the first charge state of this data and the 50 ps Saclay data can be made. We do not know the backfill pressure, focal volume, or spectrometer efficiency of the Saclay data so in order to make a comparison we must

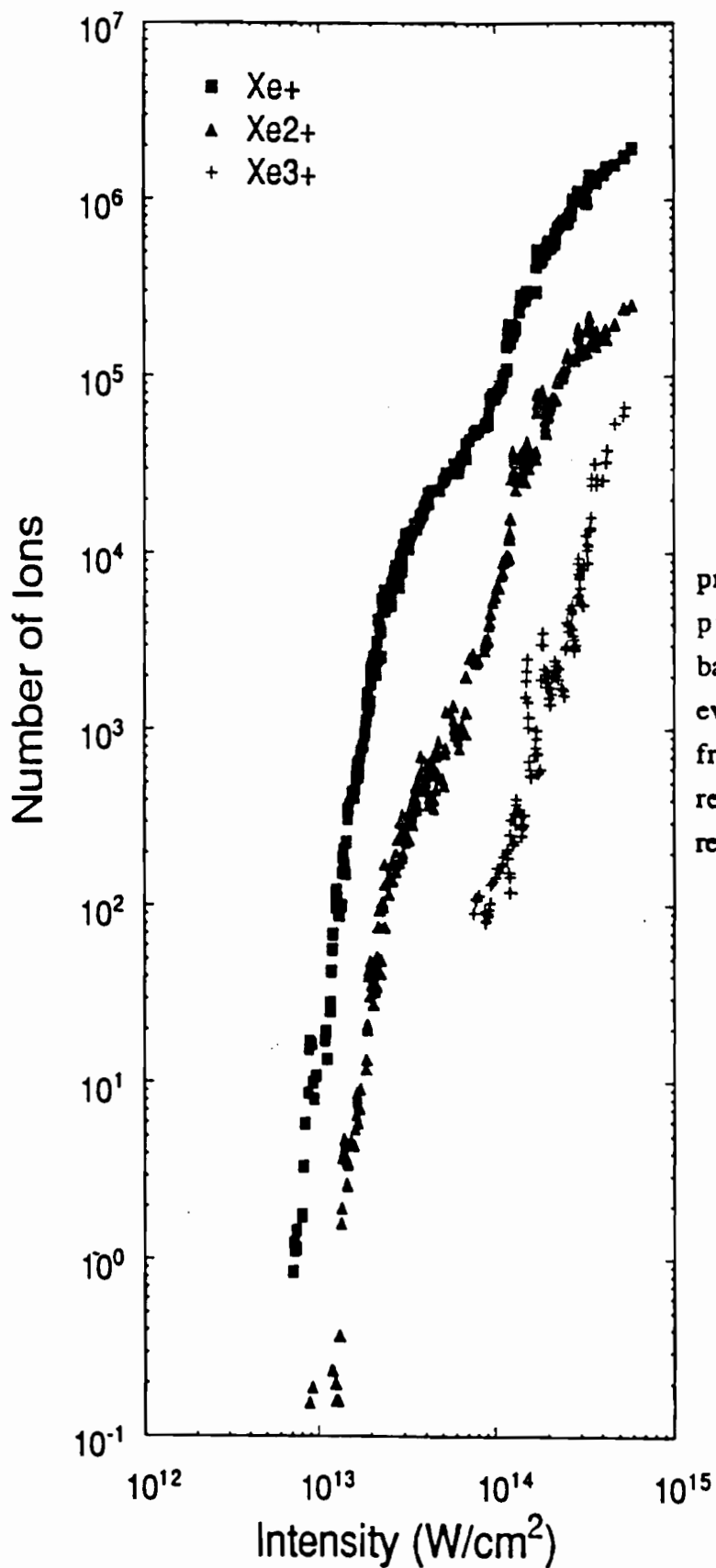


Fig. 5.5 Xenon ion production for a 55 ps pulse with 0.3 Å bandwidth. There is some evidence for a transition from the multiphoton regime to the tunneling regime.

line up the saturation levels. Since our data has a kink in it we have two possibilities for the saturation level. Figures 5.6 and 5.7 show the two possible alignments. If the lower saturation is used, the two sets of data agree to within a factor of about 1.3. If the higher saturation is used, the two sets of data are separated by about a factor of 10 at the  $10^5$  ion level. This accounts for the apparent discrepancy which was mentioned earlier. The origin of the kink should be investigated further to determine if it is an artifact of the experimental apparatus or if it is due to a change in the physical process on an atomic level.

A comparison between our 1.9 ps data and our 55 ps data can be made [see Fig. 5.8]. The lower portion of the curves are separated by a factor of about 3 in intensity. This shift can not be explained totally by the difference in pulse length which can account for a factor of about 1.7. The slopes of the two curves differ. The lower portion of the 55 ps data has a slope value near 11 which is in agreement with LOPT. Both the 1.9 ps data and the upper portion of the 55 ps data have a slope closer to 6. The significance of this difference in slope is not yet fully understood. A fairly large relative uncertainty remains between the intensities for the two pulse lengths (maybe as much as a factor of two). This is mainly due to uncertainties in the focal spot area measurements since the different pulse lengths need to use different conversion curves to translate optical density on the film into incident laser intensity.

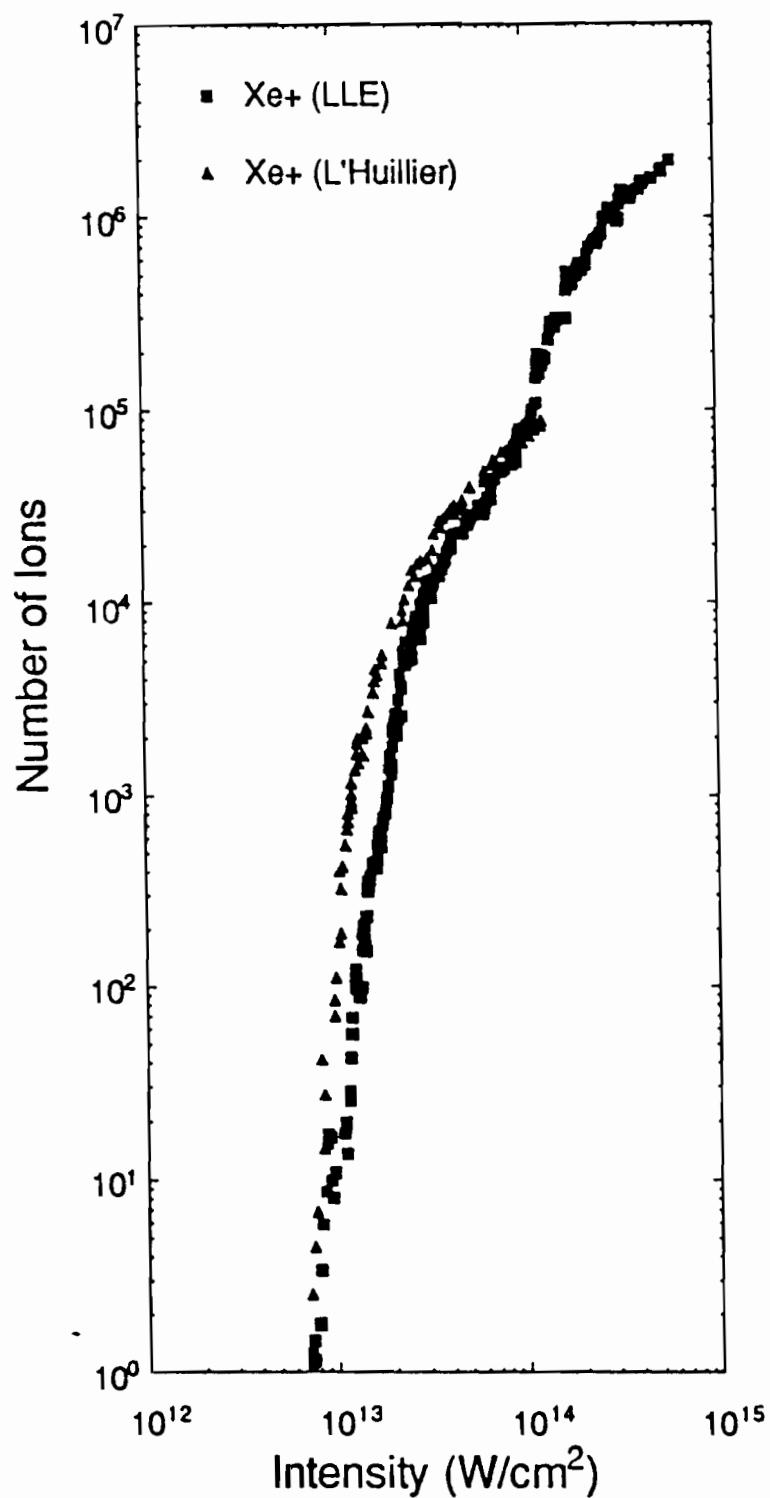


Fig. 5.6 Comparison between the 55 ps data obtained at LLE and the 50 ps data obtained by L'Huillier. L'Huillier's data is aligned with the lower saturation level.

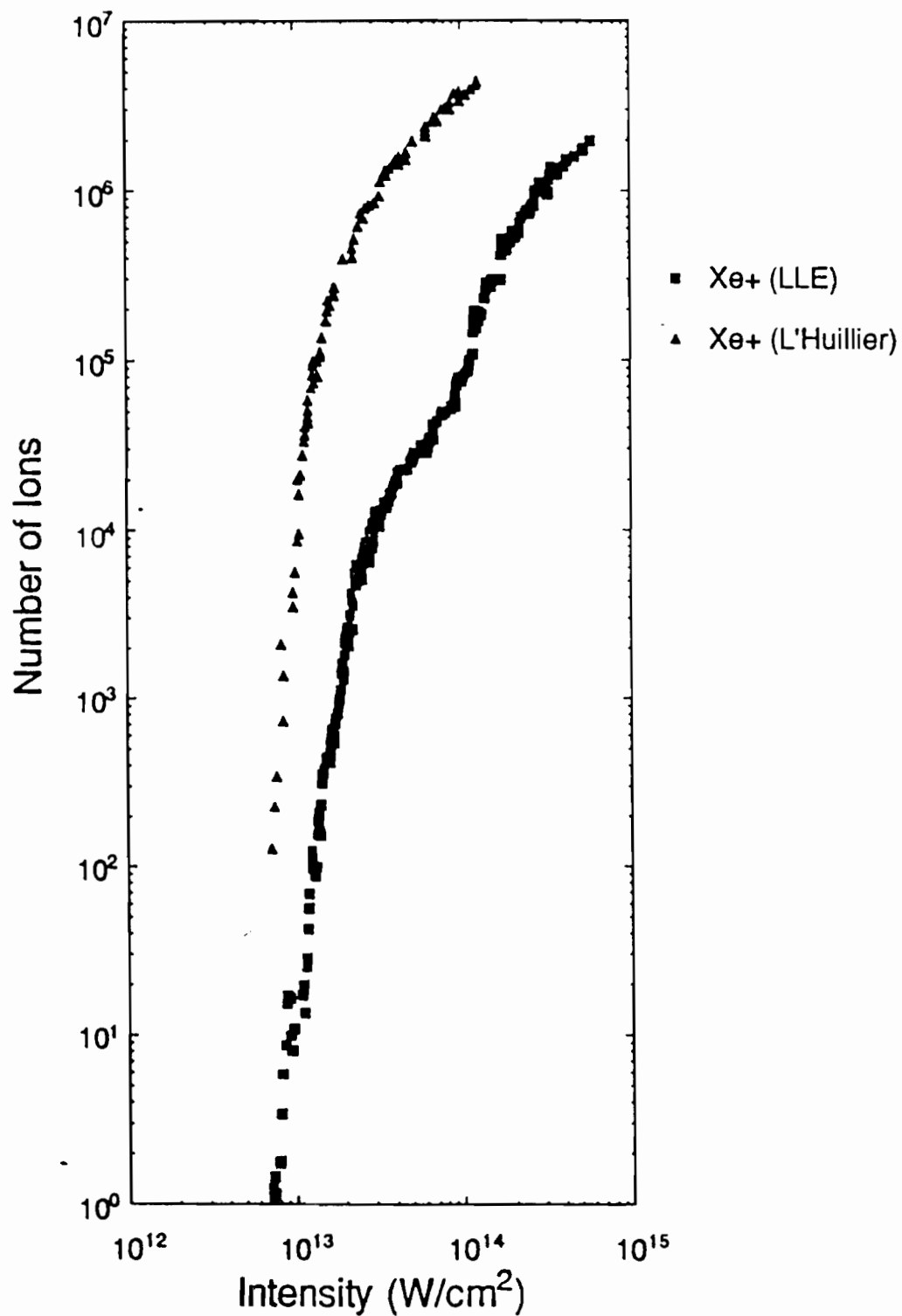


Fig. 5.7 Comparison between the 55 ps data obtained at LLE and the 50 ps data obtained by L'Huillier. L'Huillier's data is aligned with the upper saturation level.

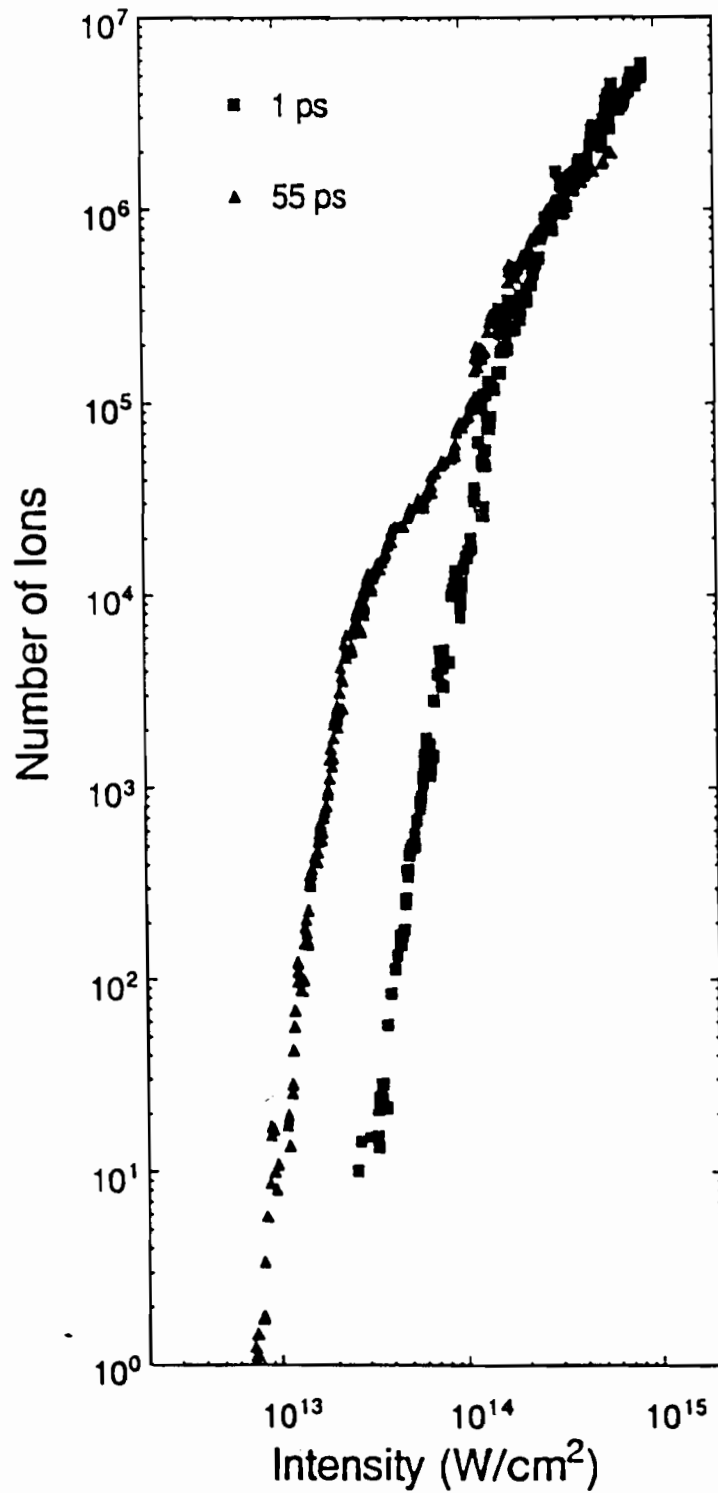


Fig. 5.8 Comparison of  $\text{Xe}^+$  ion production for 1.9 ps and 55 ps laser pulses at  $1.053 \mu\text{m}$  wavelength.

## V.C. Second Harmonic Generation Experiments

Experiments to study harmonic generation of the laser have been performed (see Appendix E for experimental procedure). These include the observation of second harmonic production in krypton gas. This is relevant to the discussion of ion production since it provides an independent method of testing the BSI model. Electron densities which have been calculated with the BSI model are used to compare theoretical predictions to experimentally measured values of the conversion efficiency and the spectral shift of the second harmonic. Both quantities are found to have satisfactory agreement.

In the dipole approximation second harmonic production is a forbidden process in an isotropic medium. It is possible, however, to create second harmonic light by introducing a static electric field to the focal region.<sup>90,91</sup> Second harmonic generation is only seen at intensities higher than that required to ionize the gas, and when the gas is ionized the electrons are ponderomotively accelerated away from the beam axis. The ions are heavier so they do not move much. This results in a charge separation which creates a radial electric field. This electric field can interact with the laser to produce second harmonic by a four-wave mixing process [see Fig. 5.9].

The radial electric field which is created at the laser focus is actually not a static field, but it is oscillatory with a frequency equal to the plasma frequency. This has been confirmed experimentally by measuring the spectrum of the second harmonic signal as a function of target gas pressure. The plasma frequency depends on the electron density as  $\omega_p \propto n_e^{1/2}$  and the central frequency of the second harmonic is observed to shift approximately as  $n_e^{1/2}$ , where  $n_e$  is determined using the BSI model [see Fig. 5.10].

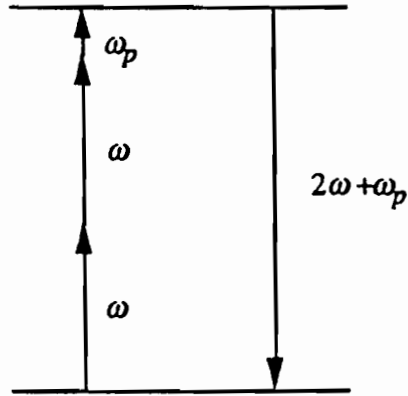


Fig. 5.9 Four-wave mixing between the laser and another electric field with frequency  $\omega_p$ . If the field is static then  $\omega_p = 0$  and second harmonic generation results.

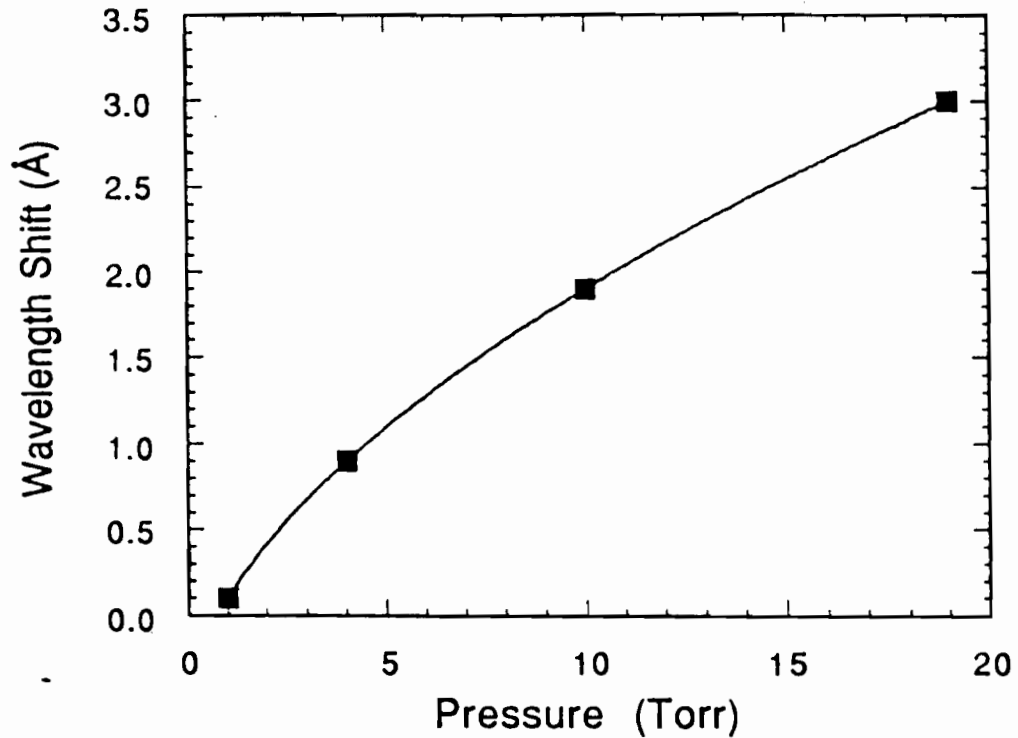


Fig. 5.10 Second harmonic wavelength shift versus gas pressure (electron density is proportional to pressure in this range). The best fit line is  $\Delta\lambda = -0.55 + 0.65 \times P^{0.58}$ .

The experimental conversion efficiency for second harmonic (using  $I = 3 \times 10^{14} \text{ W/cm}^2$ ) was measured as  $\eta_2 = 1 \times 10^{-14}$  with a factor of three uncertainty.<sup>92</sup> The magnitude of the static electric field can be estimated using the BSI model to determine the degree of ionization and using plasma equations<sup>91</sup> to determine the electric field which is set up due to charge separation. At an intensity of  $3 \times 10^{14} \text{ W/cm}^2$  the calculated value of the static electric field is  $\mathcal{E}_s = 3 \times 10^4 \text{ V/cm}$ . This is used to calculate the expected theoretical conversion efficiency<sup>91</sup>

$$\eta_2 = 9\pi^3 k_1^4 (\chi^{(3)})^2 I \mathcal{E}_s^2 \omega_0^4 / c, \quad (5.3)$$

where  $k_1$  is the fundamental wave number and  $\chi^{(3)}$  is the nonlinear susceptibility given by  $\chi^{(3)} = N\gamma$ , where  $N$  is the ion density ( $\approx 5 \times 10^{16} \text{ cm}^{-3}$ ) and  $\gamma = 3.8 \times 10^{-37} \text{ esu}$ .<sup>93</sup> We find a theoretical value of  $\eta_2 = 3 \times 10^{-13}$ , which is within a factor of three of the experimental result.

## CHAPTER SIX

### CLOSING REMARKS

#### VI.A. Summary

The interaction of noble gas atoms with high-intensity, 1-ps laser pulses at 1.053- $\mu\text{m}$  wavelength has been discussed. Data which represent the first survey of noble gas ionization at this wavelength with intensities up to  $5 \times 10^{16}$  W/cm<sup>2</sup> is presented. It is found that ionization of noble gases with this laser occurs in the tunneling or barrier suppression regime rather than the multiphoton regime and a species dependent threshold intensity is observed. This species dependence is best described by either a Coulomb barrier-suppression model, or a species-dependent tunneling ionization model. Other models which do not include species dependence do not accurately predict the spacing between charge states. Two Thomas-Fermi models which include a species dependence are not in agreement with each other. One describes the threshold intensities fairly well and the other does not agree with the lower charge states.

Additional experiments suggest that the ionization process is non-resonant in contrast to results at shorter wavelengths which suggest that high-intensity ionization is resonantly enhanced due to Stark shifting of bound levels.<sup>43-47</sup> Evidence for a non-resonant process can be seen in a comparison of ionization by linearly or circularly polarized light. The observed threshold intensity for ionization by linearly polarized light is approximately a factor of two less than for circularly polarized light. Ionization with circularly polarized light is not expected to be resonantly enhanced since dipole selection rules make most resonant states inaccessible. If the ionization process for

linear polarization were resonantly enhanced the difference in threshold intensities would be more than a factor of two. Two criteria are suggested to distinguish resonant from non-resonant ionization. Both place our experiments in the non-resonant regime and leave the shorter wavelength experiments in the resonant regime.

Variable bandwidth experiments were performed to investigate the effects on ionization. It was found that non-bandwidth limited, chirped pulses produced ion curves which were nearly identical to those produced by bandwidth limited pulses of the same duration. A comparison between our 55 ps bandwidth limited data and that obtained by L'Huillier *et al.*<sup>14</sup> showed that the discrepancy in threshold intensities which we had originally observed can be attributed to the two saturation levels which are seen in our data. The agreement between the results of the two experimental groups can be either good or bad depending on which saturation level is used to align the two sets of data.

A comparison between our 1.9 ps data and 55 ps data shows that the difference in thresholds for the two cases can not be attributed entirely to the difference in pulse length. The slopes of the curves suggest that the longer pulse length data agrees with LOPT better than the short pulse data.

Second harmonic production was seen in krypton and the threshold for harmonic production is consistent with the threshold for ion production. The spectral shift due to the plasma frequency is in agreement with calculated electron densities using the BSI model and the harmonic conversion efficiency is within order of magnitude agreement with theoretical predictions.

## VI.B. Future experiments

Higher damage threshold compression gratings are currently being installed in the laser system which will allow experiments to be done at intensities above  $10^{18}$  W/cm<sup>2</sup>. A high intensity pressure scan of all the noble gases can then be performed using the improved techniques of chapter five at both 1 ps and 55 ps pulse lengths. This should answer the question of whether there is a transition from MPI to tunneling ionization.

High resolution electron spectroscopy should be performed to investigate whether resonant peaks can be seen in the electron spectra. This would either confirm or dispute the current hypothesis that the ionization process for 1- $\mu$ m light in this intensity regime is non-resonant. Electron spectra will provide an additional test for various theoretical models since features such as the angular dependence of electron emission can be tested.

Measurement of the laser intensity using ponderomotively accelerated electrons should be repeated with the new laser setup. Both 1 ps and 55 ps pulses should be used. The longer pulse length will allow the electrons to convert their entire ponderomotive potential into directed kinetic energy thereby reducing the uncertainties associated with this measurement technique. This independent measurement of the laser intensity will increase our confidence level in the current measurements.

## APPENDICES

### A. Pulse Fluctuation Measurement

The IR light energy can be expressed as the time integral of the incident power

$$E_{ir} = \int_{-\infty}^{\infty} dt P_{ir}(t). \quad (\text{A.1})$$

We can write  $P_{ir}(t)$  as the product of the peak power and a time dependent function:

$P_{ir}(t) = P_{ir,o} f(t)$  so

$$E_{ir} = P_{ir,o} \int_{-\infty}^{\infty} dt f(t). \quad (\text{A.2})$$

The power of the frequency-doubled (green) signal is proportional to the fundamental power squared so

$$E_g = \int_{-\infty}^{\infty} dt P_g(t) = A \int_{-\infty}^{\infty} dt P_{ir}^2(t) \quad (\text{A.3})$$

where  $A$  is a constant that depends on the conversion efficiency of the crystal. Now we can write  $E_g$  as

$$\begin{aligned} E_g &= A \int_{-\infty}^{\infty} dt P_{ir,o}^2 f^2(t) \\ &= A P_{ir,o}^2 \int_{-\infty}^{\infty} dt f^2(t). \end{aligned} \quad (\text{A.4})$$

For realistic laser pulses, the time dependence in  $f(t)$  always appears as the ratio  $t/\tau_{ir}$  so we can introduce a change of variables:  $u \equiv t/\tau_{ir}$  where  $\tau_{ir}$  is a measure of the pulse width of each laser shot. Substituting  $u$  into Eqns. (A.2) and (A.4) yields

$$E_{ir} = P_{ir,o} \tau_{ir} \int_{-\infty}^{\infty} du f(u) \quad (\text{A.5})$$

$$E_s = A P_{ir,o}^2 \tau_{ir} \int_{-\infty}^{\infty} du f^2(u). \quad (\text{A.6})$$

The laser pulse width ( $\tau_{ir}$ ) varies from shot to shot, but since  $t$  always appears in  $f(t)$  as  $t/\tau_{ir}$  the pulse shape  $f(u)$  does not vary. This means that the shot-to-shot fluctuations have been removed from the integrals in Eqns. (A.5) and (A.6) and they can be replaced by constants so

$$E_{ir} = B P_{ir,o} \tau_{ir} \quad (\text{A.7})$$

$$\begin{aligned} E_s &= C A P_{ir,o}^2 \tau_{ir} \\ &= \frac{CA}{B} E_{ir} P_{ir,o} \\ &= \frac{CA}{B^2} \frac{E_{ir}^2}{\tau_{ir}} \end{aligned} \quad (\text{A.8})$$

Solving for  $\tau_{ir}$  we get Eqn. (2.5)

$$\tau_{ir} = \frac{CA}{B^2} \frac{E_{ir}^2}{E_s} \quad (\text{A.9})$$

## B. Time of Flight Calculation

The expression for the flight time of an ion in a TOF spectrometer is derived here. Relativistic effects are ignored since the maximum energy of an ion will be of magnitude 10 keV.

The force on an ion in an electric field is (see Fig. B.1)

$$F = ma = q\mathcal{E} = qV_1/d \quad (\text{B.1})$$

The time required for an ion to reach the drift tube is obtained from  $x = at^2/2$ .

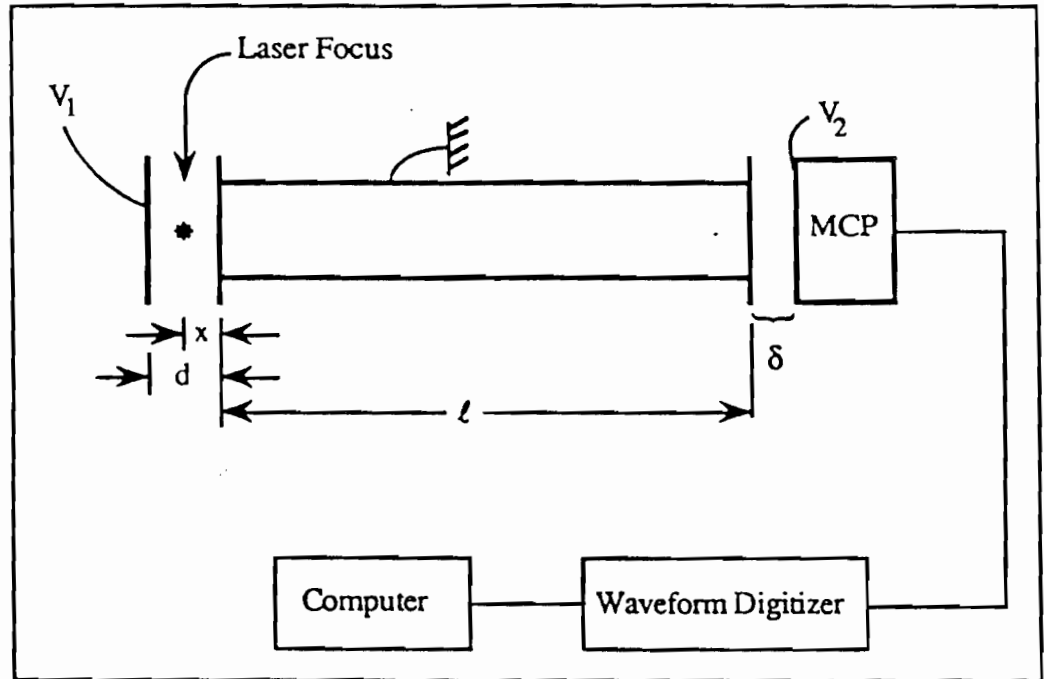


Fig. B.1 Drawing of the ion time-of-flight spectrometer.

Using the expression for the acceleration we obtain an acceleration time of

$$t_{A_1} = \sqrt{\frac{2mx d}{qV_1}} \quad (\text{B.2})$$

At this point the ion will drift with a constant velocity in the field free drift tube. Its *Kinetic Energy* =  $qEx = qV_1x/d = mv^2/2$ .

Solving for  $v$  yields

$$v = \sqrt{\frac{2qV_1x}{md}} \quad (\text{B.3})$$

The drift time is then

$$t_D = \frac{\ell}{v} = \ell \sqrt{\frac{md}{2qV_1x}} \quad (\text{B.4})$$

In calculating the time for the second acceleration we should not neglect the initial velocity so the time must be found from the quadratic equation

$$\delta = at^2/2 + vt.$$

Only one of the roots gives a positive time so the solution is

$$t_{A_2} = \sqrt{\frac{m}{q}} \left[ \frac{\delta}{V_2} \left( \sqrt{\frac{2V_1x}{d} + 2V_2} - \sqrt{\frac{2V_1x}{d}} \right) \right] \quad (\text{B.5})$$

Adding up the three contributions to the total drift time we get

$$\begin{aligned} t_T &= t_{A_1} + t_D + t_{A_2} \\ &= \sqrt{\frac{m}{q}} f(x, d, \ell, \delta, V_1, V_2) \end{aligned} \quad (\text{B.6})$$

For the hydrogen ion, the ratio  $m/q = 1$  which means the geometrical factor  $f$  is simply the time of flight of a hydrogen ion. Since it is very difficult to remove all the hydrogen

from a vacuum tank (much of it comes from dissociated water molecules) there is always a hydrogen peak present in our spectra. This is actually quite convenient since it can be used for calibration purposes [see Fig. 2.7].

### C. Integration of Coupled Rate Equations

The following program is used to solve equation (4.1). Ionization rates are assumed to be read in from an external file. The total number of particles is conserved to account for saturation effects. The program uses about 1 minute of CPU time on a Vax 6000-410.

```
*****
* THIS PROGRAM WILL CALCULATE THE NUMBER OF IONS      *
* PRODUCED FROM A LASER PULSE. THE CALCULATION        *
* INCLUDES SATURATION EFFECTS.                       *
* THE IONIZATION RATES ARE OBTAINED FROM PREVIOUSLY  *
* CALCULATED RATE TABLES. THE TABLES ARE PRODUCED *
* BY EITHER 'AMMRATE' OR 'KFRRATE'                   *
*****

REAL ATOM(0:200,0:54),SHELL(0:54),I0(0:200),EION(54),MOVE(54)
REAL R0,T0,INTEN,TRAN(0:100,54),TRANS,DT,A5,A6,R1,R,T
REAL DENS,Z,DI,SUM,NSTAR,VOL
REAL CSHEL1,CSHEL2,FRACTION
INTEGER L(54),M,ICH,ZLOOP,DZ,RLOOP,DR,ILOOP,KLOOP
CHARACTER*50 TITLE,FILENAME

DATA PI /3.14159265/
* A5 = 2*LAMBDA*LN(2)/PI FOR LAMBDA=1.053
* A6 = -4*LN(2)
DATA A6 /-2.772589/
***** 1053 NM *****
DATA A5 /0.46466/
```

- \* R0 = FWHM Gaussian
- \* T0 = FWHM Gaussian
- \* DT = Time step size. About 15 or 20 cycles is good usually
- \* where  $2\pi/\Omega = \text{LAMBDA}/C = 3.5E-3 = \text{ONE CYCLE}$
- \* DI = Intensity Step Factor

\*\*\*\*\* 1053 NM \*\*\*\*\*

DATA R0 /22.9/, T0 /1.0/, DT /70.E-3/

DATA ATOM /11055\*0./, TRAN /5454\*0./

\*\*\*\*\* DENS = GAS DENSITY IN MICRONS\*\*<sup>-3</sup> \*\*\*\*\*

\*\*\*\*\* = Pressure in Torr  $\times 3.5E4$  \*\*\*\*\*

DENS = (1.5E-5)\*(3.5E4)

\*\*\*\*\*

WRITE(6,\*) 'INPUT FILENAME FOR RATE TABLE'

READ(6,5) FILENAME

OPEN(UNIT=64,FILE=FILENAME,STATUS='OLD')

READ(64,5) TITLE

\*\* First line of file identifies the atom, the theoretical model, and laser characteristics \*\*

5 FORMAT(A50)

WRITE(70,\*) TITLE

J = 0

6 READ(64,\*,END=7) (TRAN(J,I) , I=1,54),I0(J)

J = J + 1

GOTO 6

```

7  CONTINUE
  CLOSE (UNIT=64)
  DO 70 I = 0, J-1
    IF (I .LT. J-1) DI = I0(I+1)/I0(I)
    KLOOP = NINT(1.8/LOG10(DI))
    DO 40 K = 0,-KLOOP,-1
      FRACTION = DI**FLOAT(K)
      VOL = VOLUME(FRACTION/DI,R0,A5) - VOLUME(FRACTION,R0,A5)
      SHELL(0) = VOL*DENS

      DO 10 I2 = 1, 54
        SHELL(I2) = 0.
10  CONTINUE

      T = -20.*T0
      DO WHILE (T .LT. 20.*T0)
C      INTEN = I0(I)*FRACTION*((1.+DI)/(2.*DI))/(1.+4.*(T/T0)**2.)
      INTEN = I0(I)*FRACTION*((1.+DI)/(2.*DI))*EXP(A6*(T/T0)**2)
      IF (INTEN .LT. I0(0)) GOTO 23  !exit loop if intensity is low ****
      I2 = 1
      DO WHILE (.TRUE.)
        I4 = I
        DO WHILE (INTEN .LT. I0(I4))
          I4 = I4 - 1
        END DO

```

\*\*\*\*\*

\* Linear interpolation between values in the rate table. \*

\*\*\*\*\*

```

      TRANS = TRAN(I4,I2)+
+      (TRAN(I4+1,I2)-TRAN(I4,I2))*(INTEN-I0(I4))/(I0(I4+1)-I0(I4))
      MOVE(I2) =(1.-EXP(-TRANS*DT*1.E-12))*SHELL(I2-1)
      I2 = I2 + 1      !Increment charge state *****

```

\*\*\*\*\* exit loop when charge state is 54 \*\*\*\*\*

```

      IF (I2 .GT. 54) GOTO 15

```

\*\*\*\*\* exit loop when trans. prob. < 1.e-5 \*\*\*\*\*

\*\*\*\*\* note tran\*dt\*1.e-12 ≈ transition probability \*\*\*\*\*

```

      IF (TRANS*DT .LT. 1.E5) GOTO15
      END DO
15      SUM1 = 0.
      DO 20 I3 = 1 , I2 - 1
          SHELL(I3) = SHELL(I3) + MOVE(I3)
          SHELL(I3-1) = SHELL(I3-1) - MOVE(I3)
          SUM1 = SUM1 + MOVE(I3)
20      CONTINUE
      IF (SUM1 .LT. .02 .AND. T .GT. .1*T0) GOTO 25
23      T = T + DT
      END DO
25      SUM2 = 0.
      ATOM(I,0) = ATOM(I,0) + SHELL(0)
      DO 30 I3 = 1,54

```

```

        ATOM(I,I3) = ATOM(I,I3) + SHELL(I3)
        SUM2 = SUM2 + SHELL(I3)
30      CONTINUE
        IF ( SUM2 .LT. .1 ) GOTO 50
40      CONTINUE
***** Main output goes to unit 70 *****
50      WRITE(70,*) (ATOM(I,I5), I5=0,54),I0(I)
70      CONTINUE
        STOP
        END

```

```

REAL FUNCTION VOLUME(A,R0,A5)

```

```

***** A function to calculate the focal volume of the laser. *****

```

```

REAL A,R0,A5,ZR,ZM

```

```

***** B1 = PI/(2*LN(2)) *****

```

```

***** RS = RADIUS OF HOLE IN SPECTROMETER (microns) *****

```

```

DATA B1 /2.26618/, RS /2500./

```

```

*   IF (A .GT. 1. .OR. A .LT. 0.) WRITE(6,*) ' A OUT OF BOUNDS'

```

```

***** ZR = RALEIGH RANGE *****

```

```

***** ZM = MAX Z FOR R=0 *****

```

```

ZR = (R0**2.)/A5

```

```

ZM = ZR*SQRT((1.-A)/A)

```

```

***** The following stuff taking into account the size *****
***** of the hole in the spectrometer does not affect *****
***** the results for ion numbers below 1.e7 *****

*   IF (ZM .GT. RS) THEN
*C   B10 = 1. + (RS/ZR)**2.
*C   ZM = SQRT(RS**2.-R0**2.*B10*LOG(A*B10)/(8.*LOG(2.)))
*   ZM = RS           !close enough for science.
*   B2 = ZM*R0**2.
*   B3 = ZM/ZR
*   B7 = 1. + B3**2.
*   B8 = 1. + (B3**2.)/3.
***** B9 = 0. WHEN ZM .LT. RS SINCE B7=1/A THEN *****
*   B9 = B2*B8*(LOG(A)+LOG(B7))
*   ELSE
      B2 = ZM*R0**2.
      B3 = ZM/ZR
*   B9 = 0.
*   ENDIF
      B4 = 4.*B2/3.
      B5 = (2./9.)*B2*B3**2.
      B6 = (4./3.)*ZR*(R0**2.)*ATAN(B3)
*   VOLUME = B1*(B4+B5-B6-B9)
      VOLUME = B1*(B4+B5-B6)
      RETURN
      END

```

#### D. Iso-Intensity Volume Calculation

The volume of a laser focus can be calculated using Gaussian beam propagation equations which predict a beam intensity dependence of<sup>94</sup>

$$I = I_o \left( \frac{w_o}{w_l} \right)^2 \exp \left( -2 \left( \frac{w}{w_l} \right)^2 \right) \quad (\text{D.1})$$

where

$$w_l = w_o \sqrt{1 + \frac{z^2}{z_R^2}}, \quad (\text{D.2})$$

and  $w_o$  is the  $1/e^2$  radius of the intensity profile at the beam waist (*i.e.* at  $z = 0$ ), and  $z_R = \pi w_o^2 / \lambda =$  the Rayleigh range of the focus. Let us define  $A$  as some fraction of the maximum intensity  $A = I/I_o$  and solve for  $z(A)$  along the beam axis (*i.e.*  $w=0$ ). Combining Eqns. (D.1) and (D.2) with  $w=0$  we find

$$z^2 \Big|_{w=0} = z_R^2 \left( \frac{1-A}{A} \right) \equiv C^2. \quad (\text{D.3})$$

For a given value of  $A$ , Eqn. (D.1) can be solved for  $w$  with the result

$$w(A) = w_l \sqrt{\frac{1}{2} \ln \left( \frac{w_o^2}{A w_l^2} \right)}. \quad (\text{D.4})$$

Now that we have the integration limits we can find the focal volume which has an intensity greater than  $A I_o$

$$Vol = \int_{-C}^C dz \int_0^{w(A)} dw \int_0^{2\pi} w d\phi \quad (D.5)$$

$$Vol = \pi \int_0^C dz w_l^2 \ln\left(\frac{w_o^2}{A w_l^2}\right) \quad (D.6)$$

$$= \pi \left[ \ln\left(\frac{w_o^2}{A}\right) \int_0^C dz w_l^2 - \int_0^C dz w_l^2 \ln(w_l^2) \right] \quad (D.7)$$

Plugging in the expression (D.2) for  $w_l$  and integrating we get

$$\begin{aligned} Vol = \pi \left[ \ln\left(\frac{w_o^2}{A}\right) w_o^2 z_R \left(\frac{C}{z_R} + \frac{C^3}{3z_R^3}\right) - z_R w_o^2 \ln(w_o^2) \left(\frac{C}{z_R} + \frac{C^3}{3z_R^3}\right) - \right. \\ \left. - z_R w_o^2 \left(\frac{C}{z_R} \ln\left(1 + \frac{C^2}{z_R^2}\right) - \frac{2C}{z_R} + 2 \tan^{-1}\left(\frac{C}{z_R}\right)\right) - \right. \\ \left. - z_R w_o^2 \frac{1}{3} \left(\frac{C^3}{z_R^3} \ln\left(1 + \frac{C^2}{z_R^2}\right) - \frac{2C^3}{3z_R^3} + \frac{2C}{z_R} - 2 \tan^{-1}\left(\frac{C}{z_R}\right)\right) \right] \quad (D.8) \end{aligned}$$

Canceling terms and defining  $c \equiv C/z_R = (1-A)/A = (I_o - I)/I$

$$Vol = \pi z_R w_o^2 \left[ \frac{4c}{3} + \frac{2c^3}{9} - \frac{4}{3} \tan^{-1}(c) \right]. \quad (D.9)$$

This is the volume of the focus which has an intensity greater than the fraction  $A$ . To find the volume of a shell between two intensities, we must subtract the volume with

fraction  $A_2$  from the volume with fraction  $A_1$ . The volume of a shell is then

$$Volume = \pi z_R w_o^2 \left[ \frac{4(c_1 - c_2)}{3} + \frac{2(c_1^3 - c_2^3)}{9} - \frac{4}{3}(\tan^{-1}(c_1) - \tan^{-1}(c_2)) \right] \quad (D.10)$$

which is the same as Eqn. 4.2.

## E. Second Harmonic Experimental Procedure

The laser is operated in the same manner as for the ion experiments, but rather than measuring the ions which are created we are measuring the second harmonic photons which are created colinearly with the laser beam. The vacuum chamber configuration which is shown in Fig. 2.6 is also used for this experiment, but the measured signal is now transmitted through the output window of the chamber. Additionally, an RG1000 filter is placed before the input window on the chamber to prevent laser flashlamp light and room light from entering the chamber yet allow the laser to pass through with minimal attenuation. An output window made of BK7 is located along the laser axis to allow measurement of the second harmonic in the forward direction. Laser harmonics are separated with bandpass filters and detected with a photomultiplier tube. Initial experiments showed a significant amount of fluorescing in the filters due to absorption of the fundamental IR wavelength. This fluorescence was greatly reduced by placing a 45° dielectric-coated IR mirror before the filters. The second harmonic is able to pass through the mirror with a small amount of attenuation, but the fundamental wavelength is attenuated by a factor of ~1000 thereby reducing the intensity incident on the filters.

Experiments which measured the spectral content of the harmonic signal made use of a 1/4 meter scanning monochrometer. The bandpass filters and dielectric mirrors were still used to separate the harmonic signals. A photomultiplier tube was placed at the output of the monochrometer to measure the harmonic signal strength as the monochrometer was scanned across the wavelength region near 527 nm. The monochrometer was operated in second-order which provided a wavelength resolution of 0.5 Å for the second harmonic. Wavelength scans were performed at four different

pressures. The position of the central frequency (*i.e.* unshifted frequency) was calibrated by frequency doubling the laser in a KDP crystal and performing a wavelength scan with no gas present in the vacuum chamber and no RG1000 filter before the chamber.

Some background harmonic signal was still present using this setup, however the signal attributable to "other effects" such as harmonic generation in windows and filters was approximately a factor of 100 lower in intensity than the signal from the laser-gas interaction. The amount of background was measure by performing intensity scans both with and without gas in the chamber. The intensity dependent background signal was then subtracted from any additional data which was taken.

## REFERENCES

1. A. Einstein, *Annalen der Physik* **17**, 891 (1905).
2. M. Goeppert-Mayer, *Ann. Phys.* **9**, 273 (1931).
3. W. Kaiser and C. G. B. Garrett, "Two-Photon Excitation in  $\text{CaF}_2:\text{Eu}^{2+}$ ," *Phys. Rev. Lett.* **7**, 229 (1961).
4. I. D. Abella, "Optical Double-Photon Absorption in Cesium Vapor," *Phys. Rev. Lett.* **9**, 453 (1962).
5. R. G. Meyerand Jr. and A. F. Haught, "Gas Breakdown at Optical Frequencies," *Phys. Rev. Lett.* **11**, 401 (1963).
6. G. S. Voronov and N. B. Delone, *Sov. Phys. JETP Lett.*, **1**, 66 (1965).
7. G. S. Voronov and N. B. Delone, "Many-Photon Ionization of the Xenon Atom by Ruby Laser Radiation," *Sov. Phys. JETP* **23**, 54 (1966).
8. G. S. Voronov, G. A. Delone, and N. B. Delone, "Multiphoton Ionization of Atoms II. Ionization of Krypton by Ruby-Laser Radiation," *Sov. Phys. JETP* **24**, 1122 (1967).
9. P. Lambropoulos, "Topics on Multiphoton Processes in Atoms," from *Advances in Atomic and Molecular Physics, Vol 12* (Academic Press, New York 1976).
10. G. A. Kyrala and T. D. Nichols, "Measurement of the Absolute Rate for Multiphoton Ionization of Atomic Hydrogen at 248 nm," in *Multiphoton Processes* (proceedings of the fifth International Conference on Multiphoton Processes), ed. G. Mainfray and P. Agostini (Service de Physique Atomique CEN, Saclay, France, 1991).
11. H. B. Bebb and A. Gold, "Multiphoton Ionization of Hydrogen and Rare-Gas Atoms," *Phys. Rev.* **143**, 1 (1966).

12. M. V. Fedorov and A. E. Kazakov, "Resonances and Saturation in Multiphoton Bound-Free Transitions," *Prog. Quant. Electr.* **13**, 1 (1989).
13. F. H. M. Faisal, *Theory of Multiphoton Processes*, (Plenum Press, New York 1987).
14. A. L'Huillier, L. A. Lompré, G. Mainfray, and C. Manus, "Multiply Charged Ions Induced by Multiphoton Absorption Processes in Rare-Gas Atoms at 1.064  $\mu\text{m}$ ," *J. Phys. B* **16**, 1363 (1983).
15. A. L'Huillier, L. A. Lompré, G. Mainfray, and C. Manus, "Multiply Charged Ions Induced by Multiphoton Absorption in Rare Gases at 0.53  $\mu\text{m}$ ," *Phys. Rev. A* **27**, 2503 (1983).
16. S. Augst, D. D. Meyerhofer, D. Strickland, and S. L. Chin, "Laser Ionization of Noble Gases by Coulomb-Barrier Suppression," *J. Opt. Soc. Am. B.* **8**, 858 (1991).
17. S. Augst, D. Strickland, D. D. Meyerhofer, S. L. Chin and J. H. Eberly, "Tunneling Ionization of Noble Gases in a High-Intensity Laser Field," *Phys. Rev. Lett.* **63**, 2212 (1989).
18. K. Codling, L. J. Frasinski, and P. A. Hatherly, "On the Field Ionisation of Diatomic Molecules by Intense Laser Fields," *J. Phys. B.* **22**, L321 (1989).
19. L. V. Keldysh, "Ionization in the Field of a Strong Electromagnetic Wave," *Zh. Eksp. Teor. Fiz.* **47**, 1945 (1964) [*Sov. Phys. JETP* **20**, 1307 (1965)].
20. D. M. Volkov, "Über eine Klasse von Lösungen der Diracschen Gleichung," *Z. Phys.* **94**, 250 (1935).
21. F. H. M. Faisal, "Multiple Absorption of Laser Photons by Atoms," *J. Phys. B* **6**, L89 (1973).
22. H. R. Reiss, "Effect of an Intense Electromagnetic Field on a Weakly Bound System," *Phys. Rev. A* **22**, 1786 (1980).

23. A. Szöke, in *Atomic and Molecular Processes with Short Intense Laser Pulses*, ed. A. D. Bandrauk (Plenum Press, New York, 1987), p. 207.
24. M. D. Perry, A. Szöke, O. L. Landen, and E. M. Campbell, "Nonresonant Multiphoton Ionization of Noble Gases: Theory and Experiment," *Phys. Rev. Lett.* **60**, 1270 (1988).
25. T. W. B. Kibble, "Refraction of Electron Beams by Intense Electromagnetic Waves," *Phys. Rev. Lett.* **16**, 1054 (1966).
26. T. W. B. Kibble, "Mutual Refraction of Electrons and Photons," *Phys. Rev.* **150**, 1060 (1966).
27. P. H. Bucksbaum, M. Bashkansky, and T. J. McIlrath, "Scattering of Electrons by Intense Coherent Light," *Phys. Rev. Lett.* **58**, 349 (1987).
28. M. R. Cervenán and N. R. Isenor, "Multiphoton Ionization Yield Curves for Gaussian Laser Beams," *Opt. Comm.* **13**, 175 (1975).
29. G. Mainfray and C. Manus, "Resonance Effects in Multiphoton Ionization of Atoms," *App. Opt.* **19**, 3934 (1980).
30. L. A. Lompré, G. Mainfray, C. Manus, and J. P. Marinier, "Laser Light Statistics and Bandwidth Effects in Resonant Multiphoton Ionisation of Caesium Atoms at 1.059  $\mu\text{m}$ ," *J. Phys. B* **14**, 4307 (1981).
31. L. A. Lompré, A. L'Huillier, G. Mainfray, and C. Manus, "Multiphoton Ionisation of He Atoms at 532 nm," *Phys. Lett. A* **112A**, 319 (1985).
32. A. L'Huillier, L. A. Lompré, G. Mainfray, and C. Manus, "Laser Pulse Duration Effects in  $\text{Xe}^{2+}$  Ions Induced by Multiphoton Absorption at 0.53  $\mu\text{m}$ ," *J. Physique* **44**, 1247 (1983).
33. X. F. Li, A. L'Huillier, M. Ferray, L. A. Lompré, and G. Mainfray, "Multiple-Harmonic Generation in Rare Gases at High Laser Intensity," *Phys. Rev. A* **39** (11), 5751–5761 (1989).

34. A. L'Huillier, L. A. Lompré, M. Ferray, X. F. Li, G. Mainfray, and C. Manus, "Third-Harmonic Generation in Xenon in a Pulsed Jet and a Gas Cell," *Europhys. Lett.* **5**, 601 (1988).
35. L. A. Lompré, A. L'Huillier, and G. Mainfray, "Laser Pulse Duration Effects in the Production of Xe Ions," at *International Conference on Multiphoton Processes (ICOMP) V*, Paris, France Sept. 24-28, 1990, talk T15.
36. M. D. Perry, O. L. Landen, A. Szöke, and E. M. Campbell, "Multiphoton Ionization of the Noble Gases by an Intense  $10^{14}$  W/cm<sup>2</sup> Dye Laser," *Phys. Rev. A* **37**, 747 (1988).
37. O. L. Landen, M. D. Perry, and E. M. Campbell, "Resonant Multiphoton Ionization of Krypton by Intense uv Laser Radiation," *Phys. Rev. Lett.* **59**, 2558 (1987).
38. M. D. Perry, and O. L. Landen, "Resonantly Enhanced Multiphoton Ionization of Krypton and Xenon with Intense Ultraviolet Laser Radiation," *Phys. Rev. A* **38**, 2815 (1988).
39. M.D. Perry, A. Szöke, and K. C. Kulander, "Resonantly-Enhanced Above-Threshold Ionization of Helium," *Phys. Rev. Lett.* **63**, 1058 (1989).
40. J. H. Eberly, "Extended Two-Level Theory of the Exponential Index of Multiphoton Processes," *Phys. Rev. Lett.* **42**, 1049 (1979).
41. A. L'Huillier, X. Tang, and P. Lambropoulos, "Multiphoton Ionization of Rare Gases using Multichannel-Quantum-Defect Theory," *Phys. Rev. A* **39**, 1112 (1989).
42. X.-Tang, P. Lambropoulos, A. L'Huillier, and S. N. Dixit, "Theory of Resonant Multiphoton Ionization of Krypton by Intense Ultraviolet Laser Radiation," *Phys. Rev. A* **40**, 7026 (1989).
43. R. R. Freeman, P. H. Bucksbaum, H. Milchberg, S. Darack, D. Schumacher, and M. E. Geusic, "Above-Threshold Ionization with Subpicosecond Laser Pulses," *Phys. Rev. Lett.* **59**, 1092 (1987).

44. H. G. Muller, H. B. van Linden van den Heuvell, P. Agostini, G. Petite, A. Antonetti, M. Franco, and A. Migus, "Multiphoton Ionization of Xenon with 100-fs Laser Pulses," *Phys. Rev. Lett.* **60**, 565 (1988).
45. H. Rottke, B. Wolff, M. Brickwedde, D. Feldmann, and K. H. Welge, "Multiphoton Ionization of Atomic Hydrogen in Intense Subpicosecond Laser Pulses," *Phys. Rev. Lett.* **64**, 404 (1990).
46. R. R. Freeman and P. H. Bucksbaum, "Investigations of Above-Threshold Ionization using Subpicosecond Laser Pulses," *J. Phys. B* **24**, 325 (1991).
47. A. Szöke, O. L. Landen, and M. D. Perry, "Experimental Study of Atomic Structure in Strong Electromagnetic Fields," *Phys. Rev. A* **40**, 2766 (1989).
48. B. W. Boreham and J. L. Hughes, "Measurement of Ionization Threshold Intensities in Helium using Ponderomotive Force Accelerated Electrons," *Zh. Eksp. Teor. Fiz.* **80** (1981) [*Sov. Phys. JETP* **53**, 252 (1981)].
49. K. G. H. Baldwin and B. W. Boreham, "Investigation of Tunneling Processes in Laser-Induced Ionization of Argon," *J. Appl. Phys.* **52**, 2627 (1981).
50. F. Yergeau, S. L. Chin, and P. Lavigne, "Multiple Ionisation of Rare-Gas Atoms by an Intense CO<sub>2</sub> Laser ( $10^{14}$  W cm<sup>-2</sup>)," *J. Phys. B* **20**, 723 (1987).
51. S. L. Chin, W. Xiong, and P. Lavigne, "Creation of Multiple Charges (up to Xe<sup>6+</sup>) from Xe Atoms by an Intense CO<sub>2</sub> Laser," *J. Opt. Soc. Am B* **4**, 853 (1987).
52. W. Xiong, F. Yergeau, S. L. Chin, and P. Lavigne "Multiphoton Ionisation of Rare Gases by a CO<sub>2</sub> Laser: Electron Spectroscopy," *J. Phys. B* **21**, L159 (1988).
53. S. L. Chin and W. Xiong, *Fundamentals of Laser Interactions II*, edited by F. Ehlotzky (Springer-Verlag, Berlin, 1989), p. 80.
54. W. Xiong and S. L. Chin, "Tunnel Ionization of K and Xe atoms by Intense CO<sub>2</sub> Laser," *Sov. Phys. JETP* **99**, 481 (1991).

55. S. L. Chin, C. Rolland, P. B. Corkum, and P. Kelly, "Multiphoton Ionization of Xe and Kr with Intense 0.62- $\mu\text{m}$  Femtosecond Pulses," *Phys. Rev. Lett.* **61**, 153 (1988).
56. T. S. Luk, U. Johann, H. Egger, H. Pummer, and C. K. Rhodes, "Collision-free Multiple Photon Ionization of Atoms and Molecules at 193 nm," *Phys. Rev. A* **32**, 214 (1985).
57. C. K. Rhodes, "Physical Processes at High Field Strengths," *Phys. Scr.* **T17**, 193 (1987).
58. G. Gibson, T. S. Luk, and C. K. Rhodes, "Tunneling Ionization in the Multiphoton Regime," *Phys. Rev. A* **41**, 5049 (1990).
59. A. J. Taylor, C. R. Tallman, J. P. Roberts, C. S. Lester, T. R. Gosnell, P. H. Y. Lee, and G. A. Kyrala, "High-Intensity Subpicosecond XeCl Laser System," *Opt. Lett.* **15**, 39 (1990). The  $\text{Xe}^{13+}$  result is from private communication.
60. P. Maine, D. Strickland, P. Bado, M. Pessot, and G. Mourou, "Generation of Ultrahigh Peak Power Pulses by Chirped Pulse Amplification," *IEEE J. Quantum Electron.* **QE-24**, 398 (1988).
61. M. Pessot, P. Maine, and G. Mourou, "1000 Times Expansion/Compression of Optical Pulses for Chirped Pulse Amplification," *Opt. Comm.* **62**, 419 (1987).
62. D. Strickland, "Development of an Ultra-Bright Laser and an Application to Multi-Photon Ionization," Ph. D. thesis, University of Rochester, 1988 (unpublished).
63. Y. H. Chuang, D. D. Meyerhofer, S. Augst, H. Chen, J. Peatross, and S. Uchida, "Suppression of the Pedestal in a Chirped-Pulse-Amplification Laser," *J. Opt. Soc. Am. B.* **8**, 1226 (1991).
64. G. P. Agrawal, *Nonlinear Fiber Optics* (Academic Press, Boston, 1989), Chap. 4 and 6.

65. E. B. Treacy, "Optical Pulse Compression with Diffraction Gratings," *IEEE J. Quant. Electr.* **QE-5**, 454 (1969).
66. O. E. Martinez, "3000 Times Grating Compressor with Positive Group Velocity Dispersion: Application to Fiber Compensation in 1.3, 1.6  $\mu\text{m}$  Regime," *IEEE J. Quantum Electron.* **QE-23**, 59 (1987).
67. A. E. Siegman, *Lasers*, (University Science Books, Mill Valley, CA, 1986), Chapter 10, p. 382-386.
68. M. D. Perry, F. G. Patterson, and J. Weston, "Spectral Shaping in Chirped-Pulse Amplification," *Opt. Lett.* **15**, 381 (1990).
69. D. Normand, M. Ferray, L. A. Lompré, O. Gobert, A. L'Huillier, and G. Mainfray, "Focused Laser Intensity Measurement at  $10^{18}$  W/cm<sup>2</sup> and 1053 nm," *Opt. Lett.* **15**, 1400 (1990).
70. J. Janszky, G. Corradi, and R. N. Gyuzalian, "On a Possibility of Analysing the Temporal Characteristics of Short Light Pulses," *Opt. Commun.* **23**, 293 (1977).
71. G. Albrecht, A. Antonetti, and G. Mourou, "Temporal Shape Analysis of Nd<sup>3+</sup>:YAG Active Passive Mode-Locked Pulses," *Opt. Commun.* **40**, 59 (1981).
72. F. Salin, P. Georges, G. Roger, and A. Brun, "Single-Shot Measurement of a 52-fs Pulse," *Appl. Opt.* **26**, 4528 (1987).
73. P. B. Corkum, N. H. Burnett, and F. Brunel, "Above-Threshold Ionization in the Long-Wavelength Limit," *Phys. Rev. Lett.* **62**, 1259 (1989).
74. *Manual for Channelplate Charged Particle Detectors Model CP-601 and CP-602*, Comstock Inc., Oak Ridge, TN.
75. D. L. Book, *NRL Plasma Formulary* (Naval Research Laboratory, Washington D. C., 1987), pp. 53-54.

76. M. V. Ammosov, N. B. Delone, and V. P. Krainov, "Tunnel Ionization of Complex Atoms and of Atomic Ions in an Alternating Electromagnetic Field," *Zh. Eksp. Teor. Fiz.* **91**, 2008 (1986) [*Sov. Phys. JETP* **64**, 1191 (1986)].
77. L. D. Landau and E. M. Lifshitz, *Quantum Mechanics* (Pergamon, New York, 1965), worked out problem at end of §73.
78. A. M. Perelomov, V. S. Popov, and M. V. Terent'ev, "Ionization of Atoms in an Alternating Electric Field," *J. Exptl. Theoret. Phys.* **50**, 1393 (1966) [*Sov. Phys. JETP* **23**, 924 (1966)].
79. L. D. Landau and E. M. Lifshitz, *Quantum Mechanics* (Pergamon, New York, 1965), §46.
80. R. L. Kelly and L. J. Palumbo, *Atomic and Ionic Emission Lines Below 2000 Angstroms: Hydrogen Through Krypton*, (Naval Research Laboratory, Washington D. C. 1973).
81. P. M. Koch, B. E. Sauer, M. R. W. Bellermand, and L. Moorman, "Microwave Ionization of Excited Hydrogen Atoms: Experiments with Widely Varying Parameters," Big Sky Workshop on Super-Intense Laser-Atom Physics, talk T15, Big Sky, MT June 22-25, 1991.
82. See for example, B. H. Bransden and C. J. Joachain, *Physics of Atoms and Molecules*, (Longman, London and New York, 1983), Appendix 5.
83. H. R. Reiss and R. S. Bardfield, "Quantitative Theoretical Predictions for Ionization Experiments in Very Strong Fields," Big Sky Workshop on Super-Intense Laser-Atom Physics, poster P2, Big Sky, MT June 22-25, 1991.
84. M. Brewczyk and M. Gajda, "Mechanism of the Multiple Ionisation of Atoms by Strong Laser Pulses," *J. Phys. B* **21**, L383 (1988).
85. M. Brewczyk and M. Gajda, "Thomas-Fermi Atom in a Static Homogeneous Electric Field," *Phys. Rev. A* **40**, 3475 (1989).

86. M. Brewczyk and K. Rzazewski, "How good is Adiabatic Approximation for Strong Field Multiple Ionization?," at *International Conference on Multiphoton Processes (ICOMP) V*, Paris, France Sept. 24-28, 1990, talk T12.
87. S. M. Susskind, E. J. Valeo, C. R. Oberman, and I. B. Bernstein, "Charge States of Many-Electron Atoms in a Strong Laser Field," *Phys. Rev. A* **43**, 2569 (1991).
88. D. T. Alimov and N. B. Delone, "Ionization of Atoms in an Intense Light Field," *Sov. Phys. JETP* **43**, 15 (1976).
89. M. V. Fedorov and A. M. Movsesian, "Interference Suppression of Photoionization of Rydberg Atoms in a Strong Electromagnetic Field," *J. Opt. Soc. Am. B.* **6**, 928 (1989).
90. M. S. Malcuit, R. W. Boyd, W. V. Davis, and K. Rzazewski, "Anomalies in Optical Harmonic Generation using High-Intensity Laser Radiation," *Phys. Rev. A.* **41**, 3822 (1990).
91. D. S. Bethune, "Optical Second-Harmonic Generation in Atomic Vapors with Focused Beams," *Phys. Rev. A* **23** (6), 3139–3151 (1981).
92. S. Augst, D. D. Meyerhofer, C. I. Moore, and J. Peatross, "Tunneling Ionization and Harmonic Generation in Krypton Gas using a High-Intensity, 1- $\mu\text{m}$ , 1-ps Laser", in the Proceedings of SPIE OE/LASE '90, *Femtosecond to Nanosecond High-Intensity Lasers and Applications*, **1229**, 152 (pub. by SPIE, Bellingham, WA, 1990). The intensities in Fig. 1 and Fig. 3 are too high by approximately a factor of 4.
93. J. F. Ward and G. H. C. New, "Optical Third Harmonic Generation in Gases by a Focused Laser Beam," *Phys. Rev.* **185**, 57–72 (1969).
94. A. E. Siegman, *Lasers*, (University Science Books, Mill Valley, CA, 1986), Chapter 17.